João Pedro Bento Vilas

Master of Science

Interferometric mapping of test mass surfaces for precise position determination in inertial sensors

Dissertation submitted in partial fulfillment
of the requirements for the degree of

Master of Science in
Physics Engineering

Adviser: Dr. Alexander Sell, Lead of LET,
Airbus Defence and Space

Technical Supervisor: Dr. Harald Kögel, Associate,
Airbus Defence and Space

Examination Committee

Chairperson: Prof. Dr. Isabel Catarino
Raporteur: Dr. Jorge Machado
Members: Dr. Alexander Sell
Dr. Harald Kögel

FACULDADE DE
CIÊNCIAS E TECNOLOGIA
UNIVERSIDADE NOVA DE LISBOA

April, 2018

Interferometric mapping of test mass surfaces for precise position determination in inertial sensors

This document was created using the (pdf)LaTeX processor, based in the "novathesis" template[1], developed at the Dep. Informática of FCT-NOVA [2].
[1] https://github.com/joaomlourenco/novathesis [2] http://www.di.fct.unl.pt

Acknowledgements

I would like to thank my advisor Dr. Alexander Sell and technical supervisor Dr. Harald Kögel for not only giving me the opportunity to work in this project, but also all the support given to me throughout all this work with their knowledge, laboratory expertise and advise.

For my colleagues in the LET, I want to give a special thanks to PhD students Markus Oswald and Oliver Mandel who were always available to help me and explain basic concepts of electronics and signal process.

To my colleagues in the student office, I want to thank them all for the nice conversations and good times we had together, making my time in Friedrichshafen really enjoyable.

I want to thank my brothers, my girlfriend and most of all my mother for all the support and motivation given during my studies.

Abstract

Novel inertial reference sensors for space applications using optical readout of a Spherical proof mass (SPM), which enable full drag-free operations, are being studied for future space programs such as Laser Interferometer Space Antenna (LISA) and Big Bang Observer. Using this concept results in the reduction of residual acceleration noise by the proof mass, but with the SPM under rotation the surface topography induces errors in the center of mass position determination due to factors like surface finish, that changes the optical path length on a nanometer scale, and the reflection angle.

To determine successfully the center of mass position with picometer accuracy, a surface map of the proof mass is necessary in order to correct the measurement data, thus improving the precision of the position determination.

An experimental setup using double heterodyne interferometer in opposing configuration developed by Airbus, Friedrichshafen, is used to map one single surface circumference of a continuously rotating proof mass. In this thesis, enhancements were done to allow a complete surface map of the SPM with picometer accuracy at relevant angular frequencies. Enhancements made were: The inertial-mass degrees of freedom were increased by adding a second rotational stage. Overall software performance has been improved by implementing fast angle read-out by the encoders. Code in LabVIEW and MATLAB has been developed, capable of making a full 2D surface map of the SPM for calibration of errors in the determination of the position of the center of mass. Data acquisition has been sped up to enable low-noise full 2D surface maps.

Keywords: Interferometry, heterodyne interferometry, surface measurements, center of mass determination.

Resumo

Novos sensores de referência inercial para aplicações espaciais com recurso a leitura ótica de uma massa inercial esférica (SPM), que permite operações sem arrasto, são estudados para futuros programas espaciais como o Laser Interferometer Space Antenna (LISA) e o Big Bang Observer. A utilização deste conceito resulta na redução do ruído de aceleração residual pela massa inercial, mas com a SPM sob rotação a topografia da superfície induz erros na determinação do centro de massa devido a fatores como acabamento superficial que altera o comprimento do caminho ótico em escala nanométrica e ângulo de reflexão.

Para determinar com sucesso a posição do centro de massa com precisão picométrica, um mapa de superfície da massa inercial é usado para corrigir medições feitas, melhorando assim a precisão da determinação da posição.

Uma montagem experimental usando dois interferómetros heteródinos em configuração oposta, desenvolvida pela Airbus Friedrichshafen, é usada para mapear uma única circunferência da superfície da massa inercial em rotação contínua. Nesta tese foram realizados aprimoramentos para permitir um mapa de superfície completo da SPM com exatidão picométrica em frequências angulares relevantes. Os aprimoramentos feitos foram: Aumento dos graus de liberdade da massa inercial com a adição de um segundo estágio rotacional. O desempenho geral do software foi melhorado com a implementação da leitura rápida dos ângulos dos encoders. Código desenvolvido em LabVIEW e MATLAB capaz de fazer um mapa de superfície 2D completo da SPM para calibração de erros na determinação da posição do centro de massa. A aquisição de dados foi acelerada para permitir fazer mapas de superfície bidimensionais de baixo ruído.

Palavras-chave: Interferometria, interferometria heteródina, medição de superficies, determinação de centro de massa.

Contents

List of Figures

List of Tables

Acronyms

AOM Acousto-optic modulator.

DRS Disturbance Reduction System.

FIFO First in first out.

FPGA Field programmable gate array.

GRS Gravitational Reference Sensor.

LIGO Laser Interferometer Gravitational-Wave Observatory.

LISA Laser Interferometer Space Antenna.

PCB Printable circuit board.

PLL Phase locked loop.

PSD Power spectrum density.

QPD Quadrant photodetector.

SPM Spherical proof mass.

VHDL Very High Speed Integrated Circuit Hardware Description Language.

Chapter 1

Introduction

This chapter will start by introducing: the relationship between men and space, the first equipments designed to study space, what are gravitational waves and the differences between these and electromagnetic waves, the first indirect and direct detection of gravitational waves, what is Laser Interferometer Space Antenna, or LISA, and how a Gravitational Reference Sensor works. After introducing the mentioned topics, the motivation for the work presented here will be explained.

1.1 Astronomy

Ever since the first time Galileo used a telescope to observe motion of celestial bodies, mankind has used more and more advanced telescopes to observe the cosmos. In 1669, Newton introduced the first reflecting telescope, using mirrors. This type of telescope was in the forefront of technology until the 19th century when it started suffering from poor reflectivity and thermal properties of the mirrors.

At the turn of the 18th century, William Herschel and William Parsons were able to build reflectors with diameters ranging from 1.25 to 1.80 meters, which allowed for observation and discovery of more planets and moons inside the solar system.

Issues regarding reflectivity and thermal properties were solved in the mid 19th century as mirrors coating got better, allowing for the creation of the modern giant telescopes. These telescopes allowed us to see even beyond what was ever possible as new galaxies were observed, proving that the Milky Way is just one of millions.

All these discoveries were made by direct observation of visible light, which begs the question what could also be discovered if other wavelengths of the electromagnetic spectrum were also observed.

Since the 20th century, scientist have widen the boundaries of the known Universe

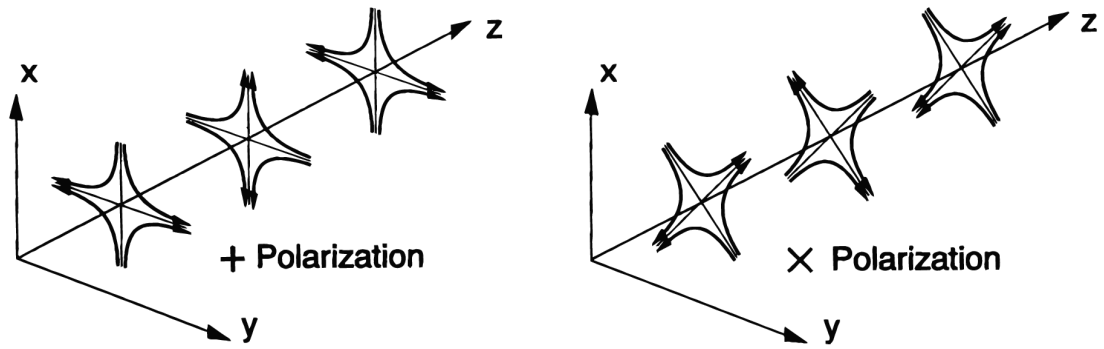

Figure 1.1: The gravitational waves produce tidal forces in planes transverse to the propagation direction, with different possible polarization states. The wave on the left is in the + polarization state, and the one on the right is in the × polarization state.[1]

further with the use of telescopes that are able to observe across the electromagnetic spectrum which led to the discovery of quasars, pulsars, the cosmic microwave background for low frequencies and X-ray stars, gamma-ray bursts, black holes for high frequencies. Such discoveries allowed us to know that the universe emerged from the big bang and has been expanding and where the first black holes were formed.

1.2 Gravitational waves

Electromagnetic waves are mainly generated by accelerated charges, due to charge conservation, or from interactions of atoms or other particles within celestial bodies, which propagate through spacetime. As the wavelength is much smaller than the celestial objects under observation, in principle they can be imaged. However, charged particles or dense dust or gas clouds can obscure objects from electromagnetic observation.

On the other hand, gravitational waves are distortions in spacetime with two types of polarization, figure 1.1, created by powerful merging or collisions of black holes or other massive celestial bodies, due to mass and momentum conservation. These waves are generated by the bulk mass distribution of the entire celestial body, resulting in a coherent emission with a wavelength comparable to or larger than the size of the object. Therefore proximity of the object to the detector is no issue, making gravitational waves a very reliable probe of the cosmos as to discover parts of the universe that were before invisible to us like black holes and other, maybe soon to be discovered, objects. Also unlike electromagnetic waves, gravitational waves might not be imaged but heard. Audio-like methods are needed to analyze these waves.

The existence of gravitational waves was theorized by Albert Einstein back in 1916, more than a hundred years ago, when he found that the wave solutions of linearized weak-field equations were transverse waves of spatial strain that travel at the speed of light, generated by time variations of the mass quadrupole moment of the source[2]. With this

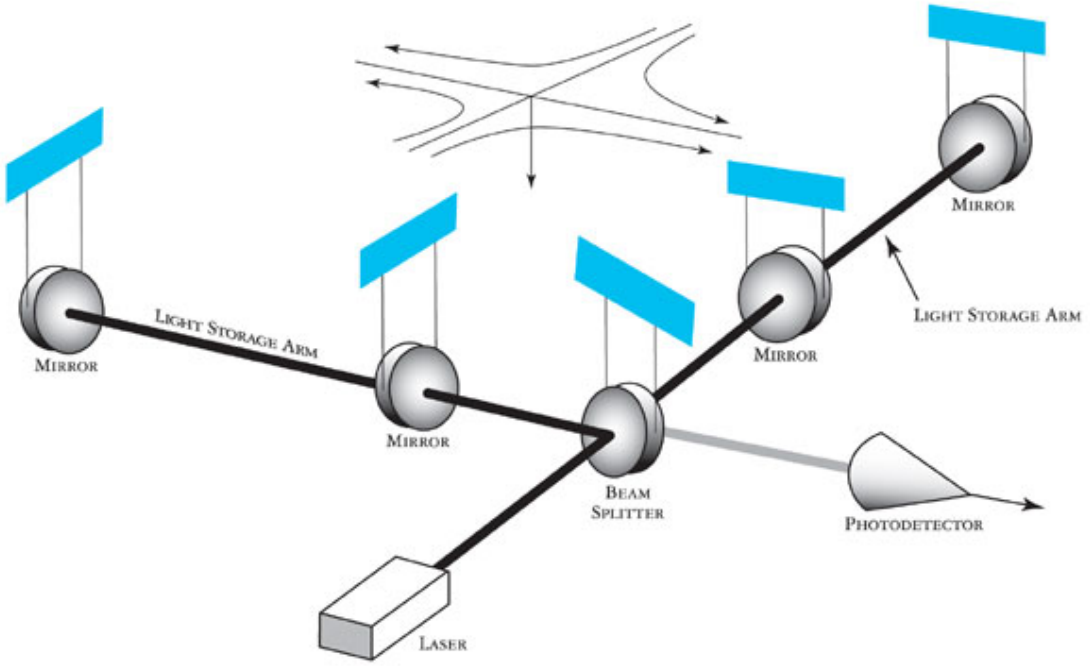

Figure 1.2: Basic design of the LIGO interferometers. Image: Caltech/MIT/LIGO Lab.

discovery, later scientist published different solutions for the field equations, solutions which describe black holes, rotating black holes and binary black hole mergers.

For years scientist tried to detect gravitational waves without success. Until 1974 when Joseph Taylor and Russell Hulse discovered a binary pulsar [3] which, according to general relativity, the stars fall closer together and orbit more quickly losing energy in form of gravitational waves. Observations confirmed this prediction therefore proving the existence of gravitational waves, making this the first indirect detection.

Having proven the existence of gravitational waves, detectors more sensitive over a wide range of frequency started being used, detectors such as Michelson interferometers.

1.2.1 The first direct detection of Gravitational Waves

In 2002, Laser Interferometer Gravitational-Wave Observatory (LIGO) made two stations composed each of two equally long tunnels perpendicular to each other with a laser beam being split and directed down the tunnels, with two test masses mirrors separated by 4 km, in Hanford, Washington, and Livingston, Louisiana, working as Michelson interferometers, figure 1.2.

These facilities measure gravitational wave strain, as a difference in length of its orthogonal arms, caused by a passing gravitational wave as can be seen in equation (1.2)[2], where h is the gravitational wave strain amplitude projected onto the detector.

$$L_X = L_Y = L = 4km \tag{1.1}$$

$$\Delta L(t) = \delta L_X - \delta L_Y = h(t)L \tag{1.2}$$

On September 14, 2015 at 09:50:45 UTC in Hanford and Livingston, a groundbreaking discovery was made when both detectors observed gravitational waves corresponding to a binary black hole system merging to form a single black hole. This discovery not also marks the beginning of a new chapter in mankind's space exploration but also brings closer theoretical physics to the realm of observable science.

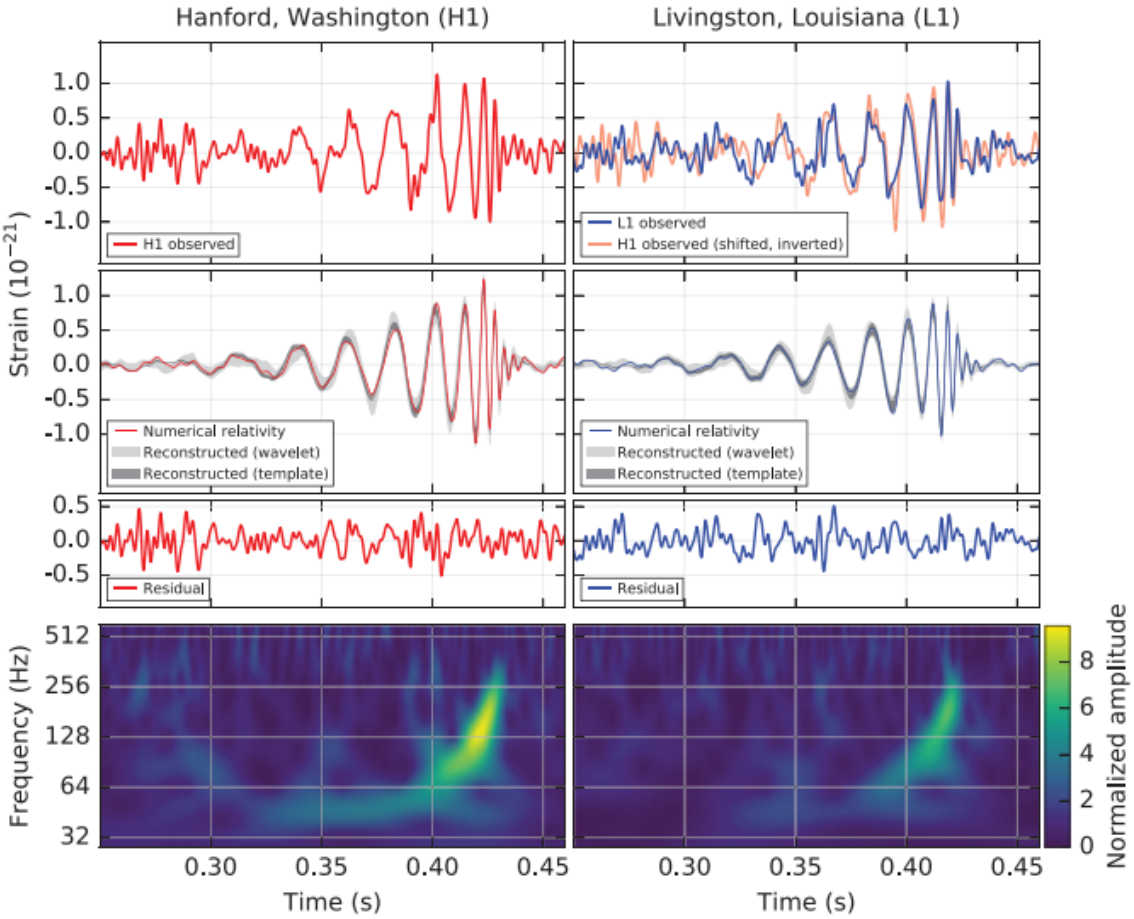

Figure 1.3: The gravitational wave observed by the LIGO Hanford (H1, left column panels) and Livingston (L1, right column panels) detectors. Time is shown relative to September 14, 2015 at 09:50:45 UTC. Figure taken from Abbot et al., PRL 116, 061102 (2016)[2]

The detected gravitational waves can be seen in figure 1.3. The first row plots the gravitational wave strain, the second row shows the gravitational wave strain projected onto each detector with three calculations using different types of wavelets [4], the residuals are plotted in the third row after subtracting the filtered numerical relativity waveform from the filtered detector time series and the bottom row is a time-frequency representation of the strain data, showing the signal frequency increasing over time. In figure 1.4

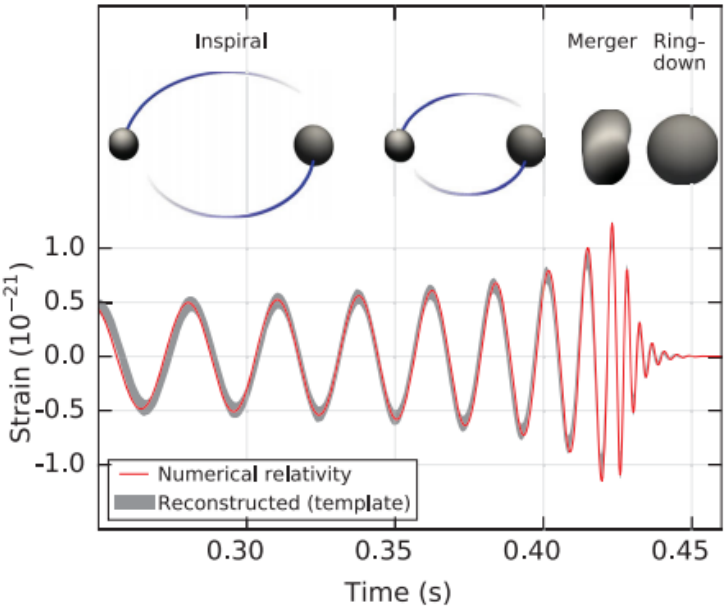

Figure 1.4: Visual representation of the acquired data. Figure taken from Abbot et al., PRL 116, 061102 (2016)[2]

the inset images show the visual meaning of the numerical relativity models of the black hole horizons as the black holes coalesce.

Although this first direct detection of gravitational waves was a scientific breakthrough, the limitations of a ground detector are already put into question. A ground detector, like the LIGO in Louisiana and Hanford, gives access to the high-frequency regime of gravitational wave astronomy, frequencies above ten hertz. The high-frequency regime is where it's expected to observe low mass sources at low redshift. The low-frequency regime, below one hertz, will probably never be accessible from the ground due to the limited detector size and seismic disturbances. The heaviest and most diverse objects are expected to be observed in the low-frequency regime[5]. In answer to this problem, LISA or Laser Interferometer Space Antenna is being created.

1.3 Laser Interferometer Space Antenna, LISA

LISA is a space mission designed to measure gravitational waves over a broad band at low frequencies from 0.1 mHz to 1 Hz. In this range the strongest sources of gravitational waves will be detected and with this new information it will be possible to: determine how massive black holes present in most galactic nuclei have formed and grown over time, to trace the interaction of galaxy growth and massive black hole growth over the entire history of galaxy formation, explore the populations of stellar-mass compact objects in galactic nuclei and their dynamics, study the signals from stellar-mass close binaries in the galaxy and give information on the extreme endpoints of stellar evolution and galactic structure using galactic binaries and observe highly relativistic mergers of black

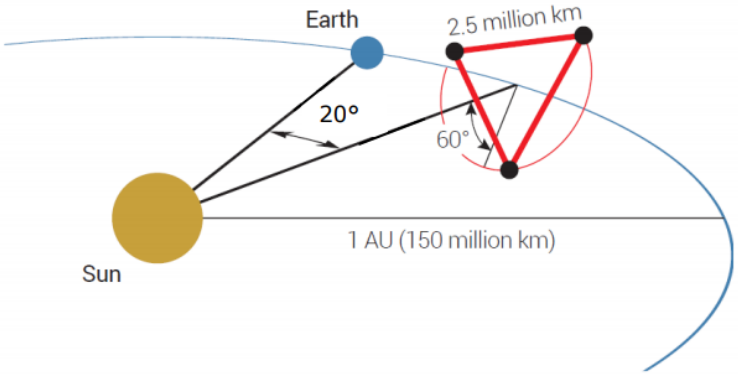

Figure 1.5: LISA orbit [5]

hole binaries and provide strong tests of the predictions and validity of the general theory of relativity.

LISA is composed of three drag free spacecrafts that form an equilateral triangle in space, trailing the earth in a helio-centric orbit between 50 and 65 million km from earth, where each side has an arm length of $2.5 \cdot 10^6$ km, figure 1.5. Each arm connects the spacecrafts via interferometric laser links between free falling test masses co-orbiting inside each spacecraft. Gravitational waves will be detected due to the interferometric measurement of differential optical pathlength modulation along the three sides of a triangular configuration, with picometer resolution and reaching a strain sensivity of 10^{-21}. The Michelson interferometers used in LISA are implemented differently from a conventional Michelson interferometer like the one in LIGO, they closer resemble a Doppler tracking.

In order to realize such measurements, the optical pathlength is continuously measured by heterodyne laser interferometers in both directions along each arm. Due to the distance between spacecrafts, direct reflection of the laser beam is not possible, so using stable lasers at 1064 nm and 2 watts of power transmitted at each end, the received laser beam power is in the order of 100 pW, therefore each spacecraft acts as an active transponder, transmitting a high-power beam that is phase-locked to the receiving laser beam, with a fixed offset frequency.

The measurement between free-falling test masses is separated in three parts:

- Local test mass to optical bench 1;
- Optical bench 1 to external optical bench 2;
- Optical bench 2 to local test mass.

In figure 1.6 a single arm measurement is explained and broken up into the three different measurements, two between the respective test mass and the spacecraft and one between the two spacecrafts. These measurements are recombined allowing reconstruction of the distance between test masses and the measurement between the free falling

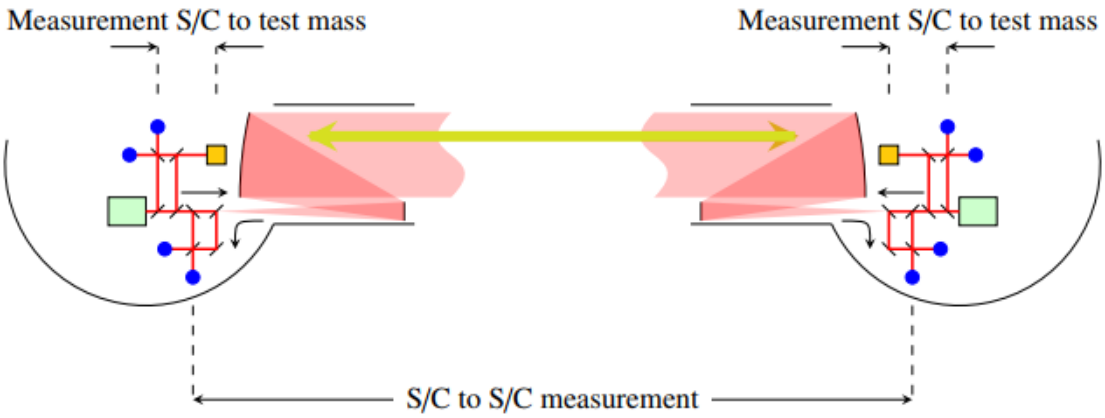

Figure 1.6: LISA measuring partition [6]

test mass and its local optical bench also provides the Gravitational Reference Sensor (GRS). The red lines represent the laser path inside the spacecraft, the yellow squares are the test masses, in green are the laser sources and the blue dots indicate where the interferometric measurements are taken.

The three interferometric arms of LISA measure independently from each other. Two of the three arms work as Michelson interferometers measuring the two possible polarizations of the gravitational waves while the third one is insensitive to the passing gravitational waves, being used to characterize the instrumental noise background.

Each spacecraft contains two test masses, each one for a different arm, which must be shielded from noisy non-gravitational forces, acting on the spacecraft, and are used as geodesic reference test particles. In order to prevent relative accelerations between the test mass and the spacecraft in which it is contained, the latter is "drag-free controlled"with micro-Newton thrusters to follow the movement of the test mass along its interferometric arm, without any forces applied to the test mass along the measurement axes [5].

1.3.1 Gravitational Reference Sensor

The GRS is one of three components that make the Disturbance Reduction System (DRS). The DRS is composed of the GRS, feedback control system which navigates the spacecraft around the test mass and the micro-thrusters that control the spacecraft position. GRS provides shielding to the test mass from all external disturbances except from gravity, providing an inertial reference in spacetime to enable time varying position and distance measurement. In combination with the other components of DRS any movements between the test mass and the spacecraft, which houses it, represents an input for the feedback control system, hence making the spacecraft position itself accordingly with the test mass, providing a drag free system since the test mass movements are movements of the spacecraft as well.

GRS can be implemented in two different modes, drag-free and accelerometer. In the drag-free mode, the test mass moves freely in space and its position works as an input for the housing sensors and as an output to the spacecraft thrusters in order to keep the position and attitude of the test mass stable. In the accelerometer mode, the test mass position is kept fixed inside the spacecraft and the force applied to keep the test mass fixed is the input for the spacecraft thrusters.

Besides the two different modes which the GRS can function as, four possible GRS configurations for the LISA mission were designed to reduce complexity and to enhance the measurement precision [7]:

Configuration 1 - This is the current baseline design for LISA: two cubical test masses per spacecraft. These test masses are in a non drag-free environment under electrostatic suspension to keep them aligned with the respective interferometric arms. A combination of capacitive sensing and optical sensing is used to measure relative position of the test masses with respect to the spacecraft for drag-free control. The recently finished and highly successful LISA pathfinder mission, has shown this type of sensor can fulfill the high level requirements in differential acceleration noise of $3 \cdot 10^{-14} m \cdot s^{-2}/\sqrt{Hz}$ at $\approx 10^{-3} Hz$;

Configuration 2 - Uses one cubical test mass per spacecraft, acting as the only GRS of the respective spacecraft, resorting to In-Field pointing system;

Configuration 3 - A spinning spherical proof mass position optically sensed is used to drag-free control the spacecraft position, resorting to In-Field pointing system;

Configuration 4 - Unlike configuration 3, the spherical proof mass (SPM) would be completely drag-free inside the sensor.

Both configurations 3 and 4, unlike the previous, don't use electrostatic suspension and require superior technology to integrate a spherical proof mass. It is estimated that these configurations have lower noise than configurations 1 and 2.

Space missions like Gravity Probe B (GP-B), successfully tested spherical gyroscopes in Earth orbit with unprecedented accuracy [8].

1.3.2 Telescope pointing and In-Field pointing systems

During the LISA mission period, there will be fluctuations in the orbital dynamics of the constellation, affecting the apex angles of the triangle. These fluctuations are estimated to be $\pm 1^\circ$ on an annual timescale and need to be corrected. For this purpose two possible pointing concepts can be used, the Telescope pointing and In-Field pointing systems.

The baseline design for LISA is Telescope pointing, which articulates the position with ultralow noise tracking mechanism of two independent payload assemblies, of each spacecraft, composed of telescope, optical bench and proof mass.

The alternative concept developed by Astrium is the In-Field pointing. In this alternative instead of a movable optical assembly, there is a rigid payload with ultralow noise steering mirror at the telescope intermediate pupil. This steering mirror is positioned by a piezoelectric mechanism[9].

The In-Field pointing has several advantages over the Telescope pointing such as:

- The Single Active GRS concept can be used. In this concept both inertial sensors on the spacecraft can work as the reference for both telescopes in the spacecraft, increasing the mission robustness. This allows for redundancy between two alternative GRS system concepts, thus if for some reason one of the GRS isn't working at the meant specifications, the other GRS can be used.

- In the Single Active GRS concept, the active GRS can be in drag-free for all translational degrees of freedom, except for its rotatory degrees of freedom which require electrostatic suspension.

- The two optical benches of the spacecraft can be combined into one single optical bench which includes all necessary optical components.

- The total payload mass, volume and power consumption is lower.

1.4 Center of mass determination errors

Due to material density inhomogeneities, the geometric center of a spherical proof mass doesn't coincide with its center of mass. Considering the SPM geometric center, instead of the center of mass, inertial movements of the proof mass will result in false displacements signal output. Therefore the center of mass has to be determined in order to achieve the required accuracy parameters for LISA.

Advanced manufacturing processes studied in [10] can produce proof masses of Au-Pt and Cu-Be alloys with a center of mass uncertainty of ≈ 100 nm, which is not enough for LISA requirements.

For configurations 3 and 4 of LISAs GRS, there exist different methods to determine the center of mass. In configuration 3 the spinning SPM allows to shift signals caused by the out-of-roundness and mass center offset errors that would result from imperfections in the manufacturing process of the sphere, to frequencies outside of the measurement bandwidth. For configuration 4, to correct out-of-roundness and center of mass errors to allow the spacecraft to follow the sphere in a drag-free mode, the sphere center of mass position would be reconstructed on-ground during data analysis based on high precision topographic surface mapping with picometer accuracy.

1.5 Motivation

The detection of gravitational waves has proven to be one of the greatest challenges of the present scientific community. Detecting such waves would allow the observation of cosmic bodies and events never registered before. This challenge was since overcome, for high frequency regime, by LIGO on September 14, 2015 which detected a black hole merger event. But since this date several other discoveries were made.

One of the most important other observations done by LIGO was the collision of neutron stars on August 17, 2017. These cosmological bodies are the densest visible objects through electromagnetic waves and this is why this observation was so important, not only did LIGO detect the gravitational waves being emitted from the rotation of the two colliding neutron stars, but also other earth telescopes detected the gamma radiation emission of this event[11].

In order to measure the gravitational waves with the desired strain sensitivity of 10^{-21} in the low frequency regime, LISA requires an ultra accurate noise compensation system to isolate the free falling test masses from external disturbances, called the DRS.

The DRS is comprised of three different components, one being the GRS. Several distinct designs for the GRS were made, one of them allowing the use of a spherical proof mass in a total drag free environment with whole optical read out. Such a setup is only possible if the surface of the SPM is mapped at picometer accuracy level, since the SPM under rotation the surface topography induces errors in the determination of the position of the center of mass due to factors like surface finish that changes the optical path length on a nanometer scale and reflection angle.

An experimental setup capable of measuring single 2D circumference of the SPM, was already developed by Airbus Friedrichshafen with the possibility of being enhanced in order to map the total surface of the SPM.

By mapping the surface of the SPM it is possible to correctly determine the position of the center of mass and thus improving the GRS positioning accuracy and reaching the desired strain sensitivity for the LISA mission.

1.6 Objectives

With this thesis enhancements to the experimental setup capable of measuring single 2D circumferences of the SPM, are studied and implemented in order to successfully map the surface of the SPM.

The changes made are:

- Add one more degree of freedom to the SPM with a second rotational stage
- Implement fast angle read-out by the encoders, for precise determination of the spherical coordinates of the measurement spots

- Develop code in LabVIEW and MATLAB capable of making 2D surface map of the SPM in order to correct the errors in the determination of the center of mass position
- Speed up data acquisition in order to enable low-noise full 2D surface maps, by reducing the total measurement time and thus also reducing the impact of thermal drifts on the measurement accuracy.

Chapter 2

Theoretical Background

For the mentioned objectives in this thesis to be achieved, certain theoretical concepts must be explained. The concepts here explained are not meant to provide a deep knowledge of either optics or electronics but to give the necessary information to understand the work done.

This chapter will aboard the basic concepts of interferometry and how certain electronic components work.

2.1 Interferometry Principles

Interferometry is a measurement method using the phenomenon of interference of waves or principle of superposition. When two beams of the same frequency superpose, an intensity interference pattern is formed. The interference pattern changes according to the difference in phase of the beams, if the beams are in phase the resulting interference pattern will be constructive, if the beams are in anti-phase then the interference pattern will be destructive, any other combination of phases will result in an intermediate interference pattern that can be used to detect the phase difference of the beams[12]. Assuming two electrical fields expressed by:

$$\begin{cases} \overrightarrow{E}_1 = \overrightarrow{E}_{01}\, e^{i\left(\overrightarrow{k}\cdot\overrightarrow{r_1}-\omega t+\theta_1\right)} \\ \\ \overrightarrow{E}_2 = \overrightarrow{E}_{02}\, e^{i\left(\overrightarrow{k}\cdot\overrightarrow{r_2}-\omega t+\theta_2\right)}, \end{cases} \tag{2.1}$$

with $\overrightarrow{E}_{0x}$ as the amplitude of the wave, θ_x the initial phase of the wave, $\overrightarrow{k}$ as the propagation vector, $\overrightarrow{r}_x$ as the position vector and considering the wave frequency ω the same for both waves, the interference of the electrical fields is:

$$\overrightarrow{E} = \overrightarrow{E}_1 + \overrightarrow{E}_2 = \left[\overrightarrow{E}_{01} e^{i\left(\overrightarrow{k}\cdot\overrightarrow{r_1}+\theta_1\right)} + \overrightarrow{E}_{02} e^{i\left(\overrightarrow{k}\cdot\overrightarrow{r_2}+\theta_2\right)} \right] e^{-i\omega t} \tag{2.2}$$

Due to the properties of optical photodetectors, these cannot measure electrical field directly but time-average intensity of the light,

$$\begin{aligned} I_{total} &= \left\langle \left| \overrightarrow{E} \right|^2 \right\rangle = \left\langle \overrightarrow{E} \cdot \overrightarrow{E}^* \right\rangle = \left\langle \left(\overrightarrow{E}_1 + \overrightarrow{E}_2 \right) \cdot \left(\overrightarrow{E^*}_1 + \overrightarrow{E^*}_2 \right) \right\rangle \\ &= \left\langle \left| \overrightarrow{E_1} \right|^2 \right\rangle + \left\langle \left| \overrightarrow{E_2} \right|^2 \right\rangle + \left\langle \overrightarrow{E}_1 \cdot \overrightarrow{E^*}_2 \right\rangle + \left\langle \overrightarrow{E}_2 \cdot \overrightarrow{E^*}_1 \right\rangle \end{aligned} \tag{2.3}$$

with

$$\begin{cases} \left\langle \left| \overrightarrow{E_1} \right|^2 \right\rangle = I_1 \\ \\ \left\langle \left| \overrightarrow{E_2} \right|^2 \right\rangle = I_2 \\ \\ \left\langle \overrightarrow{E}_1 \cdot \overrightarrow{E^*}_2 \right\rangle = \left\langle \overrightarrow{E}_{01} \cdot \overrightarrow{E^*}_{02} \right\rangle e^{i\left[\overrightarrow{k}\left(\overrightarrow{r}_1 - \overrightarrow{r}_2\right) + (\theta_1 - \theta_2)\right]} \\ \qquad\qquad = \sqrt{I_1 I_2}\, e^{i\left[\overrightarrow{k}\left(\overrightarrow{r}_1 - \overrightarrow{r}_2\right) + (\theta_1 - \theta_2)\right]} \\ \\ \left\langle \overrightarrow{E}_2 \cdot \overrightarrow{E^*}_1 \right\rangle = \left\langle \overrightarrow{E}_{02} \cdot \overrightarrow{E^*}_{01} \right\rangle e^{-i\left[\overrightarrow{k}\left(\overrightarrow{r}_1 - \overrightarrow{r}_2\right) - (\theta_1 - \theta_2)\right]} \\ \qquad\qquad = \sqrt{I_1 I_2}\, e^{-i\left[\overrightarrow{k}\left(\overrightarrow{r}_1 - \overrightarrow{r}_2\right) - (\theta_1 - \theta_2)\right]} \end{cases} \tag{2.4}$$

Using the complex trigonometric function $\cos(\delta) = \frac{1}{2}\left(e^{i\delta} + e^{-i\delta}\right)$ and $\delta = \overrightarrow{k}\left(\overrightarrow{r}_1 - \overrightarrow{r}_2\right) - (\theta_1 - \theta_2)$, the time-average intensity simplifies

$$I_{total} = I_1 + I_2 + 2\sqrt{I_1 I_2}\cos(\delta) \tag{2.5}$$

Assuming both waves have the same initial phase and intensity,

$$I_{total} = 2I + 2I\cos(\delta) = 4I\cos^2\left(\frac{\delta}{2}\right) = 4I\cos^2\left(\frac{\overrightarrow{k}\left(\overrightarrow{r}_1 - \overrightarrow{r}_2\right)}{2}\right) \tag{2.6}$$

The last equation, 2.6, shows the relation between detected intensity by the photodetector and difference in wave positions $\overrightarrow{r}_1 - \overrightarrow{r}_2$. This relation is the reason why interferometry can be used for surface topography.

2.1.1 Michelson Interferometer

In the field of interferometry, several techniques exist to measure displacements like the Michelson interferometer. This interferometer uses a beam splitter which splits a light source along two arms perpendicular to each other. At the end of each path there is a

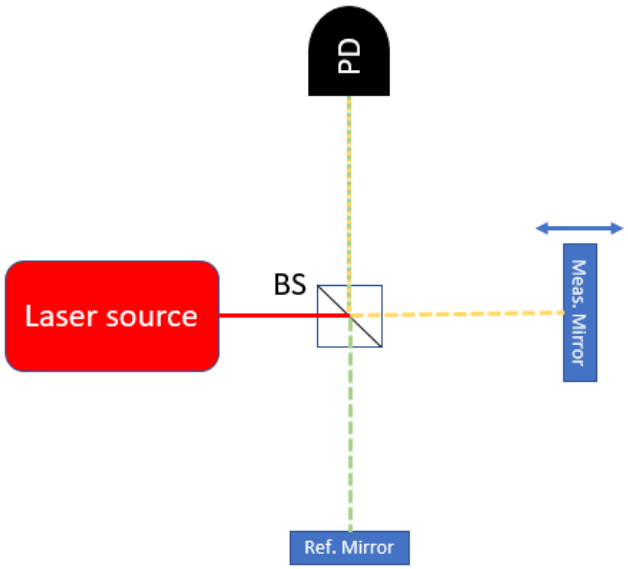

Figure 2.1: Michelson interferometer example. PD stands for photodetector and BS for beam splitter.

mirror which reflects back the light beam towards the beam splitter, where the beams recombine by the superposition principle. One of the mentioned mirrors works as a reference mirror and the other as the measurement mirror, the latter can be adjusted to increase or decrease the beam pathlength. The resulting interference pattern detected in a photodetector is directly correlated to the difference in the path length of the beams. A simple schematic of a Michelson interferometer is shown in figure 2.1 with the reference and measurement mirrors, a photodetector to measure the interference pattern and a beam splitter.

2.1.2 Homodyne and Heterodyne frequency

Interferometers can be characterized in terms of the frequency type used for detection, heterodyne or homodyne. Heterodyne interferometers use heterodyne frequency for the measurement of displacement with great long-range measurement ability and possesses noise immunity to variations in light intensity. Unlike homodyne interferometry, where only one frequency of laser light is used for both the reference and measurement arms of the interferometer, heterodyne interferometry uses different frequency in each arm. The difference between both frequencies (the heterodyne frequency) is obtained from a frequency shifting unit.

2.1.3 Spatial separation and perfect symmetry

Due to periodic nonlinearity of heterodyne interferometry, high accuracy measurements become difficult. Considering I_1 the measurement wave and I_2 the reference wave, the nonlinear time-varying component of the measurement signal at the photodetector is

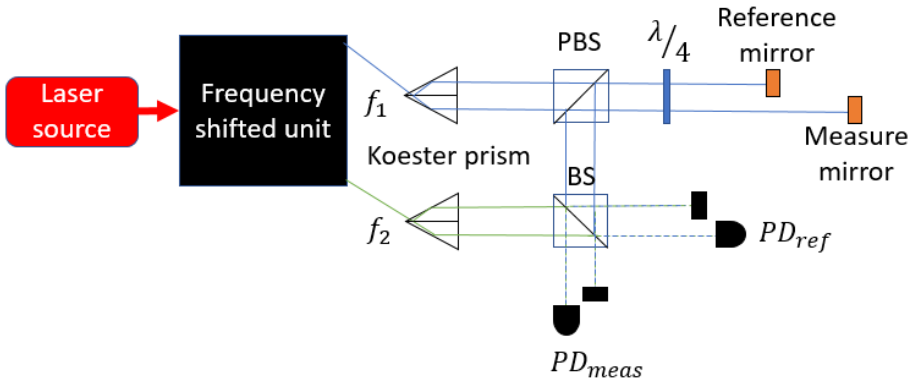

Figure 2.2: Example of heterodyne interferometry generation following the principles of spatial separation and perfect symmetry of the laser beams. PBS as polarized beam splitter, BS as beam spliter and $\frac{\lambda}{4}$ as quarter wave plate.

$$I_m \propto \overline{I_1 I_2}\cos(\Delta\omega t+\phi)+(\overline{I_1}\beta+\overline{I_2}\alpha)\cos(\Delta\omega t)+\left(\alpha\beta+\beta_{pf}\,\alpha_{pf}\right)\cos(\Delta\omega t-\phi)+ \\ \left(\overline{I_1}\,\beta_{pf}-\overline{I_2}\,\alpha_{pf}\right)\sin(\Delta\omega t)+\left(\alpha\,\beta_{pf}-\beta\,\alpha_{pf}\right)\sin(\Delta\omega t-\phi), \tag{2.7}$$

where the coefficients α, β, α_{pf} and β_{pf} represent the mixing of polarization, frequency or both. These issues appear due to either properties of the laser beam, ellipticity and nonorthogonality, or imperfection of beam splitters, ghost reflections and other related issues [13].

The mixing of frequency and polarization stops being a problem if there exists spatial separation between the two laser beams and if there exists perfect symmetry in the pathlength of the beams like in figure 2.2. Thus resulting in a linear time-varying signals at the measurement and reference photodetectors

$$\begin{cases} I_m \propto I_1\, I_2 \cos(\Delta\omega t+\phi) \\ \\ I_r \propto I_1\, I_2 \cos(\Delta\omega t) \end{cases} \tag{2.8}$$

with

$$\Delta\omega = 2\pi\left|f_1-f_2\right| \tag{2.9}$$

and the phase difference between the measurement and reference beams $\phi(t)$ can be expressed by integrating the Doppler effect between both targets resulting in

$$\phi = 2\frac{2\pi}{\lambda}\int dt\cdot v(t) = 2\frac{2\pi}{\lambda}s(t) \tag{2.10}$$

In 2.10, $v(t)$ represents the velocity of the measurement target, if reference target assumed stationary, so after integration the displacement between the measurement target, $s(t)$, is obtained[14].

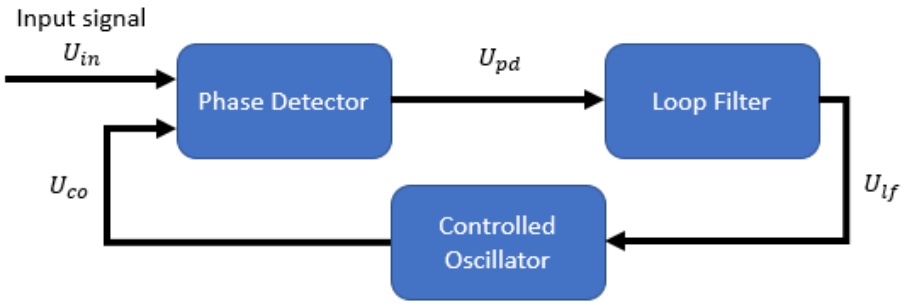

Figure 2.3: Block diagram of a PLL

2.2 Phase-locked loop

Phase locked loop (PLL) is a system composed of three main parts, figure 2.3, with the objective to generate an output signal with the same frequency as the input signal, preserving the input signal phase information and to eliminate noise artifacts.

The phase detector, which in this case is a frequency mixer, is responsible to compare the phase of the input signal and the controlled signal, providing information of the necessity of better tuning the controlled oscillator, to minimize the phase error, to the loop filter [15].

If the input signal

$$U_{in} = A_{in}\cos(\omega_{in}t + \varphi_{in}) \tag{2.11}$$

is compared with the controlled signal

$$U_{co} = A_{co}\cos(\omega_{co}t + \varphi_{co}) \tag{2.12}$$

results in

$$U_{pd} = U_{in} \cdot U_{co} \tag{2.13}$$

$$U_{pd} = K_{pd} \cdot A_{in} \cdot A_{co} \cdot \cos(\omega_{in}t + \varphi_{in}) \cdot \cos(\omega_{co}t + \varphi_{co}) \tag{2.14}$$

$$U_{pd} = \frac{1}{2} \cdot K_{pd} \cdot A_{in} \cdot A_{co} \cdot [\cos(\omega_{in}t + \omega_{co}t + \varphi_{in} + \varphi_{co}) + \cos(\omega_{in}t - \omega_{co}t + \varphi_{in} - \varphi_{co})] \tag{2.15}$$

Equation 2.15 is composed of three parts, the amplitude factor, where K_{pd} is the gain from the phase detector, a high frequency signal $\omega_{in}t + \omega_{co}t$ and a low frequency signal $\omega_{in}t - \omega_{co}t$. The high frequency signal is filtered by a low pass filter, from the loop filter, and since the ω_{in} and ω_{co} are the same or close, so $\omega_{in} - \omega_{co} \approx 0$. Thus, the signal after the loop filter is

$$U_{lf} = A_{pd}\cos(\varphi_{in} - \varphi_{co}) \tag{2.16}$$

which only depends on the phase difference between the input signal and the controlled oscillator signal.

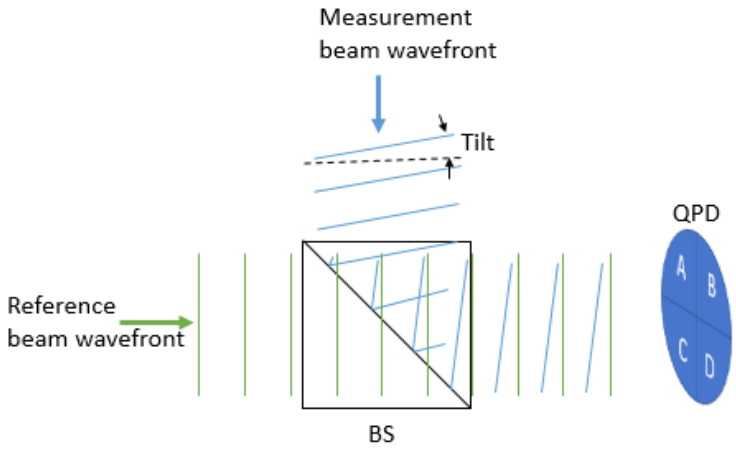

Figure 2.4: QPD with 4 quadrants (A, B, C and D), being used for DWS

2.3 Quadrant photo diode

Quadrant photodetector (QPD) is an electronic device mostly used for alignment applications and position sensing of laser beams due to its photo active area composed by a 2×2 array of individual photoactive cells. The use of QPD to detect the laser beams allows to make tilt measurements of the mirrors due to differential wavefront sensing (DWS)[16], as it can be seen in figure 2.4.

The wavefront reflected at the reference mirror is always constant unlike the measurement wavefront, which may present itself with a tilt. This tilt causes non-uniform phase shifts over the beam and can be measured by measuring the phase at two opposite individual photoactive cells. The most common orientation for the tilt measurement is,

- Orientation 1: QPD axis in parallel to plane:

$$\varphi_1 = \frac{\varphi_A + \varphi_B - \varphi_C - \varphi_D}{2}$$

$$\varphi_2 = \frac{\varphi_A + \varphi_C - \varphi_B - \varphi_D}{2}$$

- Orientation 2: QPD axis 45° out of plane

$$\varphi_1 = \frac{\varphi_A + \varphi_D - \varphi_B - \varphi_C}{2}$$

$$\varphi_2 = \frac{\varphi_B + \varphi_C - \varphi_A - \varphi_D}{2}$$

and is calculated

$$tilt = \frac{\Delta\varphi\lambda}{2\pi r} \tag{2.17}$$

In equation 2.17, r stands for radius of the laser beam and λ as the laser wavelength.

2.4 Acousto-optic modulator

Acousto-optic modulator (AOM) is used to control the frequency or spatial direction of a beam, as shown in figure 2.5.

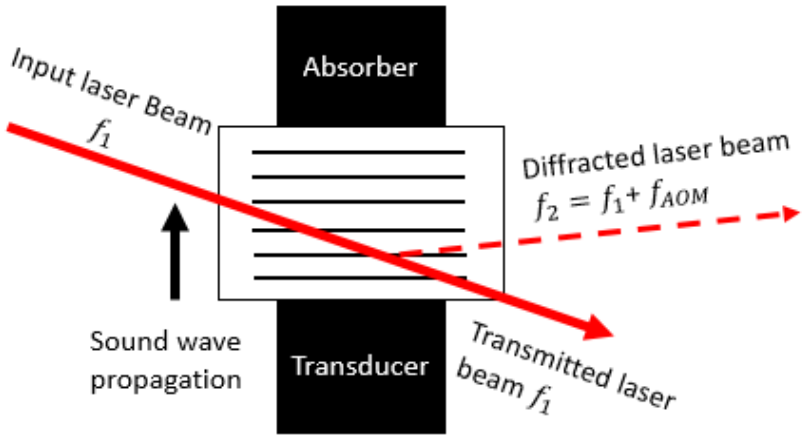

Figure 2.5: Acousto-optic modulator or AOM, the diffracted laser beam is exaggerated

This is accomplished by the transducer which upon receiving a signal to make a correction on the laser beam, generates a sound wave that causes mechanical pressure in the crystal or glass, where the beam is traveling, changing its refractive index making the beam experience Bragg diffraction.

2.5 Rotary encoder

A rotary encoder is a sensor composed of a light source, photodetector and rotation disk with a code track, which translates rotation position into digital pulse signals, figure 2.6.

The code track in the rotation disk is composed of opaque and transparent sectors. As the disk rotates these patterns block the light from arriving at the photodetector, thus creating digital pulses as shown in figure 2.7

This type of device cannot provide absolute position, but it can offer a high resolution approximation by using two output channels to sense position. These two code tracks in the rotation disk are composed of patterns 90° out of phase allowing not only high resolution positioning of the rotation disk but also its direction. Considering channel A and B, as shown in figure 2.7, if A leads B then the disk is rotating counterclockwise, if not then clockwise.

The encoders can be divided in three types:

x1 encoding - The encoder counts movement by detecting only rising edges or only falling edges of channel A. Channel B is used to detect the rotation direction.

x2 encoding - The encoder counts movement by detecting both rising and falling edges of channel A. Channel B is used to detect the rotation direction.

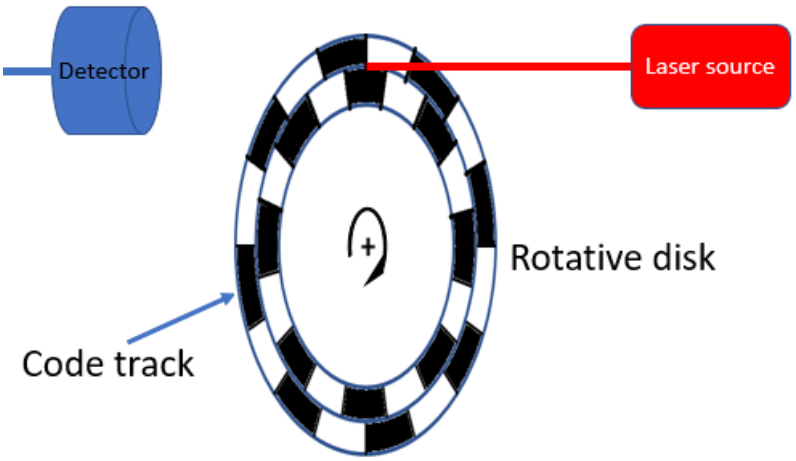

Figure 2.6: Schematic representation of the working principal of an optical incremental rotary encoder.

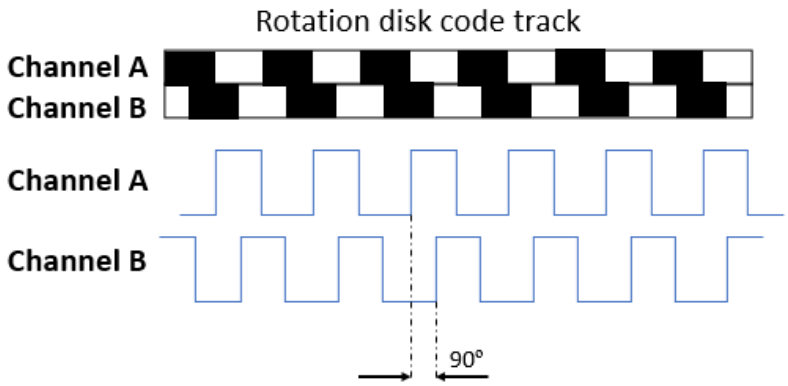

Figure 2.7: Schematic representation of the working principal of an optical incremental rotary encoder.

x4 encoding - The encoder counts movement by detecting both rising and falling edges of both A and B channels. This type of encoder has highest resolution.

Most encoders also include another feature called the reference signal (MKP), which sends a digital pulse signal for every full rotation of the rotation disk.

2.6 Differential signaling

Differential signaling is a technique which offers high immunity against electromagnetic impact in transmission lines. This technique, as shown in figure 2.8, transmits information via two complementary or differential pair signals.

These signals are commonly transmitted in twisted pair cables, so noise affects both transmission lines identically. When both signals arrive a differential receiver unit, the noise is removed leaving the signal intact.

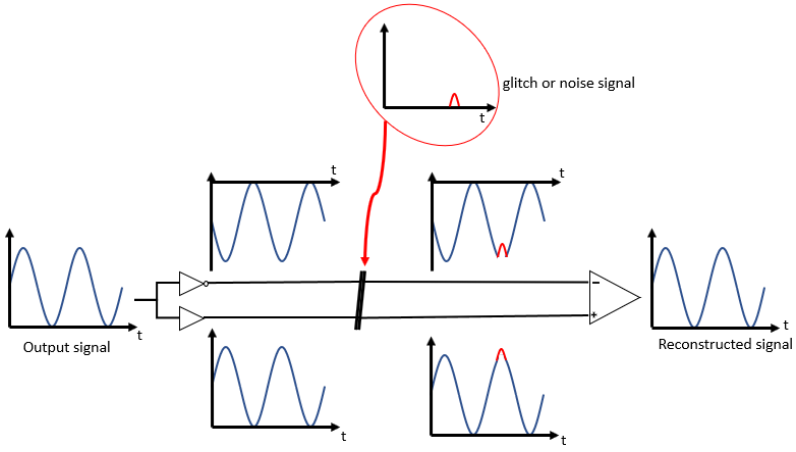

Figure 2.8: Schematic representation of differential signaling.

Chapter 3

Experimental Setup

In this chapter the experimental setup used to achieve a single diameter measurement will be shown and explained in four parts: mechanical setup, the optical setup, digital data analyzes and measurement results.

The optical setup will describe the used optical components, mathematical analyses and laser beam pathway in order to measure displacement, while in the mechanical setup the designs of the vacuum chamber, SPM support and reference mirrors are explained. In the digital analyzes section, demonstrates how the displacement is calculated and how a circumference map of the SPM is achieved. Lastly the measurement results are shown.

3.1 Mechanical setup

In figure 3.1 are shown the components mentioned in the previous section in their physical form inside the vacuum chamber which operates at a pressure of $p_{vacuum} \approx 50 - 100$ mbar . The aluminum chassis IFO1 and IFO2, contains the optic components necessary to measure the displacement in the surface of the SPM. The spherical lenses used to focus the beam on the surface of the SPM are mounted on adjustable three-axial linear stages.

3.1.1 Spherical proof mass support and reference mirrors support

The SPM support is fixed to the rotational stage with a spring ring over the little spheres in the base plate, so it rotates as the rotational stage rotates with the rotation axis and direction indicated in figure 3.2. Also in the figure, a rotative mechanism is present which allows for a shift in the initial angle position of the SPM.

In figure 3.3 both SPM support and reference mirrors support are assembled together. The reference mirror support has a hole in the center of the plate to position the SPM.

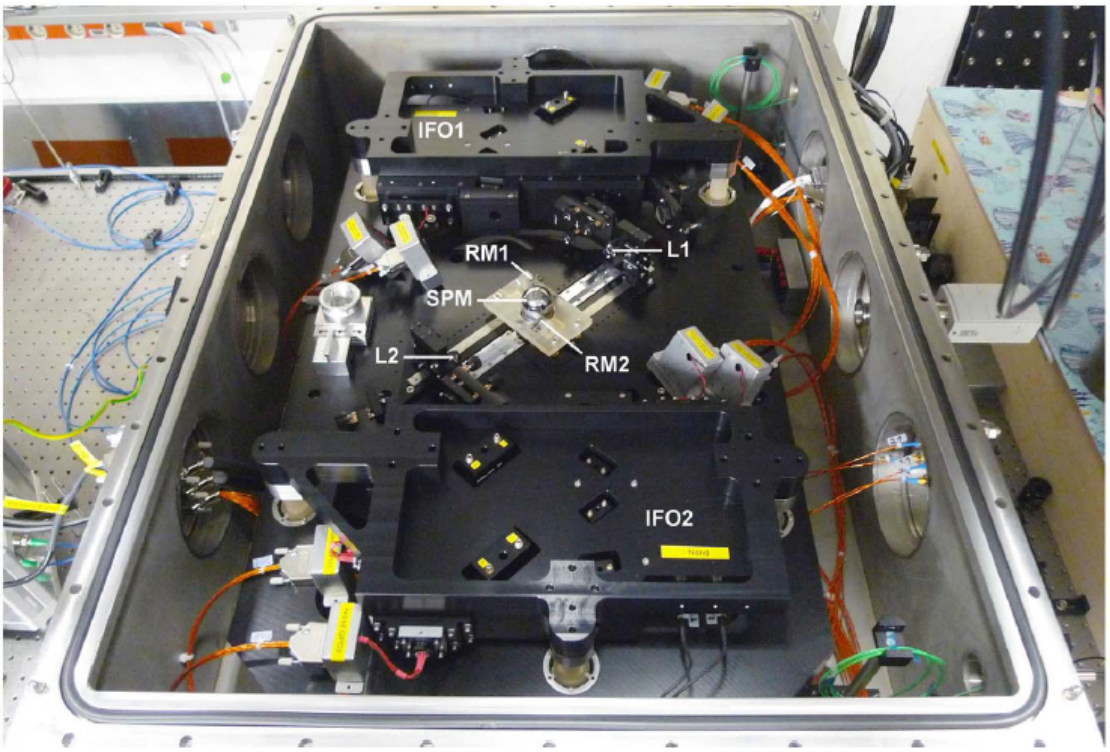

Figure 3.1: Vacuum chamber with double interferometers (IFO1 and IFO2) and SPM in the center[17]

Table 3.1: SPM properties[18]

Parameters	Dimension
Nominal diameter	40 mm
Max diameter deviation	$11,5\ \mu m$
Max diameter fluctuation	$0,5\ \mu m$
Roughness	$0,032\ \mu m$
Mass	$0,4963 kg$

The reference mirrors (RM1 and RM2) have the possibility of being oriented using flexure hinges and tiltable plate.

The SPM used to carry out this experiment is a commercially common tungsten carbide ball used for large ball bearing, quality Class G20 according to DIN5401 with the parameters in table 3.1.

3.2 Optical setup

The experimental setup designed at Airbus D&S uses a double interferometer with heterodyne frequency of 10 kHz, spatial separation of the different frequency beams and perfect symmetry. The interferometers are fed by a Nd:YAG NPRO laser Innolight Mephisto NE500, at 1064 nm. The laser beam is split by a beam splitter originating two other

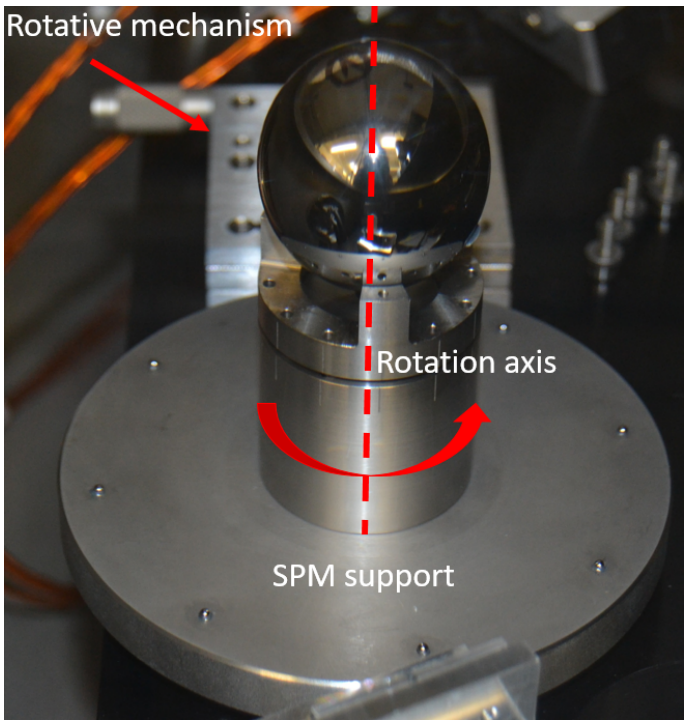

Figure 3.2: Rotation support for the SPM on top with the little support spheres in the base plate.

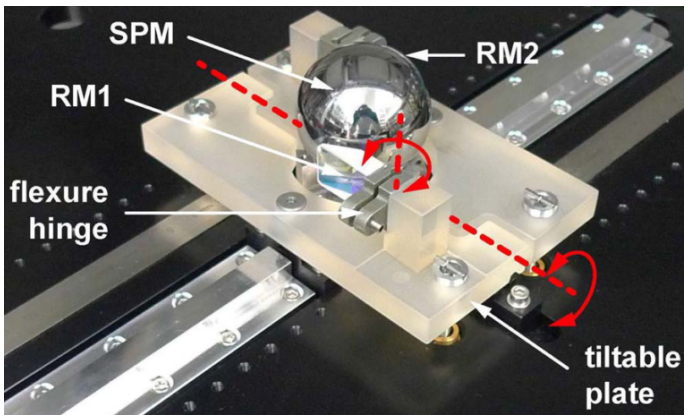

Figure 3.3: Reference mirrors support plate [17]

beams. These beams suffer a frequency shift by the AOMs, here is where heterodyne frequency of f_{het} = 10 kHz is established, figure 3.4. After having defined two beams with different offset frequencies of 78.00 MHz and 78.01 MHz, these are transported via optical fibers to the vacuum chamber.

With the beams inside the vacuum chamber, figure 3.5, the beam f_1 is detected by PD_1 and beam f_2 is detected by PD_2. PD_1 and PD_2 are responsible for controlling the intensity of the two beams via modulating the AOMs. Further along, each beam is yet again split in two other beams by a Koester prism, figure 3.6. The beams with frequency f_1 travel through adjustable mirrors (AMs), which allow for manual correction of the beam

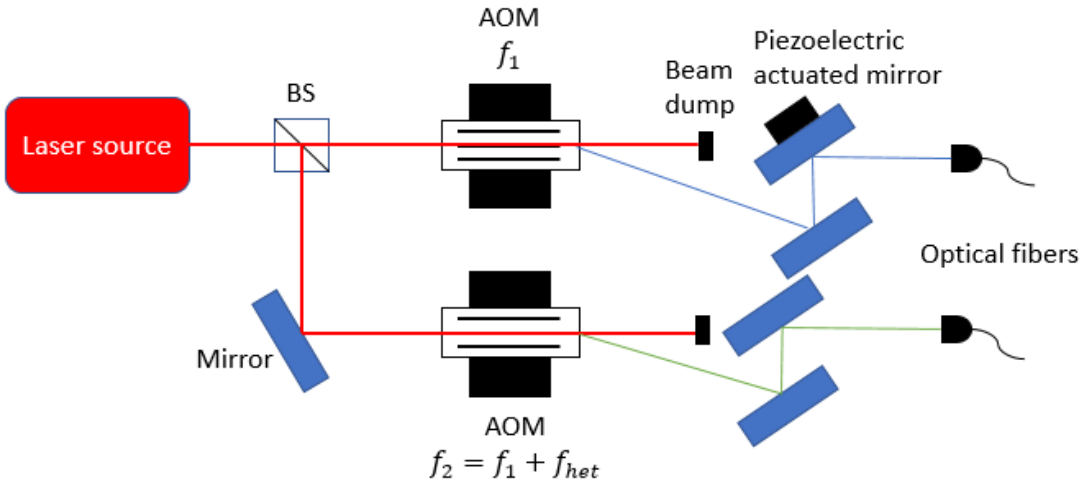

Figure 3.4: Simplistic schematic of the heterodyne frequency generation with spatial separation and symmetric design in use.

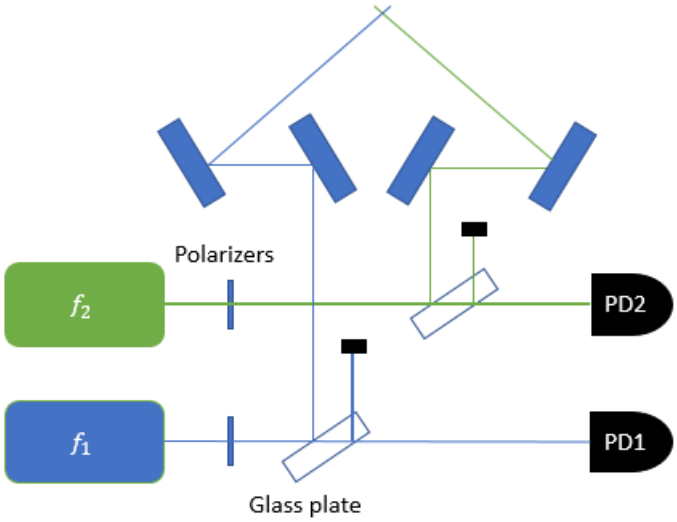

Figure 3.5: Inside the vacuum chamber with photodiodes (PD).

direction tilting, reaching a beam splitter and are redirected to the QPDs. The beams with frequency f_2 hit a polarized beam splitter and then go through a quarter wave plate circularly polarizing the beams. The same beams go through another system of AMs and are redirected to the surface of the SPM and reference mirrors. The measurement beam is focused on the surface of the SPM via plano-convex lens with a focal length of ≈ 100 mm resulting in a measurement beam diameter at the SPM of $D_{meas} = 175\ \mu m$. The beams are reflected back to the quarter wave plate, become linearly polarized again, and then reflected towards the beams of frequency f_1 where they superimpose and are directed towards QPD_1 and QPD_2. The signals detected by the QPDs are averaged over the beam cross-section, thus resulting in a low pass filtering of the measured topography for spatial frequencies higher than $2/\pi . D_{meas}$ or angular frequencies higher than $1.27/°$. The $QPDs$

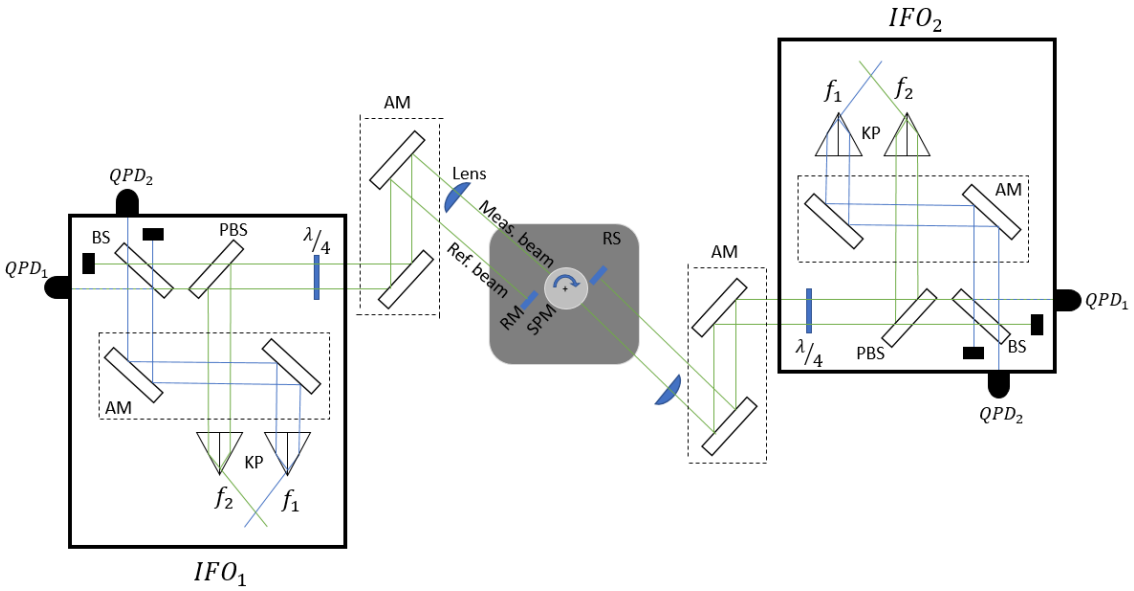

Figure 3.6: Beams are reflected back from the surface of the SPM and reference mirrors (RM), and it's possible to calculate the displacement. PBS stands for polarized beam splitter, BS as in beam splitter, $\frac{\lambda}{4}$ for quarter wave, KP is Koester prism, AM as adjustable mirrors and RS as rotational stage.

will detect the superimposed beam of f_1 and f_2 and control the piezoelectric actuated mirror to adjust the path length in figure 3.4, adjusting thus the phase.

The light intensity directed to QPD_1, or reference QPD, is

$$I_r = A_{f1} \cdot A_{f2} \cos(\Delta\omega t) \tag{3.1}$$

and direct to QPD_2, or measurement QPD, is

$$I_m = A_{f1} \cdot A_{f2} \cos(\Delta\omega t - \Delta\phi(t)) \tag{3.2}$$

In the equations 3.1 and 3.2, A_{f1} is the amplitude of the beam with frequency f_1, A_{f2} is the amplitude of the beam with frequency f_2, $\Delta\omega$ is the heterodyne frequency and $\Delta\phi(t)$ is the phase difference between the measurement and reference signals.

3.3 Digital data analyzes

3.3.1 Field Programmable Gate Array

The Field programmable gate array (FPGA) is a device that allows the user to program the hardware rather than writing software to run in a pre-designed processor like in micro-controllers. This means that the FPGA is a collection of several thousands of configurable logic blocks composed of simple logic functions, like a flip-flop, a look-up table and a multiplexer, and In/Out blocks which can either read or send signals. These configurable logic blocks or CLBs, can be connected between each other to implement complex logic functions.

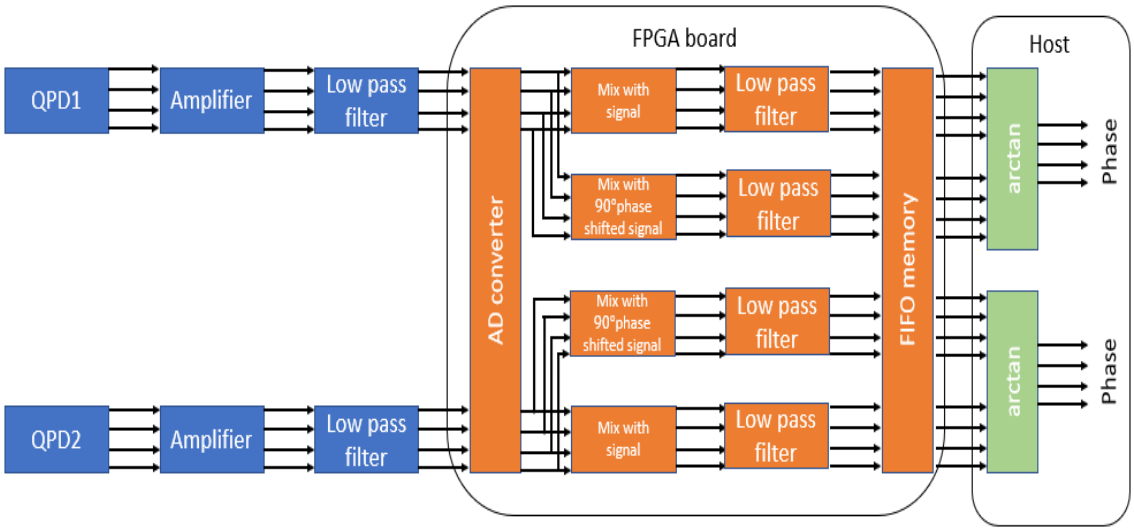

Figure 3.7: FPGA board and host signal analysis.

The FPGA used in this experimental setup is a PXI RIO 7854R from National instruments, with a maximum data processing speed or single cycle loop speed of 40 MHz.

Both the FPGA and host are coded in LabVIEW.

From the QPDs, eight signals are obtained, figure 3.7. These signals in the FPGA board are divided in two identical signals to do an in-quadrature measurement, at a speed of 160 kHz. An in-quadrature consists in multiplying two identical signals with two other signals internally generated by the FPGA board, in all equal but with a 90° phase shift relative to each other.

In the FPGA board, these signals are obtained:

$$\begin{cases} S_1 = I_m \cdot \cos(\Delta\omega t) = A_{f1} \cdot A_{f2} \cdot \cos(\Delta\omega t - \Delta\phi(t)) \cdot \cos(\Delta\omega t) \\ \\ S_2 = I_m \cdot \sin(\Delta\omega t) = A_{f1} \cdot A_{f2} \cdot \cos(\Delta\omega t - \Delta\phi(t)) \cdot \sin(\Delta\omega t) \end{cases} \tag{3.3}$$

To the equations above, a low pass filter with a cut-off frequency of 6 Hz is applied to filter out the high frequency part thus, resulting in

$$\begin{cases} S_1 = \frac{1}{2} A_{f1} \cdot A_{f2} \cdot \cos(\Delta\phi(t)) \\ \\ S_2 = \frac{1}{2} A_{f1} \cdot A_{f2} \cdot \sin(\Delta\phi(t)) \end{cases} \tag{3.4}$$

After the signals are low pass filtered, these are stored in a First in first out (FIFO) memory at a frequency of 20 Hz.

3.3.2 Host program

The host program in the workstation, removes the data from the FIFO at a maximum speed of $20Hz$ and proceeds with the calculation of the phase signal, which is given by

$$\phi(t) = \arctan\left(\frac{S_2}{S_1}\right) \tag{3.5}$$

Since the phase difference between the measurement signal and the reference signal is directly proportional to the displacement, the following equation can be derived

$$\Delta\phi(t) = \frac{4\pi n}{\lambda}\Delta l(t) \tag{3.6}$$

where n is the refractive index of the medium in which the light travels and the λ is the wavelength of the used laser beam.

As the host program calculates the displacement values, it also records the corresponding angular position. This angular position is obtained via ethernet connection between the host program and the rotational stage encoder. Thus resulting in a map of a single circumference of the SPM.

3.4 Measurement results

With the described setup, various systematic and stochastic noise sources have to be taken into consideration for the possibility to map topographically a single circumference of the SPM. Such noise sources are:

- Mechanical and thermal deformations in the setup.
- Radial and axial error movements of the SPM.
- Eccentricity of the rotation axis.

3.4.1 Noise Sources

In order to study if the measurement of the SPM topography is invalidated due to performance and accuracy issues caused by mechanical and thermal deformations in the system, a test measurement was done with the SPM static (no rotation motion).

As seen in the figure 3.8, the effects of thermal and mechanical noise in this experimental setup are neglectable due to the picometer noise displacement for $10^{-3} - 10^{0}$ Hz frequencies and few nanometer displacement for frequencies lower than 10^{-3} Hz.

These results prove that mechanical and thermal fluctuations are not limiting factors in the measurements.

The model of correction used is shown in figure 3.9. In this model C_{IFO} is the center position of measurement between both interferometers, C_{SPM} is the geometric center of mass of the SPM, x_1 and $-x_2$ are the measurement signals of each interferometer where the negative sign of x_2 comes in opposition to the measurement direction of x_1, misalignment of the rotational stage generates $\vec{c}$ which is a static offset between the rotation axis and reference frame, $\vec{s}$ is the dynamic radial and axial error movements of the rotation axis due to ball bearing in the rotational stage, $\vec{d}$ represents the eccentricity caused by the offset between rotation axis and SPM geometric center, $\vec{m}$ is the position of the C_{SPM} in relation to the C_{IFO}, φ and φ_{SPM} are the rotation angles of the rotational stage and SPM respectively.

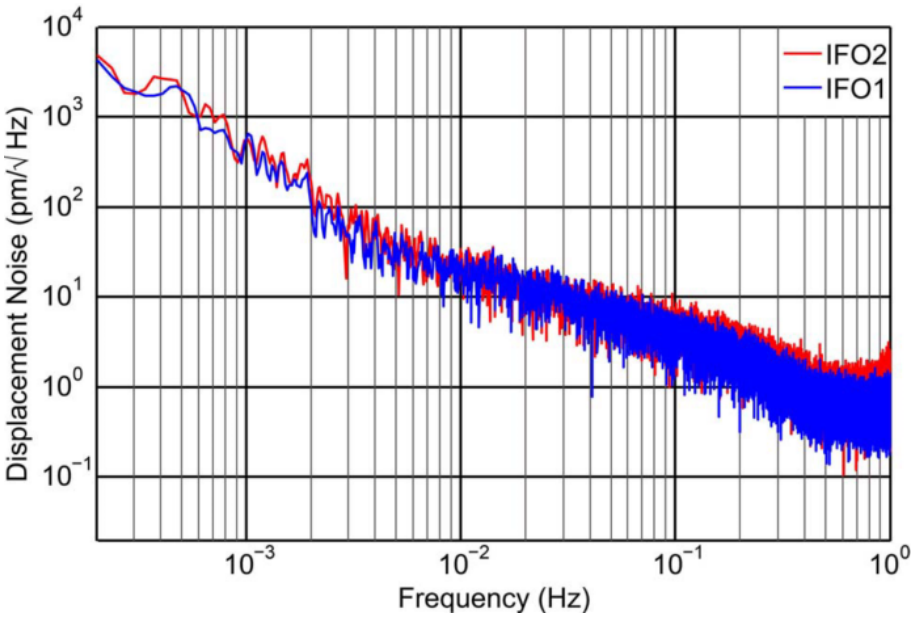

Figure 3.8: Mechanical and thermal noise displacement evaluation, showing a high symmetry of the two interferometers and the neglectable effect of these disturbances in the measurements.[17]

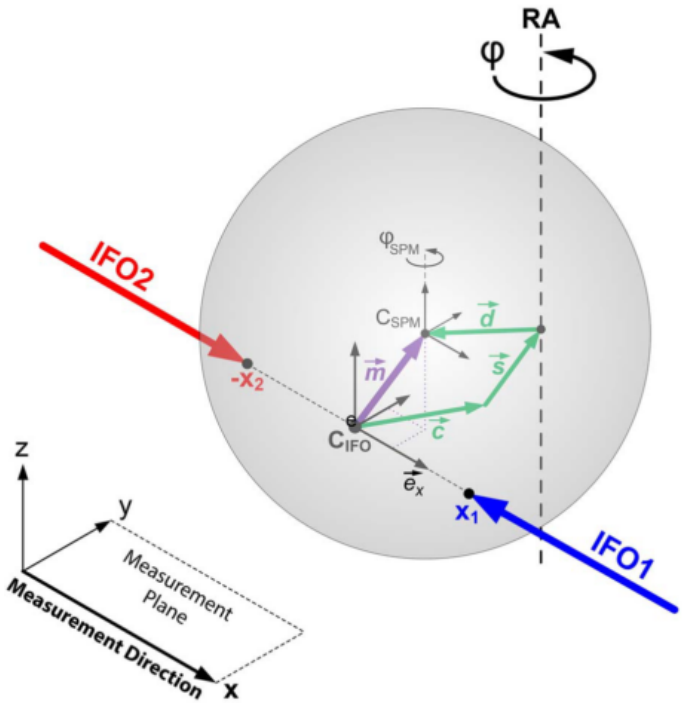

Figure 3.9: Schematic model of the geometry.[17]

The component $\vec{m}$ is calculated by

$$\vec{m} = \vec{c} + \vec{s} + \vec{d} \tag{3.7}$$

since the component $\vec{s}$ is composed of synchronous error movements, which repeat itself

every 2π interval, and asynchronous error movements, $\overrightarrow{m}$ can be expressed as

$$\overrightarrow{m}(\varphi) = \overrightarrow{c} + \overrightarrow{s_{se}}(\varphi) + \overrightarrow{s_{ae}}(\varphi) + \overrightarrow{d}(\varphi) \tag{3.8}$$

Asynchronous movement errors can be ignored if averaging of the measurements is done and $\overrightarrow{d}(\varphi) = d\overrightarrow{e}_d(\varphi - \varphi_d)$ with $d = \left|\overrightarrow{d}\right|$ and $\overrightarrow{e}_d(\varphi - \varphi_d) = \begin{pmatrix} \cos(\varphi - \varphi_d) \\ \sin(\varphi - \varphi_d) \\ 0 \end{pmatrix}$, results in

$$\overrightarrow{m}(\varphi) = \overrightarrow{c} + \overrightarrow{s_{se}}(\varphi) + d\begin{pmatrix} \cos(\varphi - \varphi_d) \\ \sin(\varphi - \varphi_d) \\ 0 \end{pmatrix} \tag{3.9}$$

Considering a sphere of radius R

$$R^2 = \left[\pm x_{1,2}(\varphi)\,\overrightarrow{e_x} - \overrightarrow{m}(\varphi)\right]^2 \tag{3.10}$$

the solutions are

$$x_{1,2}(\varphi) = R\sqrt{1 - \frac{m_y^2(\varphi) + m_z^2(\varphi)}{R^2}} \pm m_x(\varphi) \tag{3.11}$$

and describing the SPM surface $\hat{p}(\varphi, \theta)$ with spherical coordinates

$$R^2 = \frac{1}{4\pi}\int_0^{\pi}\int_0^{2\pi} \hat{p}^2(\varphi, \theta)\sin(\theta)\,d\varphi d\theta \tag{3.12}$$

with $\theta = \frac{\pi}{2}$, results in

$$x_{1,2}(\varphi, \varphi_{SPM}) \approx \hat{p}\left(\frac{\pi}{2} - \varphi \pm \left(\frac{\pi}{2} + \frac{c_y}{R}\right) + \varphi_{SPM}\right)\sqrt{1 - \frac{m_y^2(\varphi) + m_z^2(\varphi)}{R^2}} \pm m_x(\varphi) \tag{3.13}$$

The equations 3.13 represent the measurement signals of the interferometers, in which dependencies exist from the misalignment between the rotational axis and C_{IFO}, $\frac{c_y}{R}$, and the relative rotation of the SPM enabled by the support, φ_{SPM}.

In table 3.2 are shown the error intervals of the parameters mentioned in the correction model 3.9 for one rotation. The error margins of $\left|\overrightarrow{c}\right|$, d and $\left|\overrightarrow{s}\right|$ are higher than the surface topography error, therefore these errors have to be removed. In order to do so, measurements with several rotations were made. This allowed to remove the x-offset, $c_x = 0$, by subtracting the mean values from the interferometer signals leaving the y-offset c_y and eccentricity d. These two parameters can be estimated with a Taylor expansion of equation 3.11, with scalar product $\xi_{1,2} = \left\langle e^{i\varphi} \middle| x_{1,2}(\varphi) \right\rangle$ and ignoring the rotation stage error movements, $\overrightarrow{s} = 0$, resulting in

Table 3.2: Calculated error parameters for one rotation measurement

Parameters	Error dimension
$\left\|\overrightarrow{c}\right\|$	$\approx 10-20\ \mu m$
d	$\approx 10-20\ \mu m$
$\left\|\overrightarrow{s}\right\|$	$\approx 1-2\ \mu m$
SPM surface topography	≈ 100 nm

$$\xi_{1,2} = \pm\frac{d}{2}\, e^{i\left(-\varphi_d \pm \frac{c_y}{R}\right)} + dO\left(\frac{c_y}{R}\right)^2 \tag{3.14}$$

where

$$\begin{cases} c_y \approx \frac{R}{2}\left[\arg(\xi_1) - \arg(\xi_2)\right], \\ d \approx |\xi_1| + |\xi_2|, \\ \varphi_d \approx -\arg(\xi_1 - \xi_2). \end{cases} \tag{3.15}$$

From here corrected interferometer signals $x^c_{1,2}$ can be calculated

$$x^c_{1,2} = x_{1,2}(\varphi, \varphi_{SPM}) \mp d\cos(\varphi - \varphi_{SPM}) + \frac{\left[c_y + d\cos(\varphi - \varphi_{SPM})\right]^2}{2R} \tag{3.16}$$

In equation 3.16 the parameters d and φ_d, which are errors of eccentricity caused by an offset between the rotation axis and C_{SPM}, have to be calculated for each measurement due to random variations of their value because of the lash suffered by the SPM support. The parameter c_y also suffers slight variations but these are due to thermal drifts caused by long measurement times which influence beam alignment and SPM position.

In previous calculations the influence of error movements by the rotational stage were ignored. Taking these error into consideration, the $\overrightarrow{s}$ component is calculated by removing the surface topographic contributions of the SPM from the measurement data with different initial angle φ_{SPM}, resulting in

$$s_x(\varphi) \approx \frac{x^c_1(\varphi, 0) - x^c_2(\varphi, 0) + x^c_1(\varphi, \pi) - x^c_2(\varphi, \pi)}{4} \tag{3.17}$$

and

$$\sigma(\varphi) = \frac{s_y(\varphi)\, c_y + s_z(\varphi)\, c_z}{R} \tag{3.18}$$

In order to estimate the value of $\sigma(\varphi)$ using the equation 3.17 resulted in a hard to solve ambiguity, hence a solution without high frequency content is used, resulting in

$$p_{1,2}(\varphi, \varphi_{SPM}) = \hat{p}_{1,2}(\varphi, \varphi_{SPM}) - R \approx x^c_{1,2}(\varphi, \varphi_{SPM}) \mp s_x(\varphi) + \sigma(\varphi) \tag{3.19}$$

3.4.2 Results

The results of the SPM surface topography shown in the following figures 3.10, 3.11 and 3.12, were measured at a SPM rotation velocity of $\approx 1,2°/\text{sec}$ and a sampling frequency of 20 Hz.

In figure 3.10 the topography p_1 is first measured with several revolutions, ≈ 80, per different $-\varphi_{SPM}$ shifts and then averaged, $\overline{p}_1$, and the deviation between the measurements with different $-\varphi_{SPM}$ and the averaged value, ϵ_R, are used to calculate for each different measurement the standard deviation which resulted in $\sigma_R \approx 7-18$ nm. The result topography p_1 is shown in polar coordinates in figure 3.11.

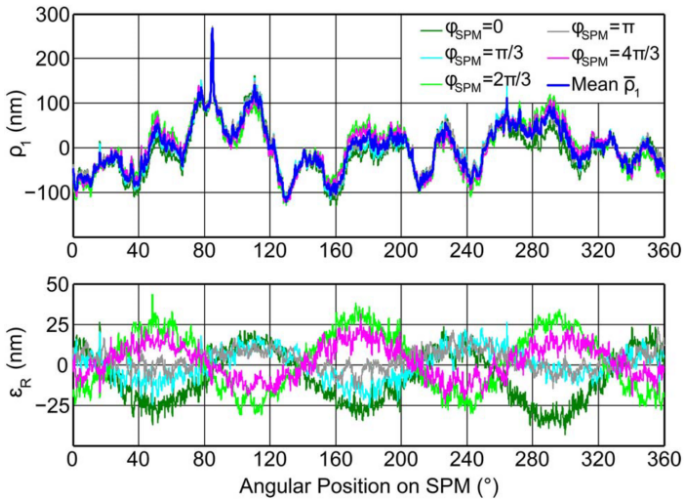

Figure 3.10: Measurement of the SPM surface on the top, p_1, and deviation on the bottom, ϵ_R.[17]

In figure 3.12 is shown the double interferometer measurement of the surface with a standard deviation of $\approx 5-8$ nm which is smaller than for just one interferometer with surface p_1. Although with this measurement the topography repeats itself after $\varphi \approx 180°$ losing therefore the circumference topography of the SPM, it can be used in terms of calibration and to generate a more accurate SPM surface map because there is a compensation of the error s_x duo to both interferometers measuring in opposite directions, resulting in a lower standard deviation for double interferometer measurement compared with single.

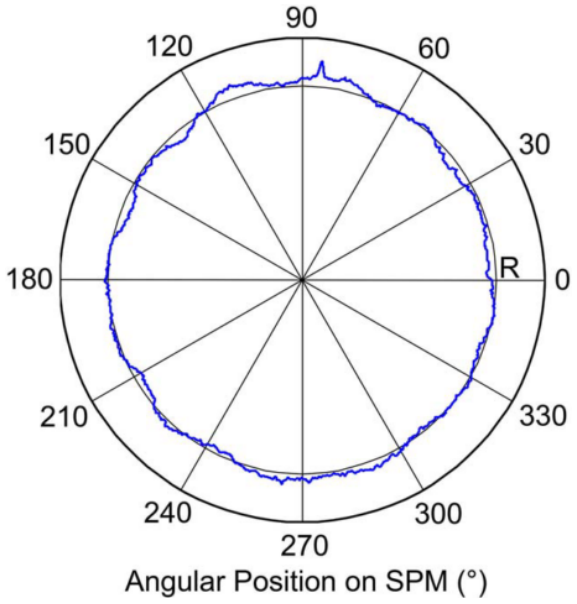

Figure 3.11: Measurement of the average SPM surface in polar coordinates exaggerated by a factor of $\approx 10^4$ between R and the topographical effects.[17]

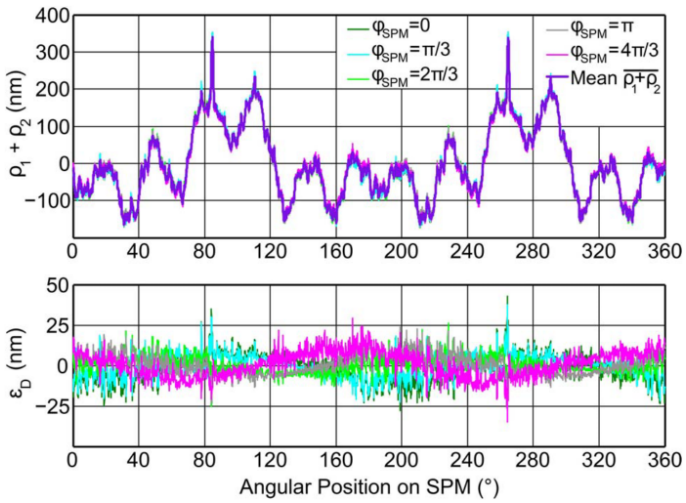

Figure 3.12: Sum measurement for both interferometers on the top and on the bottom the deviation ϵ_D.[17]

Chapter 4

Experimental setup for 2D surface topography

In this chapter, the proposed experimental setup changes to achieve complete 2D surface topography measurement, will be analyzed and explained.

4.1 Proposed experimental setup

With the previously described experimental setup, it is only possible to measure a single circumference of the SPM, if a complete surface map is to be measured, another degree of freedom needs to be added.

The proposed experimental setup shown in figure 4.1 includes several changes to the original experimental setup, which are:

- Second degree of freedom added with a second rotational stage
- Encoder for the new rotational axis
- Substitution of the reference mirrors with one ring shaped reference mirror
- Added optic components such as periscope, cylindrical lenses and a different set of adjustable mirrors

4.1.1 Second rotational stage

This rotational stage is responsible for an independent motion from around the θ axis as shown in figure 4.2, providing the necessary motion to measure several circumferences of the SPM concluding in mapping of the entire surface.

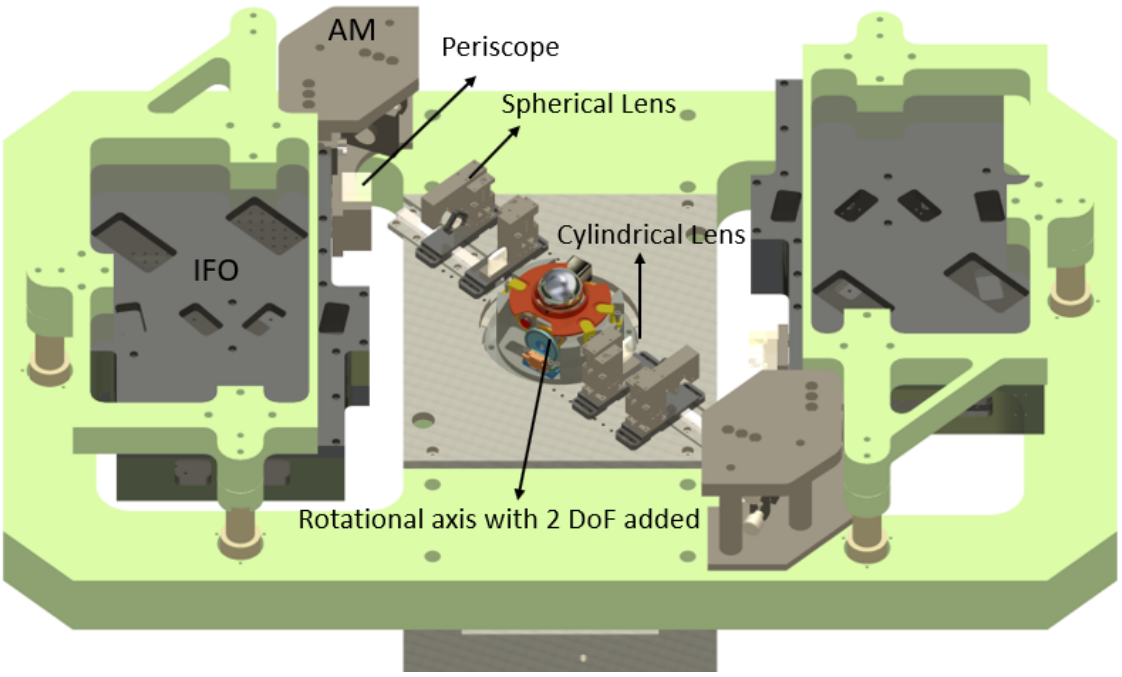

Figure 4.1: Schematic of proposed experimental setup. ADAPTED [19].

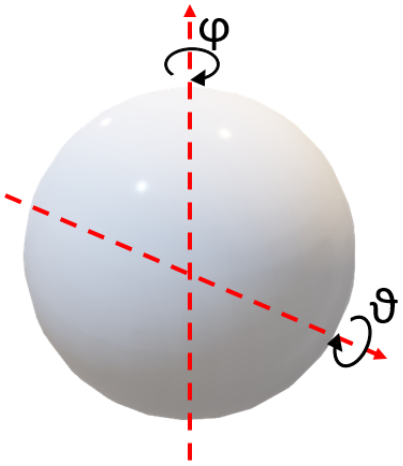

Figure 4.2: Schematic of the SPM with two possible rotational axis.

There are two possible ways to successfully measure the SPM surface, either with both rotational stages rotating at the same time, "simultaneous"option, or the second rotation stage makes a step per revolution of the first rotational stage, "one step per revolution"option. Both ideas were carefully analyzed but the simultaneous option although faster than the other and with more even density of measurement points along the surface, it would imply similar values of accuracy like the first rotational stage and highly difficult designing. therefore the later option was chosen, although this option results in an uneven density of measurement points specially at the poles, $\varphi = \pm 90°$ and $\theta = 0°, 180°$.

Figure 4.3 exemplifies how the measurement with the chosen method is done. After every $\varphi = 2\pi n$, n is a natural number, a measurement of a single circumference is done

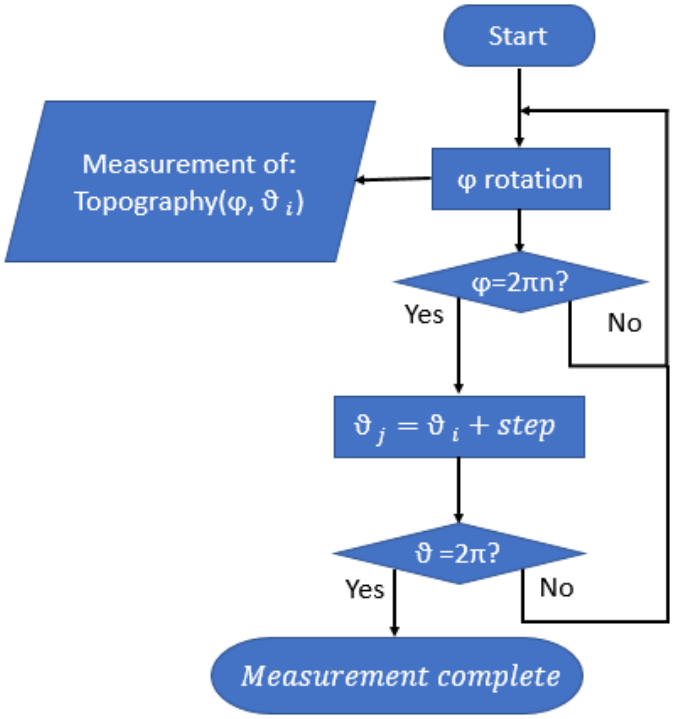

Figure 4.3: Flowchart of the logic behind the chosen method of measuring, one step per revolution.

and after $\theta = 2\pi$ a complete set of circumferences have been measured culminating in the figure 4.4, which is the plot of topography equation $p_{1,2}(\varphi, \theta)$.

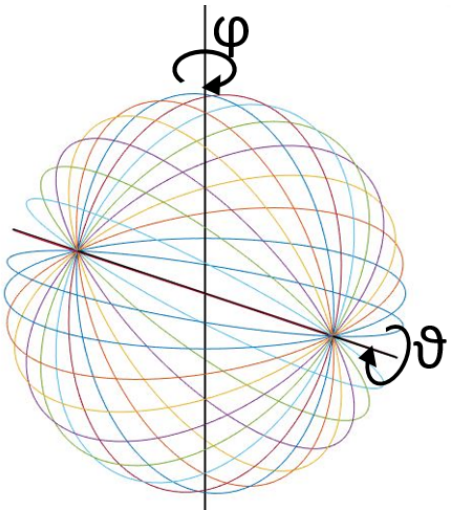

Figure 4.4: Schematic of a complete surface mapping, the step angle of θ is exaggerated.

In order to cover the surface as much as possible, the maximum distance between each measured circumference, or the step size, cannot be larger than

$$2 \cdot \left(2 \cdot \frac{D_{meas}}{D_{SPM}} \right) = 0.0175 \text{ rad}, \tag{4.1}$$

with a resolution of ≈ 8.75 mrad.

Besides being able to supply the SPM with a second degree of freedom, the second rotational stage must also be able to pinpoint the SPM position with high accuracy. For this the second rotation stage was designed based on the so called "friction wheels"solution. This solution is a system composed of two or more wheels in contact, in which the rotation in one of the wheels results in the rotation of the others, due to a electrostatic bonding of the molecules between both surfaces at the points of contact.

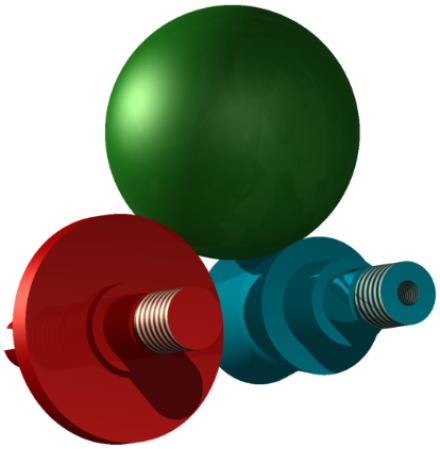

Figure 4.5: Schematic representation of the working principal of "friction wheels"with SPM (green), driver (red) and carried (blue conical wheel).

In figure 4.5 the working principal of the "friction wheels"is exemplified. The carried and the driver provide the SPM three points of contact to ensure a stable position. Since the position of the SPM cannot be directly measured, the carried is connected to a motor which will induce a rotation motion in the carried, thus rotating as well the SPM which also rotates the driver. The driver is connected to an encoder which will thus measure indirectly the position of the SPM.

In order to proceed with the design of the second rotation stage, a study of the geometrical characterization and force equilibrium of the system has to be done.

4.1.1.1 Design

Geometrical characterization and equilibrium of forces study is made in reference [19], to calculate the ratios between points of contact and rotation axis, and the exchanges of forces between the system required to provide basic guidelines on design of the second rotational, figure 4.6, with radius in table 4.1.

The encoder used in figure 4.6 is an Atom optical x4 incremental rotary encoder from Renshaw with a rotational disk with an exterior and interior diameter of 36 mm and 12 mm respectively. The rotational disk is composed of two line tracks, each with 5000 transparent and opaque pattern repetitions. Since the encoder is x4 type, has a total 20000 counts per total revolution with a resolution:

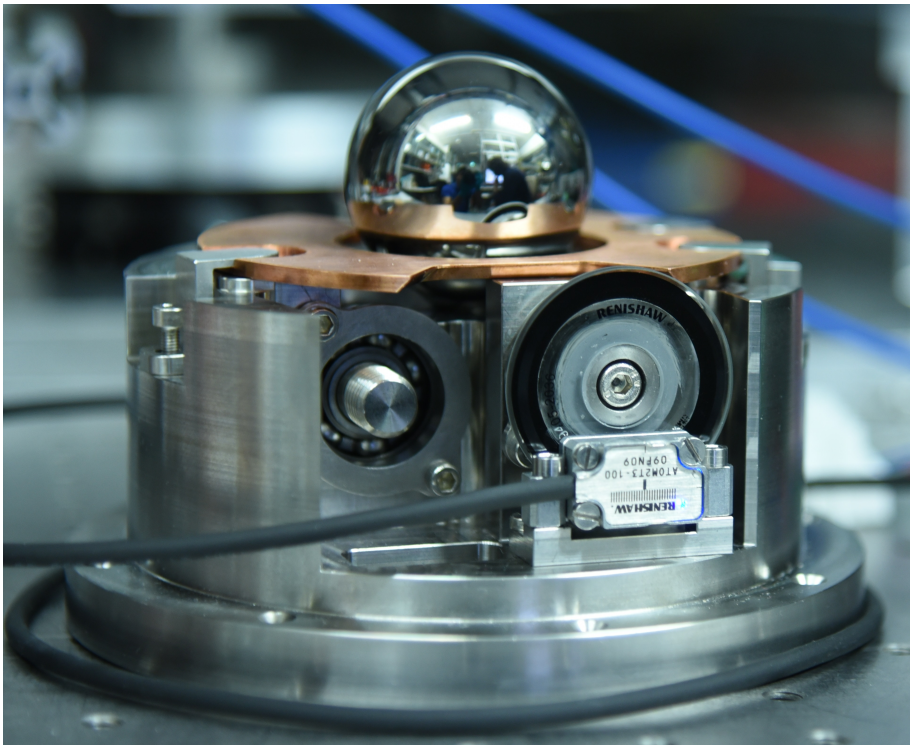

Figure 4.6: Picture of assembled second rotational stage.[19]

Table 4.1: Geometrical characterization

Parameters	Dimension
driver radius r_d	18 mm ±0.01
carried radius r_c	9.72 mm ±0.07
SPM radius r_{tm}	19.9 mm ±0.01
distance between SPM and carried centers d_c	19.6 mm ±0.02

$$\delta\theta_d = \frac{2\pi}{20000} \approx 0.314 \text{ mrad} \tag{4.2}$$

As a result of the choice "one step per revolution"method, the motor chosen for this application was a NEMA8 stepper motor connected to a step motor driver.

4.1.1.2 New reference mirror

In the previous experimental setup the reference mirrors were static while the SPM rotated along the first rotational stage axis. This situation was designed for a simpler optical setup but made the data more susceptible to eccentricities and noise from the rotation stage.

If the reference mirrors were to be had in the same conditions as the SPM, rotating along the first rotational stage axis in the same support as the SPM, then these eccentricities and noise would also be suffered by the reference mirrors resulting in topography data no longer being influenced by the s_x, therefore more accurate. Also the shape of

the reference mirrors would need to be changed, since a necessary requirement for this type of measurement is that the reflective surface of the reference mirror must be always perpendicular to the laser beam.

To accommodate the changes mentioned above, the new reference mirror is ring shaped and not flat like the previous model. The reference mirror used is made out of a copper ring with an external and internal diameter of 49 mm$\pm$2μm and 44 mm respectively, axial length of 7 mm and 98% of reflectivity.

4.1.2 New optical pathway

Having the second rotational stage designed, it is possible to observe the incompatibility between it and the used optical pathway outside the interferometers. Previously with the flat reference mirrors, the reference and measurement beams were horizontally parallel, but since theses mirrors were exchanged with a ring shaped mirror, the optical pathway had to be changed according to figure 4.7.

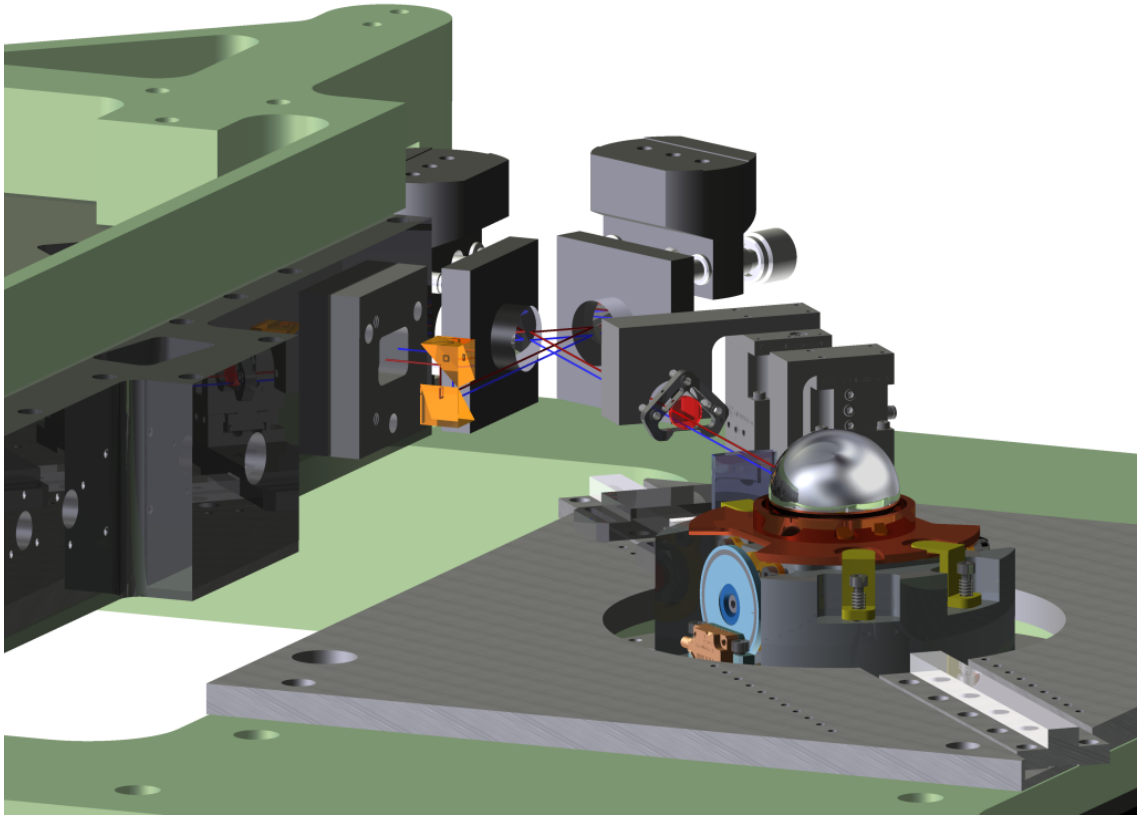

Figure 4.7: New optical pathway with a periscope, new set of adjustable mirrors and the addition of cylindrical lens.

In figure 4.7, several changes to the old optical pathway can be observed.

The first major change in the setup is the implementation of a periscope to rotate the laser beams by 90°. A periscope is a set of two right angle mirror prisms which reflect

the laser beams rotating them by 90°. The periscope used is composed of mirror prisms of 12.5 mm x 12.5 mm glued on a common glass plate which is glued on the aluminum support fixed on the interferometer chassis via bolt connections.

Any length difference which may result from using the periscopes to rotate the laser beams is disregarded, since the data gathered is not measured in absolute value but measured relatively to the first measurement point.

The second change in the optical pathway is a new set of adjustable mirrors which in total reflect the laser beams 45° directed to the SPM and the reference mirror. These adjustable mirrors are mounted in an aluminum structure which side plate is bolted to the interferometer chassis, figure 4.8

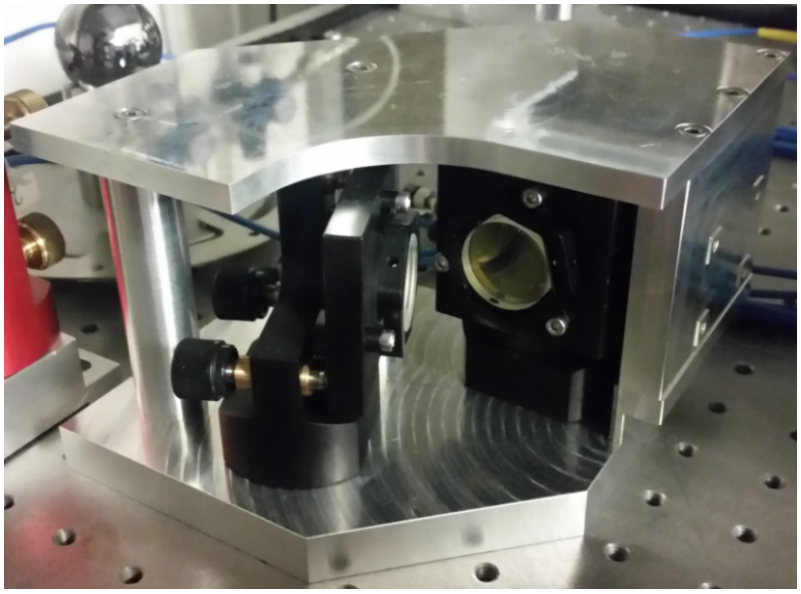

Figure 4.8: New set of adjustable mirrors mounted in an aluminum structure.

Lastly when the laser beam hits the reference mirror surface, because the latter is ring shaped, the reflected laser beam spreads unlike when it hits flat reference mirrors. So a plano convex cylindrical lenses made of BK7 with a focal length of ≈ 80 mm are used in order to minimize such spread effects on the reflected laser beam.

Chapter 5

Software Development and integration of second rotational stage

In this chapter all the software improvements and added hardware which allow a complete topography mapping are explained. First the implementation of fast angle read-out using a Printable circuit board (PCB) to connect encoders in the FPGA are explained, then how the host program sampling speed was increased, how the frequency mixer low pass filter was designed to address the increased sampling speed by the host and then the added hardware such as step motor driver are discussed.

5.1 Encoder integration

Two possible methods of integrating the encoder's signals from both rotational stages into the FPGA are, direct connection between encoders and FPGA or using an intermediary device. In order to integrate the encoder signals in the FPGA, both encoder signals must be analyzed in terms of how they are transmitted and their transmission speed.

Both encoders transmit information using two complementary signals, called differential signaling which is a technique used for noise elimination, but have different transmission speeds, 10 MHz and 2 MHz for first and second rotation stages respectively.

Since the FPGA has a maximum clock speed of 40 MHz, and therefore is faster than the encoder's signal transmission speeds, it isn't a limiting factor. However since the encoders transmit differential signals, direct connection between them and the FPGA becomes complicated to work with, because the FPGA would have to be programmed also to read differential signals when there are already integrated circuits in the market that do this exact work at very fast data transmissions. Therefore the chosen method was using differential signal receiver integrated circuits (ICs) to design a PCB which can read

encoder differential signals at fast data transmission and connect to the FPGA only digital outputs of this device following flow chart's 5.1 logic.

After the digital output signals from the PCB are read by the FPGA, encoder VIs track the rotation position of the different rotational stages. For each full rotation of the first rotational stage, the FPGA orders the stepper motor from the second rotational stage to rotate via the step motor driver.

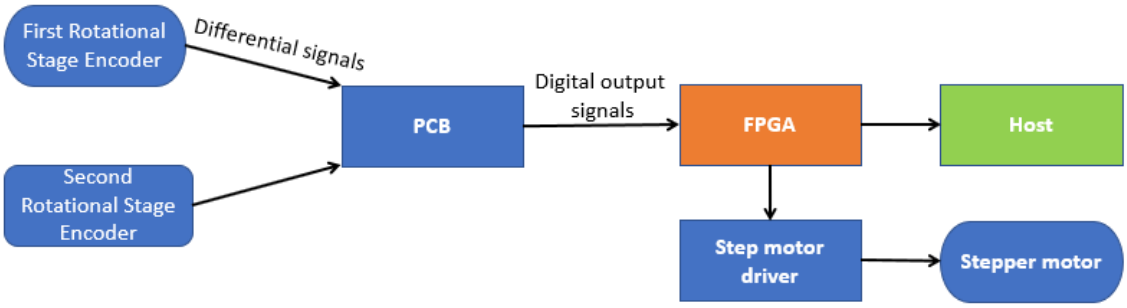

Figure 5.1: Schematic of the encoder's signal integration into FPGA.

5.1.1 PCB design

In order to design the PCB, working conditions and connector's pin-outs of the encoders have to be taken into consideration.

The first rotational stage encoder has an independent power supply, requiring no inputs besides ground to keep the same reference as the other components.

The second rotational stage encoder, on the other hand, does not have an independent power supply, therefore needs as input not only ground but also the operating voltage value, which in this case is +5 V. For this an external power supply is not needed since the FPGA has +5 V output, so the FPGA is responsible to supply the ground and VCC to the PCB and encoders.

The purpose of the designed PCB, in figure 5.2, is to convert the differential signals from the encoders into digital outputs with low and high logic levels suitable for the FPGA. Thus means the outputs of the used ICs have to be TTL with a maximum 0.8 V for low logic level and minimum 2.0 V for high logic level.

Another IC requirement to be considered, besides converting the differential signals at high data transmissions, is the operating voltage supply value. Since the second rotational stage encoder needs a +5 V supply to function, having an IC with the same working supply would mean that only one power supply for the PCB is needed, so only the FPGA +5 V output is necessary.

The differential signal receiver with +5 V supply chosen was the MAX3095CSE+. This IC is low-power quad RS-422 receivers.

The pin-outs of both encoders and for the PCB are shown in appendix A.

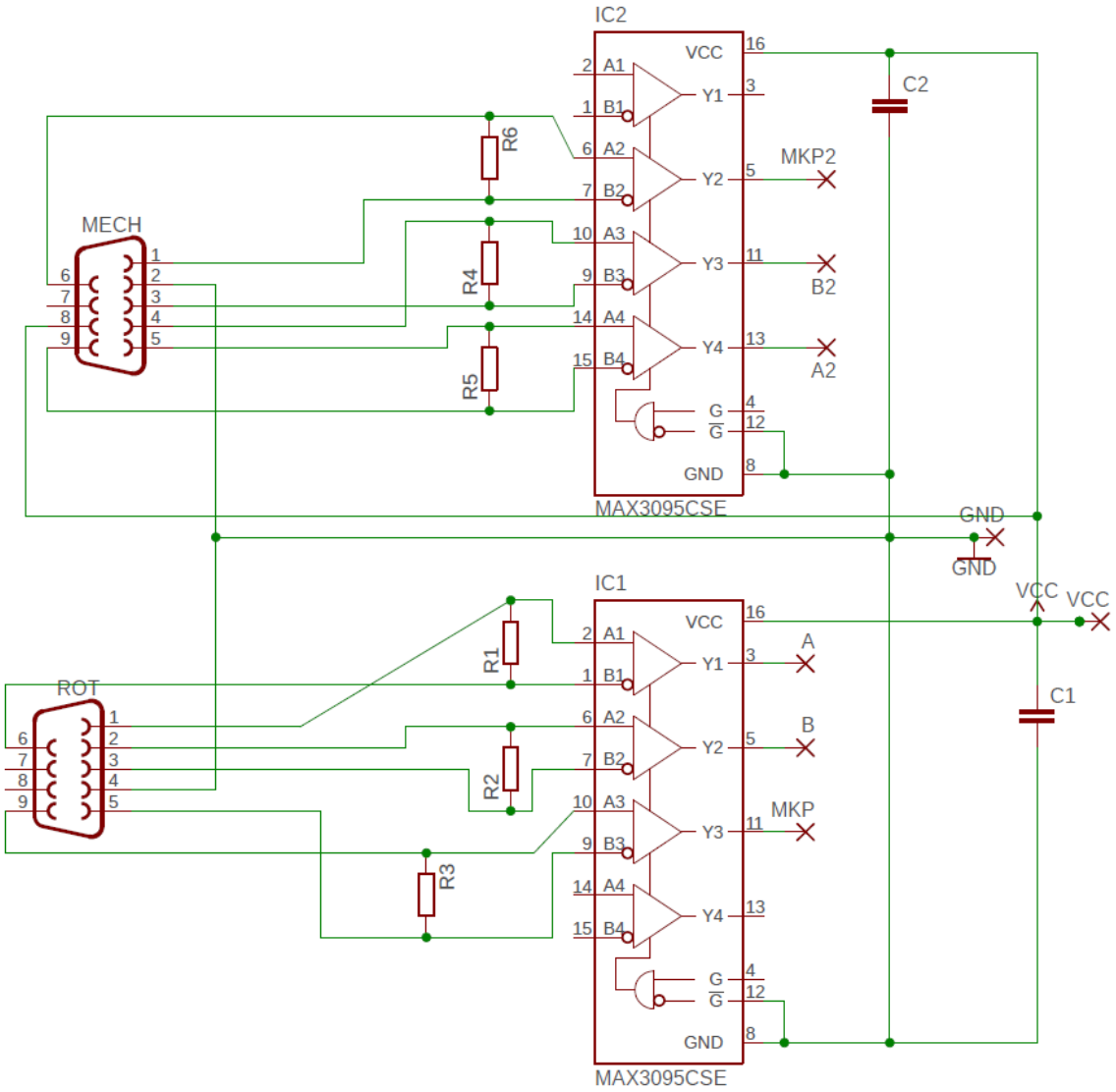

Figure 5.2: PCB electronic schematic for the encoders integration in FPGA, where ROT stands for first rotational encoder and MECH for second rotational encoder. The A, B, MKP, MKP2, A2, B2, VCC and GND are connected to FPGA digital I/O.

5.1.2 Code integration in FPGA

Figure 5.3 shows how the encoder's signals are input in the FPGA. It is in this VI where the encoder signals A and B are translated to integer rotation position. If A leads B and such case is verified then the VI will sum to its current position +1. The position is saved from one cycle to the next. The reset input serves to restart the encoder counting. The connectors with signals A and B correspond to the FPGA pins where the PCB feeds its respective outputs.

In figures 5.4 and 5.5 the code for integrating the encoders in FPGA is shown. In these figures the control process of the encoders takes part. The *Connector*0/*DIO*2 reads the MKP input signal from the first rotational stage encoder, hence when this signal is read by the FPGA the incremental encoder position for the same encoder is reset. This signal

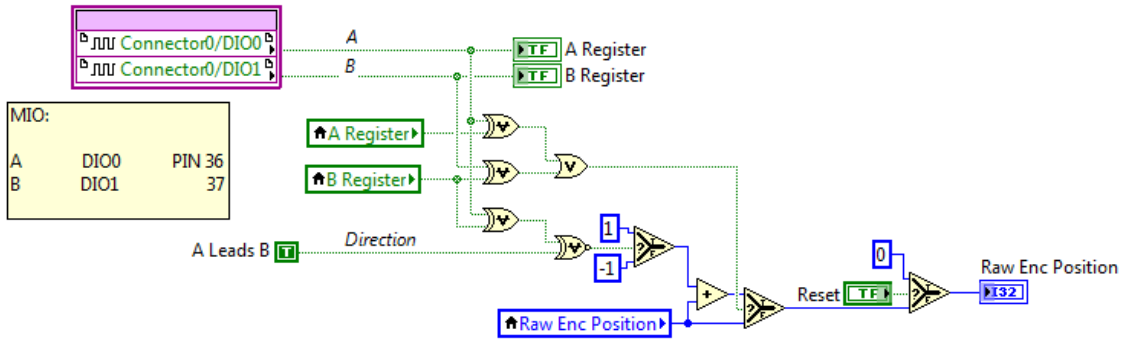

Figure 5.3: Block diagram of the encoder VIs with the connectors DIO detecting the signals A and B. Raw Enc. Position stands for the integer position of the encoder.

controls when a new circumference will be measured by signaling the step motor driver to activate the stepper motor to make a step.

Since the FPGA is a fast processing hardware, a timer had to be added when signaling the step motor driver, as due to its specifications any signal faster than 2 MHz is low-pass filtered. So the timer is used to make sure the signal lasts long enough for it to be detected by the controller.

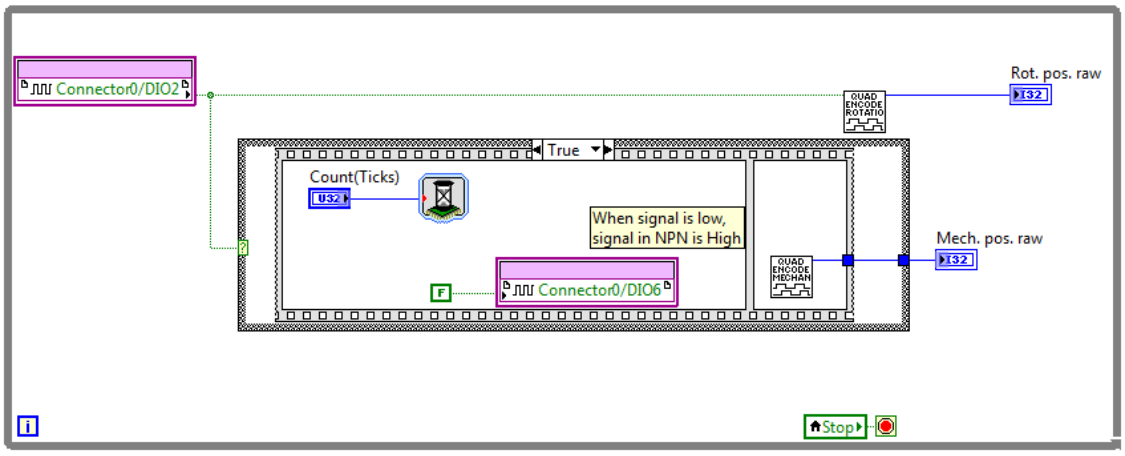

Figure 5.4: FPGA block diagram with the implementation of fast angle read-out encoders. Rot.pos.raw stands for the integer position of the first rotational stage, Mech.pos.raw stands for the integer position of the second rotational stage

As a first hardware obstacle to the correct working condition of the code, was the step motor driver having the COM+ and STEP inputs optically isolated as shown in figure 5.6.

Since the minimum voltage value in the COM+ is +5 V, the STEP input needs to have a digital signal with a logical high larger than 4.3 V and a logical low smaller than 4.3 V. The FPGA logical high is $\approx$ 3.3 V, therefore the output signal is not enough. To solve this issue a lever shifter using an NPN transistor was designed as to whenever the logical value of the first rotational stage MKP changes, the lever shifter changes the 3.3 V high logic level to 5 V logic level, therefore a rising edge of logical level high is detected by the step motor driver thus ordering the stepper motor to step.

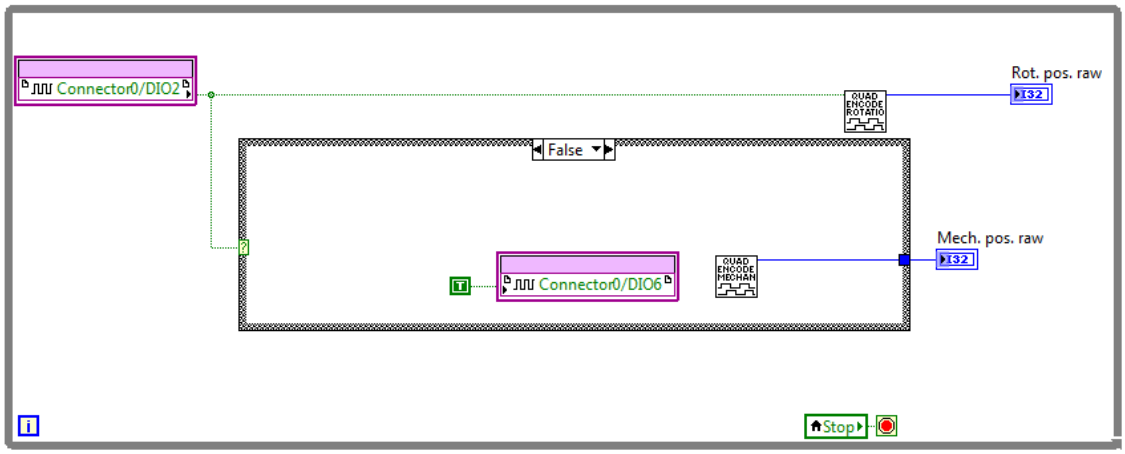

Figure 5.5: FPGA block diagram with the implementation of fast angle read-out encoders.

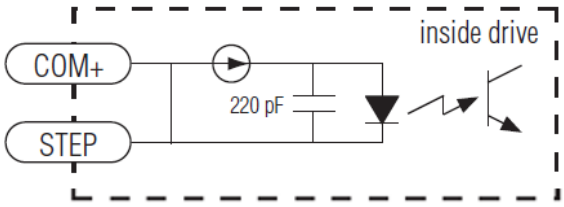

Figure 5.6: Schematic of the microstep controller inputs COM+ and STEP, optically isolated, necessary to make the motor rotate.

5.1.3 Stepper motor and step motor driver

The stepper motor is composed internally of a set of coils which allows the motor to rotate its shaft by increments, or steps, of a specific length. The NEMA8 motor used has a step motion of 1.8° with an error of 5 % and a holding torque of 12 – 15 mNm. Stepper motors bigger than NEMA8 are not considered for this application due to higher torque values and their size does not fit the application.

A step motor driver is a device used to drive the motor with a step length smaller than the motor was designed for, with a method called micro stepping. The STR2 step motor driver is capable of several different step size options per revolution for smoother motion of the motor shaft.

The step motion of the stepper motor induces different angles in the carried, driver and SPM due to radius ratios. The angular step of each component is:

$$\begin{cases} \delta\theta_c = \frac{2\pi}{div} \\ \delta\theta_{SPM} = \frac{2\pi}{div}\frac{r_c}{d_c} \\ \delta\theta_d = \frac{2\pi}{div}\frac{r_c}{d_c}\frac{r_{SPM}}{r_d} \end{cases} \tag{5.1}$$

resulting in

$$\begin{cases} \delta\theta_c = \frac{2\pi}{div} \\ \delta\theta_{SPM} = 0.5 \cdot \frac{2\pi}{div} \\ \delta\theta_d = 0.56 \cdot \frac{2\pi}{div} \end{cases} \tag{5.2}$$

with div being the number or micro steps defined by the step motor driver.

5.2 Increasing the sampling frequency

The sampling frequency is the speed at which the host program reads or samples data from the FPGA.

The host program runs entirely in one single CPU core, thus the speed processing is heavily compromised by the encumbrance of data. The remaining CPU cores do not have any load, therefore the host program is not using the entire process power available in the workstation. To increase the host program sampling frequency, its tasks will be divided to the remaining CPU cores.

In LabVIEW exists two ways to achieve this type of parallel tasking: pipelining and data parallelism.

Pipelining works as an assembly line, where each stage of the code focuses on one single CPU passing its results to the next stage until the final stage. This method consists in breaking down the algorithm into steps running on separate cores.

Unlike pipelining, data parallelism consists in dividing data that can be processed independently through the different available cores. Therefore code that can run independently such as calculations, graphics and other mathematical operations which only need an input, are processed by other cores.

After analyzing the host program, data parallelism was the chosen concept for parallel tasking. Not only is of easier implementation than pipelining, but also isn't susceptible to out of synchronization issues. This method is used to remove from the host program the graphics and mathematical calculations, leaving only the essentials, so that the host program works only as an interface for the FPGA to save the data collected from the experimental setup.

Within data parallelism there are three different ways which parallel tasking can be implemented

- Global variables
- Asynchronous static VIs
- Asynchronous dynamic VIs

Global variables are of easy implementation but when working at fast sampling regimes, the entire workstation memory can become a limiting factor due to memory

allocation issues of the global variable. These are also slower than local variables being prone to mismatches between the speed at which global variables can update and the speed at which they are read by the other VIs.

Unlike global variables, asynchronous static and dynamic VIs are of harder implementation, but offer total independence between VIs and CPU cores. These VIs run independently of the main VI and only run when an input is given, which can be done with a local variable of the main VI. Asynchronous dynamic VIs work like the static ones, but these can also send back information to the main VI, the static ones don't. This feature is not necessary so the asynchonous static VIs will be used to increase host performance.

5.2.1 Asynchronous static VI

In figure 5.7 and appendix B the developed code of the asynchronous static VIs are shown. This code is in the host program blockdiagram and transports the local variables from the host directly to the other VI running in a separate CPU core, thus allowing an increase speed interaction between FPGA and host program.

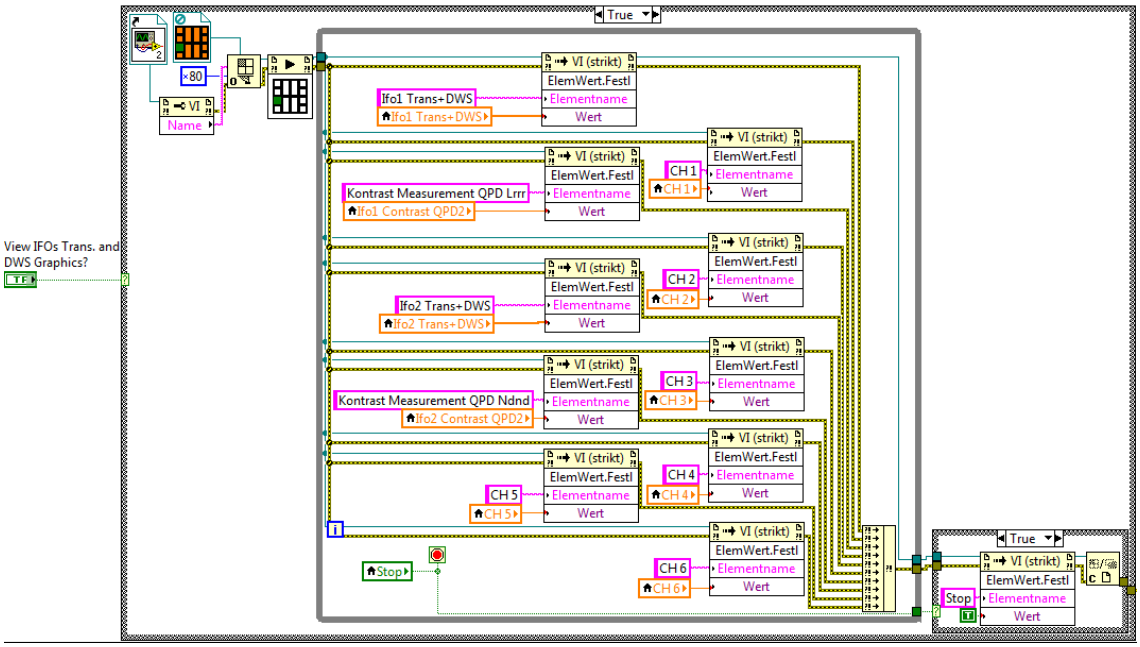

Figure 5.7: LabVIEW blockdiagram code developed for increasing host program sampling rate by using asynchronous VI for parallel processing with multi-threading.

With data parallelism is possible to increase the sampling frequency from 20 Hz to a maximum of 2 kHz. Above this new limit, the computer RAM gets full thus the code can not execute properly.

Since the surface measurement resolution is 8.75 mrad, it is possible to distinctly measure $\frac{2\pi}{0.00875} \approx 718$ points in each circumference but also measure 718 different circumferences, therefore a total of 515 524 points can be measured. Assuming that the first rotational stage has no restrictions in rotation speed, that the second rotational stage

works perfectly without slipping, that the step motor driver can supply any desired number of micro steps, which in this case is $div = 0.5 \cdot \frac{2\pi}{0.00875} = 359$ steps per revolution, and with a sampling frequency of 2 kHz, almost a thousand points per second can be measured, respecting the Nyquist rate. The Nyquist rate is the sampling frequency required to sample a signal correctly, to avoiding aliasing and has to be higher than twice the sampled signal frequency .

In these ideal conditions mentioned, the minimum time needed to measure a complete 2D surface map of the SPM is ≈ 516 seconds with the first rotational stage rotating at $\frac{360° \cdot 1000}{718} \approx 501°/sec$.

5.3 Implementation of faster phase lock loops

5.3.1 Low pass filter design

Filtering can cause latency problems, so to prevent this the low pass filter has to be designed to be as fast as possible, in this particular case at the speed of a single cycle loop of the FPGA. Do to so an IIR Butterworth lowpass filter was implemented using Very High Speed Integrated Circuit Hardware Description Language (VHDL) and several first order filters working in cascade. The first order Butterworth filter is calculated as

$$y_k = (1-a) \cdot y_{k-1} + a \cdot x_k \tag{5.3}$$

with the transfer function in the z-domain as

$$H_a(z) = \frac{a \cdot z}{z-(1-a)} \tag{5.4}$$

therefore the transfer function of an n^{th} order filter is

$$H(z) = H_a(z)^n \tag{5.5}$$

and cut-off frequency can be calculated as

$$\|H(z)\|^2 = \frac{1}{2} \tag{5.6}$$

with

$$z = e^{j2\pi f_c T_s} \tag{5.7}$$

where T_s and f_c are sampling and cut-off frequency respectively. The existent relation between the cut-off frequency and filter order is the parameter a, described in figure 5.8.

The value of parameter a and the filter order is chosen so that:

- the cut-off frequency is high enough compared to the points per second measured from the SPM surface

- the cut-off frequency is low enough so that the heterodyne frequency is sufficiently suppressed after the filter
- the cut-off frequency is close to the host sampling frequency
- the filter order is low to save FPGA resources

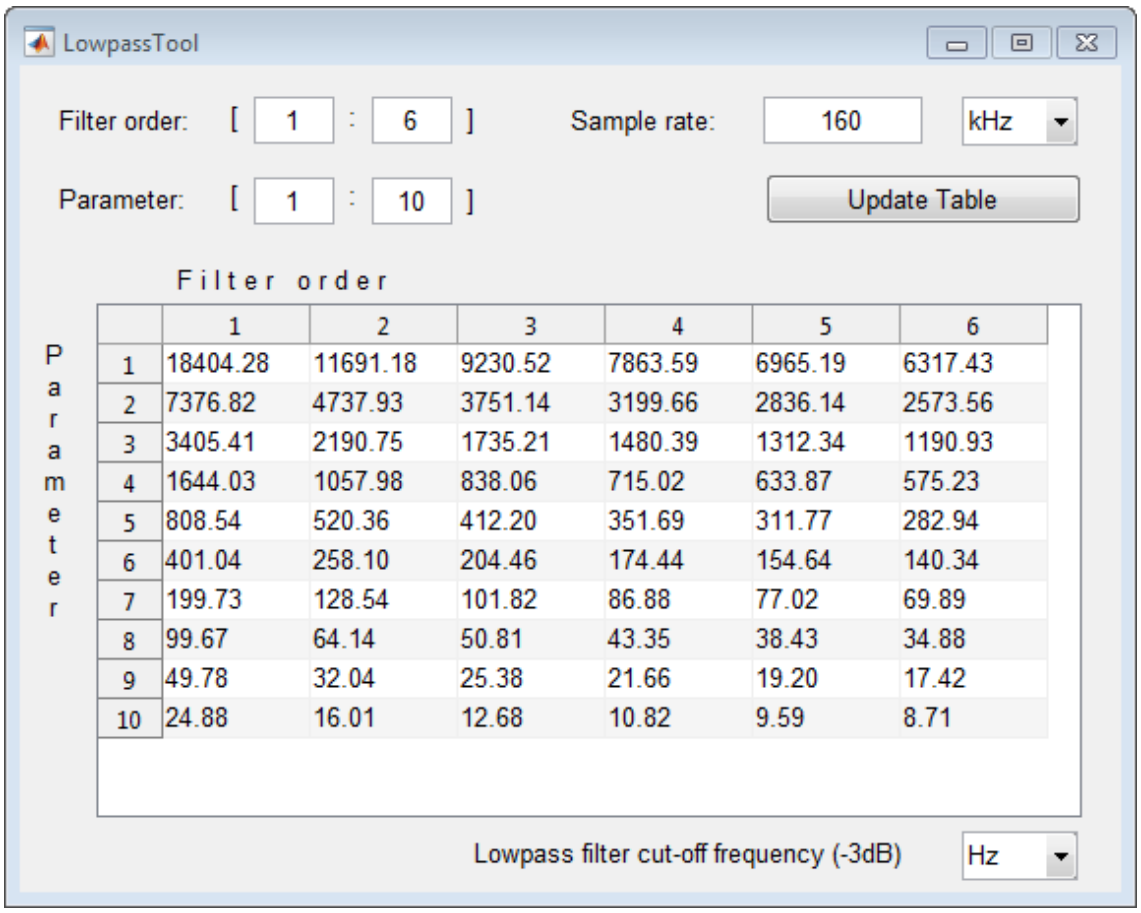

Parameter \ Filter order	1	2	3	4	5	6
1	18404.28	11691.18	9230.52	7863.59	6965.19	6317.43
2	7376.82	4737.93	3751.14	3199.66	2836.14	2573.56
3	3405.41	2190.75	1735.21	1480.39	1312.34	1190.93
4	1644.03	1057.98	838.06	715.02	633.87	575.23
5	808.54	520.36	412.20	351.69	311.77	282.94
6	401.04	258.10	204.46	174.44	154.64	140.34
7	199.73	128.54	101.82	86.88	77.02	69.89
8	99.67	64.14	50.81	43.35	38.43	34.88
9	49.78	32.04	25.38	21.66	19.20	17.42
10	24.88	16.01	12.68	10.82	9.59	8.71

Figure 5.8: Table showing the relation between cut-off frequency, filter order and parameter a for low pass filter design at FPGA sampling rate of 160 kHz.

Not all the combinations of parameter a and filter order shown in figure 5.8 can be used, due to the reasons mentioned above. Combinations with a cut-off frequency above the heterodyne frequency and below the points per second measured from the SPM surface are disregarded.

According to equation 3.3, the 10 kHz heterodyne frequency component has the same amplitude as the measured signal, thus it is recommended at least -60 dB suppression of the heterodyne frequency component, figure 5.9. Therefore any low pass filter which does not satisfy this suppression criteria, will also be disregarded.

Low pass filter design and VHDL script can be consulted in appendix B.

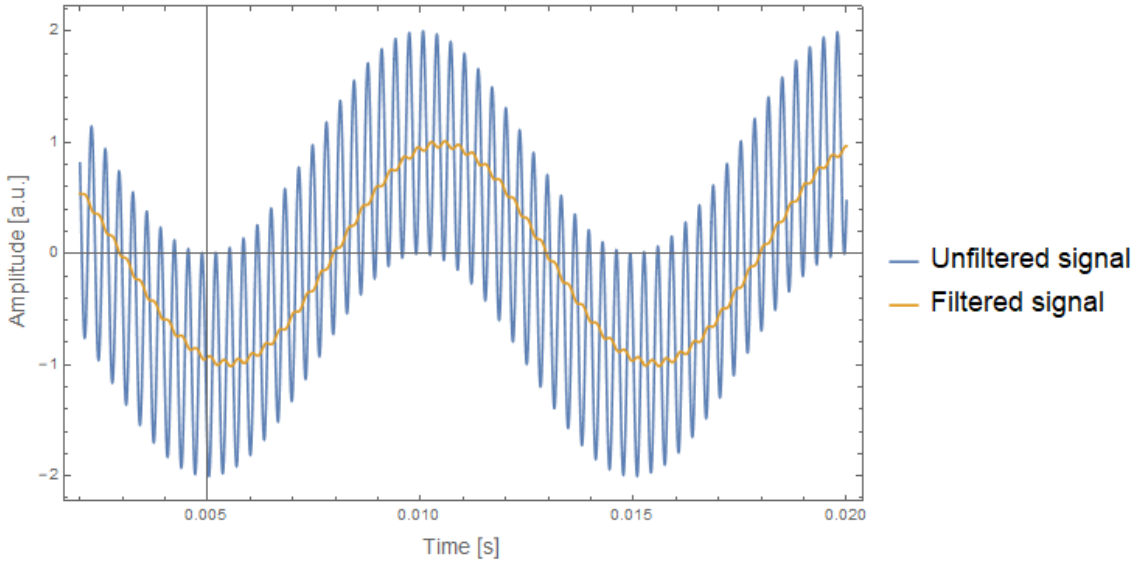

Figure 5.9: Plot of unfiltered and filtered equation 3.3 with -60 dB suppression of the heterodyne frequency component and a measurement signal of 100 Hz. With a.u. as amplitude units.

Chapter 6

Results

In this chapter the results for performance measurement of the interferometers with the new low pass filter, sampling frequency and implementation of the encoder signals for surface mapping are shown. These results aim to prove the successful implementation of the changes proposed in this work. Before presenting the obtained results, the measurement conditions will be described.

6.1 Measurement conditions

The setup was unused for two years and thus requiring optical and electronic bench testing before software improvements could be tested. Due to time constrains, optimizing both optical and electronic benches for optimal working condition was overlooked aiming only for working condition.

To test the software improvements, a reference mirror is held static on the interferometers laser output, reflecting both measurement and reference beams back to the QPDs.

During vacuum pumping, not only a vacuum leak was detected in the vacuum chamber which compromised the measurements, but also the vacuum sensor used was not properly calibrated, so the actual low pressure value at which the measurement started can only be estimated to be between 50 and 60 mbar.

The results obtained were sampled from the host program at 500 Hz, with six first order low pass filters in cascade with a cut-off frequency of 575.23 Hz, figure 6.1, and over sixty five hours of continuous measurement. Around the fourteenth hour of continuous measurement, the laser beams got out of phase therefore any data measured after this is disregarded since it no longer represents reality, but can be consulted in appendix C.

Due to hardware limitations of the first rotational stage with a maximum rotation speed of 30°/*sec*, to the measurement diameter of the laser beam on the SPM surface

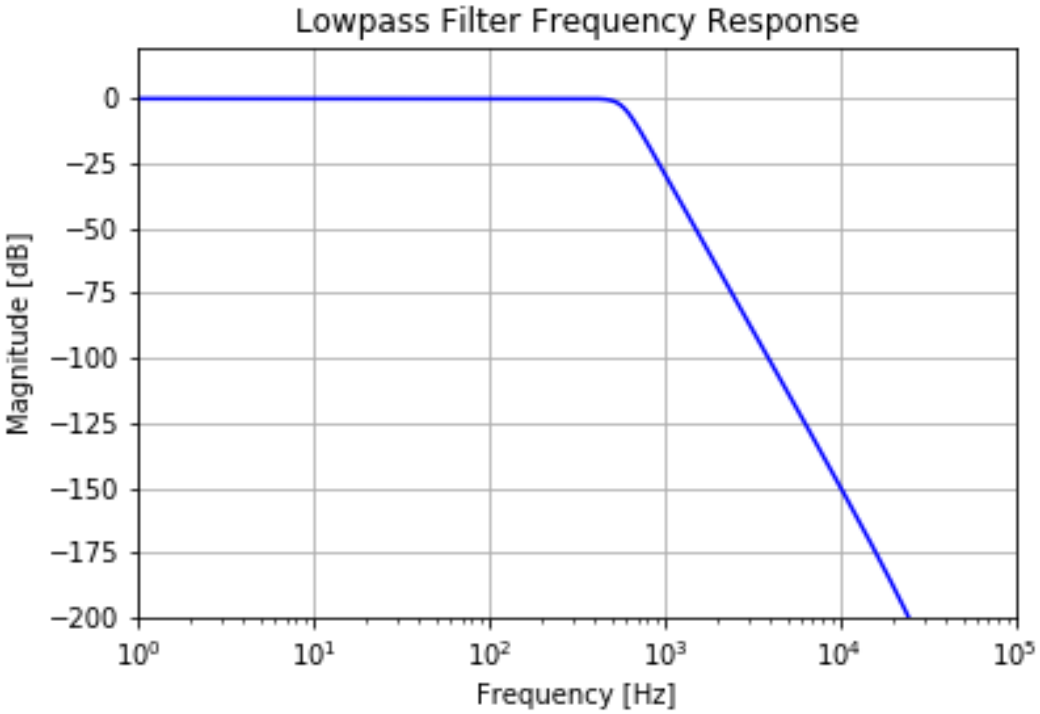

Figure 6.1: Magnitude response of the low pass filter. Cut-off frequency $f = 575.23$ Hz, sixth order.

and the diameter of the SPM, the host sampling frequency was set to 500 Hz. Since the maximum measurement points which can be distinctly detected in a single circumference measurement of the SPM is ≈ 718, only 60 points are measured each second at the designated speed of $30°/sec$. Therefore there is no need to strain the setup by testing it at 2 kHz sampling frequency when 500 Hz is sufficient to sample 60 points per second. Also the step motor driver has specific micro stepping values which do not coincide with the assumed value in section 5.2 and therefore the closest lower value of 200 micro steps was chosen.

In order to test the success of the implementation of the new host sampling frequency, low pass filter design and fast angle encoder read-out, several measurements were done:

- performance measurement, to test for thermal and mechanical noise influence
- relative displacement measurement by each QPD of each interferometer
- total displacement measured by each interferometer, $QPD_{MES} - QPD_{REF}$
- encoders coordinates plotting for surface mapping

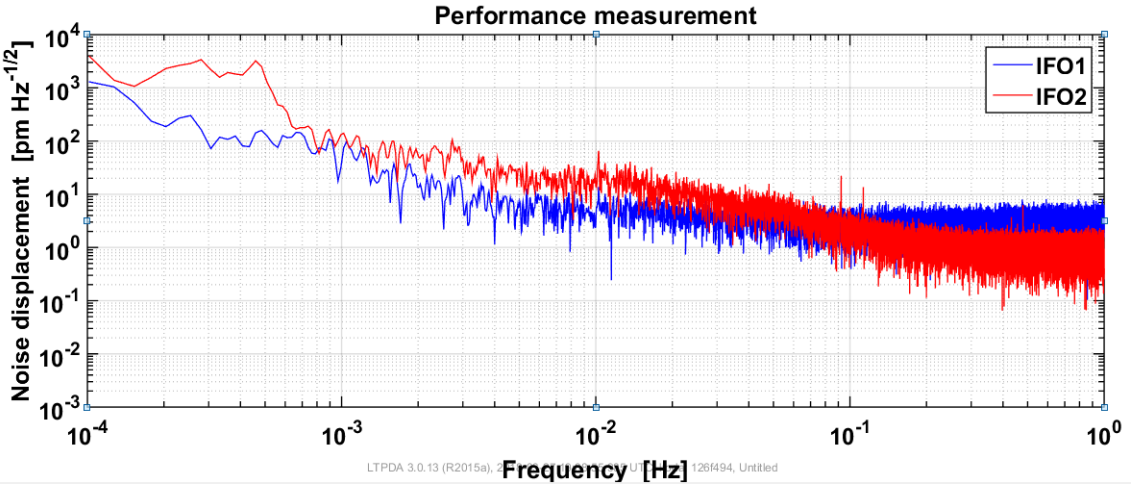

Figure 6.2: Performance of the measurement setup with reference mirror outside of each interferometer. Measured displacement noise of both interferometers is depicted as a function of frequency.

6.2 Performance measurement

The performance measurement plotted in figure 6.2 shows that thermal and mechanical deformations affect the measurement at a picometer range from 10^0 Hz to 10^{-3} Hz, while at lower frequencies effects are in the order of few nanometers. Therefore thermal and mechanical noise effects can be neglected, since its lower than the error parameters in table 3.2.

This performance measurement was done using the LTPDA toolbox which is designed for data analysis from the LISA Technology Package (part of the LISA Pathfinder Mission). With this toolbox, Power spectrum density (PSD) was used to stipulate the noise displacement caused by thermal and mechanical deformations for low frequencies. This function has an extensive list of parameters to better analyze the data. The used parameters are shown in the code in figure B.7 in appendix B.

6.3 Interferometers displacement

Figures 6.3, 6.4, 6.5 and 6.6 show the relative displacement measured for each QPD of each interferometer and the translation of each interferometer, $|QPD_{MES} - QPD_{REF}|$, as function of time, since the interferometers do not measure absolute displacements.

Displacement is measured in μrad. In order to plot the measurement data at nanometer scale, the phase measurement of the QPD is equal to the average signal measured by all four quadrants, α. Therefore displacement l can be calculated as

$$l = \frac{\lambda}{4\pi} \cdot 10^{-6} \cdot 10^{9} \cdot \alpha \tag{6.1}$$

since $\lambda = 1064 \cdot 10^{-9}$ m results in

$$l = \frac{1064}{4\pi} \cdot 10^{-6} \cdot \alpha \text{ [nm]}. \tag{6.2}$$

The laser alignment and working condition of the QPDs is shown in figure B.6 in appendix B. Each QPD quadrant detects the system alignment by measuring the superposed part of the laser beams compared to the full light intensity detected, black and blue bar respectively. As can be seen in the same figure, the alignment of the system is not optimal due to the overall intensity difference detected by each quadrant of each QPD, showing a not optimal alignment of the QPDs with the laser beams. The difference of measured superposed laser signal from the total detected in each quadrant, shows that the alignment of the lasers themselves have to be adjusted. Furthermore, in QPD_2 or QPD_{MES} from IFO_1, one of the quadrant detectors stopped working, which slightly impacts the measurement done by the QPD.

The measurement drift shown in figures 6.4 for QPD_{MES}, 6.5 and 6.6 is explained by the vacuum leak compromising the measurements. The gradual increase in pressure inside the vacuum chamber, figure 6.7, changes the refractive index thus leading to a change in optical pathlength. Taking into consideration the working condition of the vacuum sensor, the initial pressure considered is 60 mbar and a final pressure of 75.5 mbar after fourteen hours of measurement, the total refractive index variation is calculated using the script B.10 in appendix B, resulting in

$$\Delta n = n(75.5) - n(60) = 4.2 \cdot 10^{-6} \tag{6.3}$$

Although the measurements conditions were not optimal, the total displacement measured by both interferometers, $QPD_{MES} - QPD_{REF}$, is in nanometer order, which is to be expected.

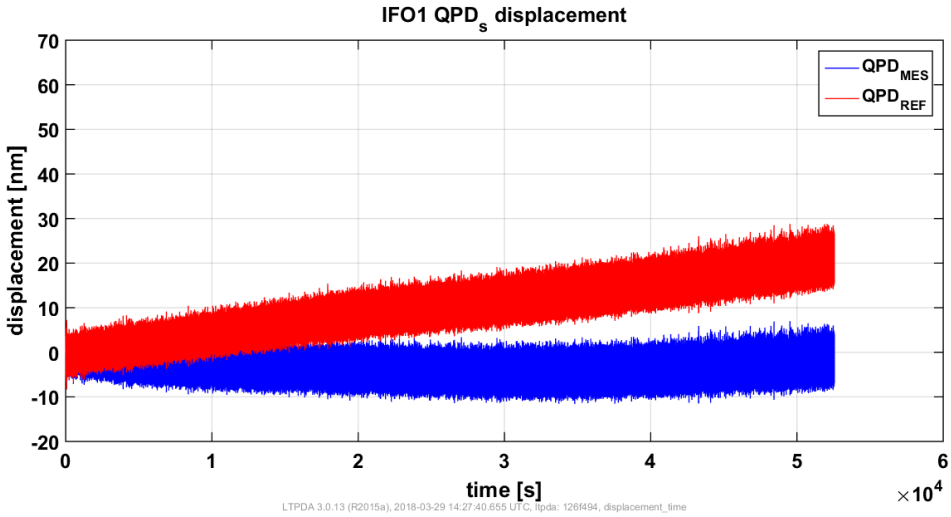

Figure 6.3: Relative displacement of each QPD from IFO1.

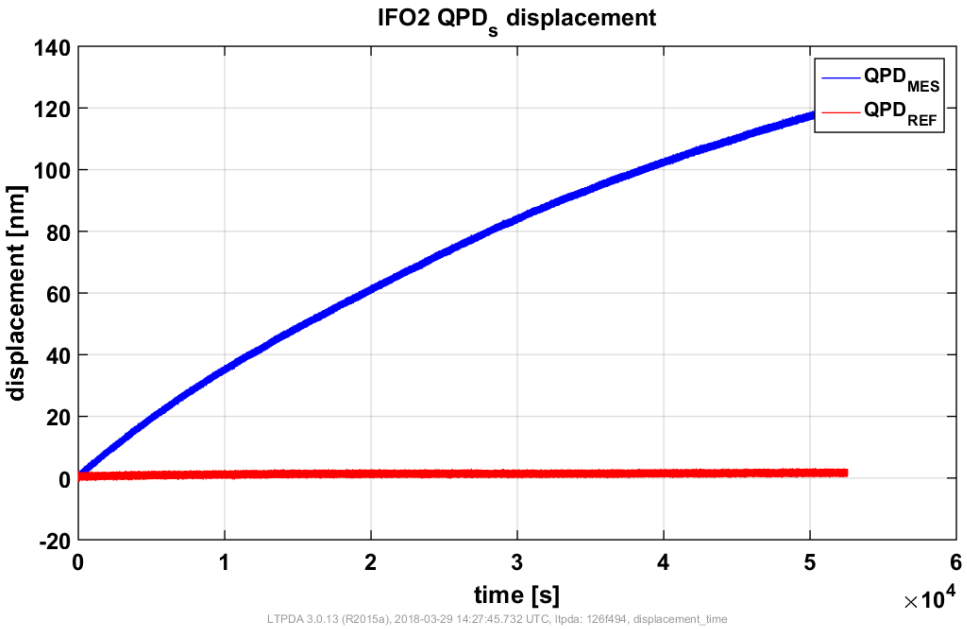

Figure 6.4: Relative displacement of each QPD from IFO2.

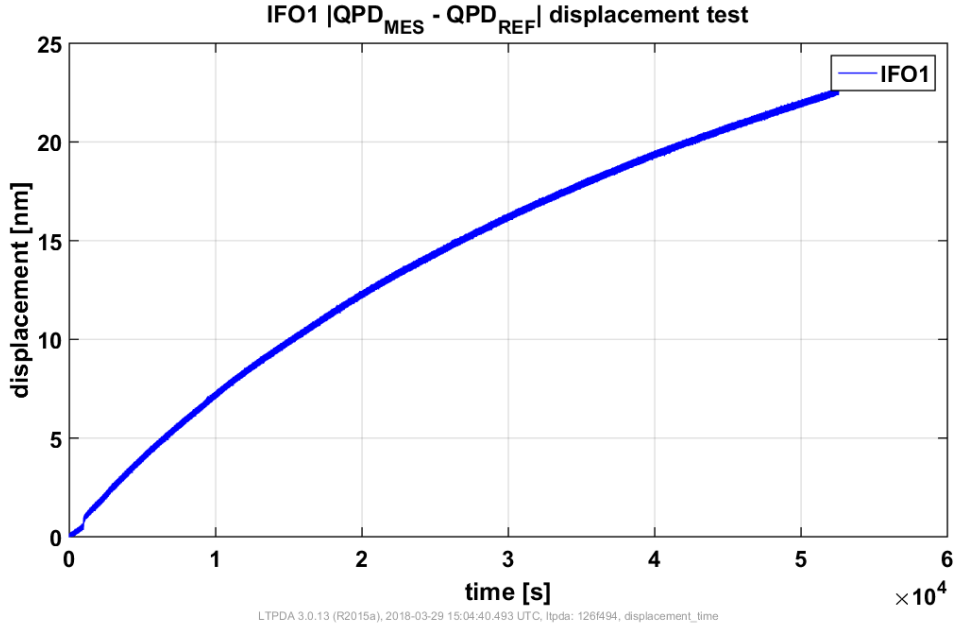

Figure 6.5: Difference displacement between both QPDs from IFO1.

6.4 Encoder implementation for surface mapping

The SPM position is indirectly measured by the encoder in the driver. The angular position of the encoder coincides with the drivers, but not with the SPM. To calculate the SPM angular position with the encoder information, the ratio between SPM and driver radius is used. Since each incremental step of the encoder is ≈ 0.314 mrad, the same incremental

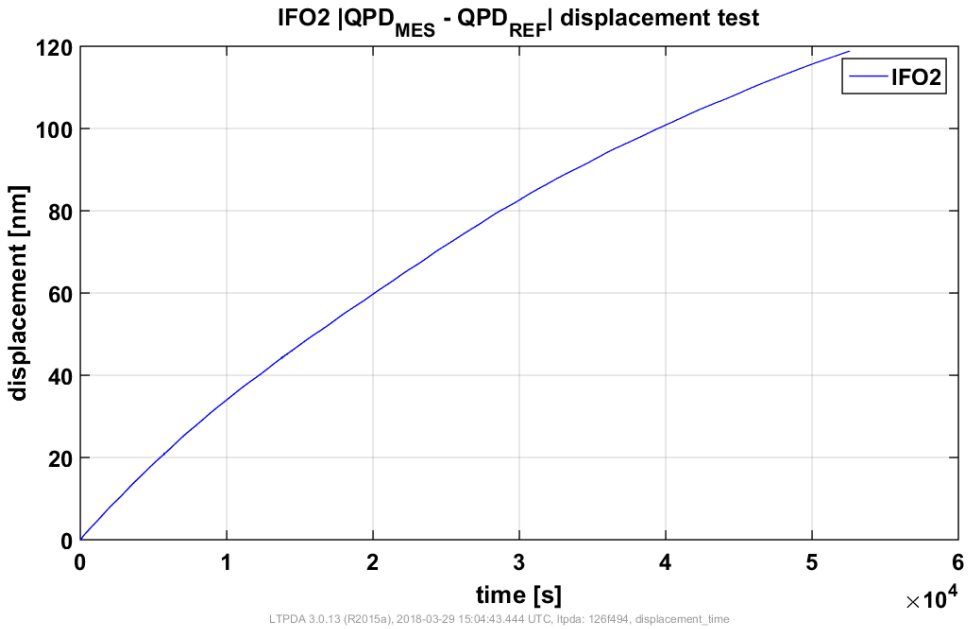

Figure 6.6: Difference displacement between both QPDs from IFO2.

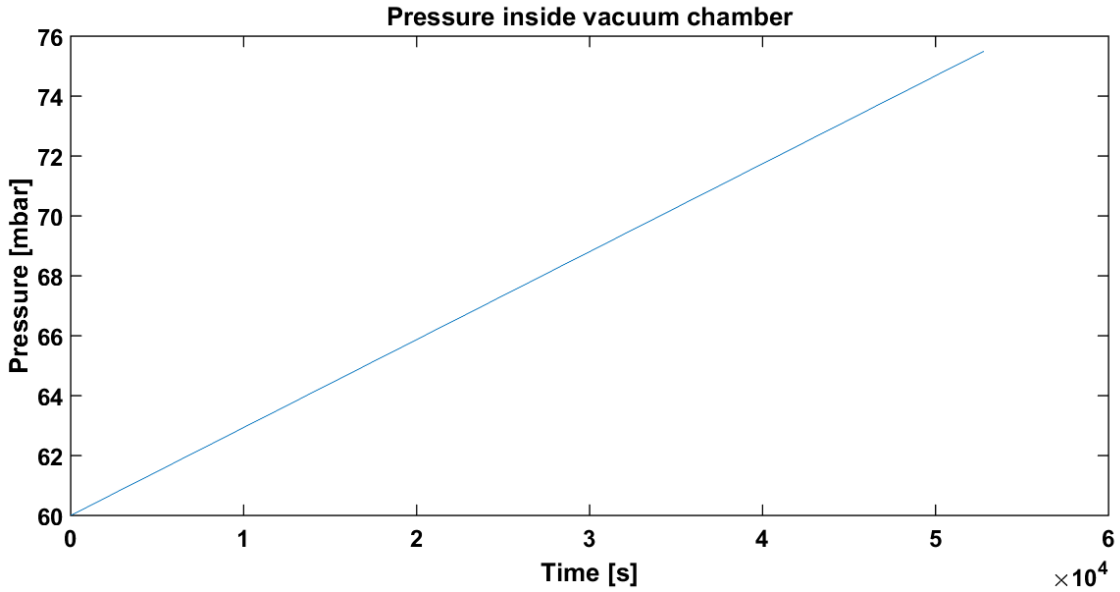

Figure 6.7: Pressure variation inside the vacuum chamber.

step for the SPM is

$$\delta\theta_{SPM} = 0.314 \cdot \frac{r_d}{r_{SPM}} = 0.283 \text{ mrad} \tag{6.4}$$

The following figures 6.8 and 6.9 show the implementation of the encoder position reading, to simulate the surface topography mapping of the SPM with the step driver controller at the 200 steps per revolution option. Therefore the expected angular distance between each circumference is ≈ 0.015 rad.

An initial worry with the implementation of the second rotational mechanism was the time interval it would take the SPM to stabilize its position upon a step. But due to the density of points at the poles visible in figure 6.8, this slipping interval can be ignored due to the amount of averaging by point done at the poles.

However after the SPM stabilizes its position, the total slipping effect causes a non-uniform distance between different measured circumferences, as can be seen in the side view plot 6.9. This slipping effect can be explained by the NEMA8 motor used having a high holding torque which compromises the operation smoothness. The motor quality itself is not ideal for this application due existence of turning points in which the motor needs to exert a higher torque than others. Temperature changes inside the motor can also be a possible cause for the slipping, since after a couple of steps with a homogeneous rotation in the first quadrant of the plot, the motor starts heating compromising the step increments performance. Morphological characteristics of the motor are also an issue like a not completely straight shaft and alignment to the carried axis.

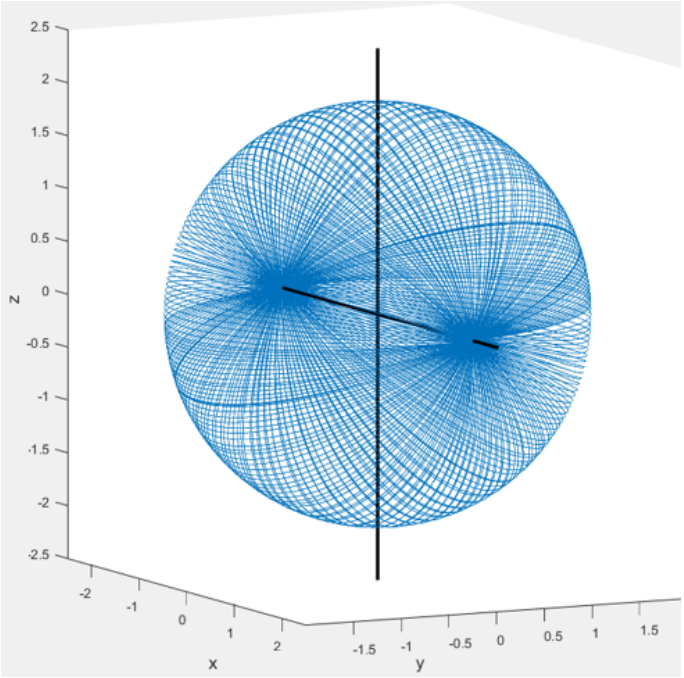

Figure 6.8: Plot of the measurement circumference with only the encoder position information at 500 Hz.

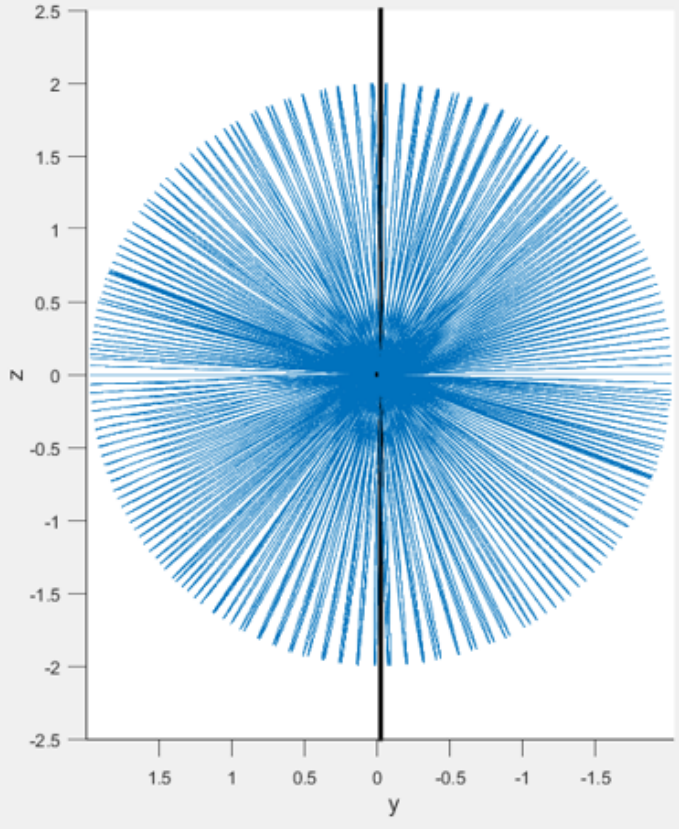

Figure 6.9: Side view of the measurement to check for slipping.

Chapter 7

Conclusion and Outlook

In this work a novel inertial sensor concept for optical readout of a spherical proof mass for space missions such as LISA and Big Bang Observer was studied. This novel concept requires surface topographical mapping of the spherical proof mass for correct center of mass determination. Therefore the aim of this thesis was to supply the tools necessary for a complete surface topographical map.

An experimental setup capable of 2D surface measurement was thus constructed by adding a second degree of freedom to the spherical proof mass in a setup for measuring circumferences, fast encoder readout for surface topographical measurement positioning and improving overall performance of the used software by using data parallelism.

The results shown in this work, although not optimal for the performance expected of an interferometer, show successful implementation of the proposed software and hardware changes. These changes allow for future complete surface topography mapping of the SPM at faster measurement speeds, which make the whole measurement less susceptible to thermal and mechanical deformations, and more practical setup to work with.

Currently the improved experimental setup works mostly limited by hardware and not software, such as the first rotational stage maximum rotation speed, the measurement diameter of the laser on the SPM surface and stepper motor quality.

In this work was demonstrated absence of massive slipping phenomena. Upon a stepper motor step, there is such a high density of measurement points in the poles $\theta = 0°, 180°$ that the initial slipping interval, until the sphere position stabilizes, can be neglected. After the SPM stabilizes its position, there is however a small slipping in the measurements, which indicates that adjustments have to be done. Changing the current stepper motor for one with less holding torque and better quality, but still small enough for this application, is a necessary adjustment to improve the smoothness of the operation, leading to more homogeneous SPM motion.

The next step for this project is to finalize the setup of the periscopes, second rotational stage and new reference mirror configuration inside the vacuum chamber. The ring shaped reference mirror geometry will be tested, thus modifying the mathematical model used for the error suppression in order to take into account the new implemented topography which will correct the s_x influence in the measurements.

After these changes are complete, the setup will be capable of measuring a complete surface topographical map of the SPM. By combining surface plotting and measurement displacement calculation scripts developed in MATLAB, it is possible to plot the measured displacement at the surface point of measurement.

To further improve the accuracy of the center of mass determination, after obtaining the SPM surface map, the other direction synchronous error movements, s_y and s_z, will be disregarded by using the DWS concept. This concept allows tilt measurements by the QPDs, thus improving the center of mass position determination accuracy.

In the long run, inertial sensors based on spherical proof masses might surpass the requirements for LISA, allowing strain sensitivity measurements of $10^{-24}/\mathrm{Hz}^{-\frac{1}{2}}$ between frequencies of 0.1 and 1 Hz, which is the requirement for the Big Bang Observer to detect gravitational waves generated during the Big Bang [20].

Bibliography

[1] J. Centrella, J. G. Baker, B. J. Kelly, and J. R. van Meter. "Black-hole binaries, gravitational waves, and numerical relativity." *Reviews of Modern Physics* 82.4 (2010), pp. 3069–3119. ISSN: 00346861. DOI: 10.1103/RevModPhys.82.3069. arXiv: 1010.5260.

[2] B. P. Abbott et al. "Observation of gravitational waves from a binary black hole merger." *Physical Review Letters* 116.6 (2016). ISSN: 10797114. DOI: 10.1103/PhysRevLett.116.061102. arXiv: 1602.03837.

[3] J. H. Taylor. "Discovery of a Pulsar in a Binary System." *Annals of the New York Academy of Sciences* 262.1 (1975), pp. 490–492. ISSN: 17496632. DOI: 10.1111/j.1749-6632.1975.tb31467.x.

[4] M. Campanelli, C. O. Lousto, P. Marronetti, and Y. Zlochower. "Accurate evolutions of orbiting black-hole binaries without excision." *Physical Review Letters* 96.11 (2006), pp. 1–4. ISSN: 00319007. DOI: 10.1103/PhysRevLett.96.111101. URL: http://arxiv.org/abs/gr-qc/0511048.

[5] K. Danzmann. "Laser Interferometer Space Antenna - A proposal in response to the ESA call for L3 mission concepts." *European Space Agency Proposal* (2017), pp. 1–41. ISSN: 1054–660X. arXiv: 1702.00786.

[6] P. Amaro-Seoane et al. "eLISA: Astrophysics and cosmology in the millihertz regime" (2012). ISSN: 0031-9007. DOI: 10.1103/physrevlett.116.231101. arXiv: 1201.3621.

[7] D Gerardi, G Allen, J. W. Conklin, K.-x. Sun, D Debra, S Buchman, P Gath, W Fichter, and R. L. Byer. " Advanced drag-free concepts for future space-based interferometers : acceleration noise performance." *Review of Scientific Instruments* 011301.1 (2014). DOI: 10.1063/1.4862199.

[8] C. W. Everitt et al. "Gravity probe B: Final results of a space experiment to test general relativity." *Physical Review Letters* 106.22 (2011). ISSN: 00319007. DOI: 10.1103/PhysRevLett.106.221101. arXiv: 1105.3456.

[9] C. Brugger, B. Broll, E. Fitzsimons, U. Johann, W. Jonke, S. Lucarelli, S. Nikolov, M. Voert, D. Weise, and G. Witvoet. "An experiment to test in-field pointing for elisa." *International Conference on Space Optics* October (2014), pp. 1–16. URL: http://old.

esaconferencebureau.com/Custom/ICSO/2014/Papers/4.Friday10October/Session13BTELESCOPESAIT/2.66402{_}Brugger.pdf.

[10] J. W. Conklin. "Estimation of the mass center and dynamics of a spherical test mass for gravitational reference sensors." Doctoral dissertation. Stanford University, 2009.

[11] B. P. Abbott et al. "GW170817: Observation of Gravitational Waves from a Binary Neutron Star Inspiral." *Physical Review Letters* 119.16 (2017), pp. 30–33. ISSN: 10797114. DOI: 10.1103/PhysRevLett.119.161101. arXiv: 1710.05836.

[12] J. D. Ellis. *Field Guide to Displacement Measuring Interferometry*. Ed. by J. E. Greivenkamp. Vol. FG30. Bellingham, Washington: SPIE Field Guides, 2014. ISBN: 9780819497994.

[13] C. M. Wu and R. D. Deslattes. "Analytical modeling of the periodic nonlinearity in heterodyne interferometry." *Applied optics* 37.28 (1998), pp. 6696–6700. ISSN: 0003-6935. DOI: 10.1364/AO.37.006696.

[14] C. M. Wu, S. T. Lin, and J. Fu. "Heterodyne interferometer with two spatial-separated polarization beams for nanometrology." *Optical and Quantum Electronics* 34.12 (2002), pp. 1267–1276. ISSN: 03068919. DOI: 10.1023/A:1021355410552.

[15] S. R. Al-Araji, Z. M. Hussain, and M. A. Al-Qutayri. *Digital phase lock loops: Architectures and applications*. Springer US, 2006, pp. 1–191. ISBN: 0387328637. DOI: 10.1007/978-0-387-32864-5.

[16] X. Yu, S. R. Gillmer, and J. D. Ellis. "Beam geometry, alignment, and wavefront aberration effects on interferometric differential wavefront sensing." *Measurement Science and Technology* 26.12 (2015). ISSN: 13616501. DOI: 10.1088/0957-0233/26/12/125203.

[17] H. Kögel, D. Weise, A. Sell, E. Fitzsimons, D. Gerardi, U. Johann, and C. Braxmaier. "Interferometric surface mapping of a spherical proof mass for ultra precise inertial reference sensors." *Applied Optics* 55.34 (2016), p. 9830. ISSN: 0003-6935. DOI: 10.1364/AO.55.009830.

[18] D. V.a. N. Gesondheid. "Norms and Standards." *Government Gazette* 90.38486 (2005), pp. 7–11. URL: http://www.spherotech.net/img/downloads/en{_}din5401.pdf (visited on 01/18/2018).

[19] F. Mostallino. "Design of a Rotation Mechanism for Interferometric Surface Topography Measurements of a Sphere." Master's thesis. Università di Pisa, 2017.

[20] J. Crowder and N. J. Cornish. "Beyond LISA: Exploring future gravitational wave missions." *Physical Review D - Particles, Fields, Gravitation and Cosmology* 72.8 (2005). ISSN: 15507998. DOI: 10.1103/PhysRevD.72.083005. URL: https://arxiv.org/pdf/gr-qc/0506015.pdf.

[21] P. E. Ciddor. "Refractive index of air: new equations for the visible and near infrared." *Applied optics* 35.9 (1996), pp. 1566–1573. DOI: 10.1364/AO.35.001566.

APPENDIX A

Appendix A - Schematics, layouts and designs

- Schematic of second rotational stage complete assembly design
- Exploded view schematic of reference mirror mount of second rotational stage
- Exploded view schematic of motor mount of second rotational stage
- Exploded view Schematic of second rotational stage mount on first rotational stage
- Pin assignment of the D-SUB interfaces
- Ensemble ML auxiliary encoder channel pin assignment
- Atom miniature encoder system Ri connector pin assignment
- PCB electronic schematic for the encoders integration in FPGA
- Differential Line Receiver Quad MAX3095CSE+
- STR2 micro step controller driver

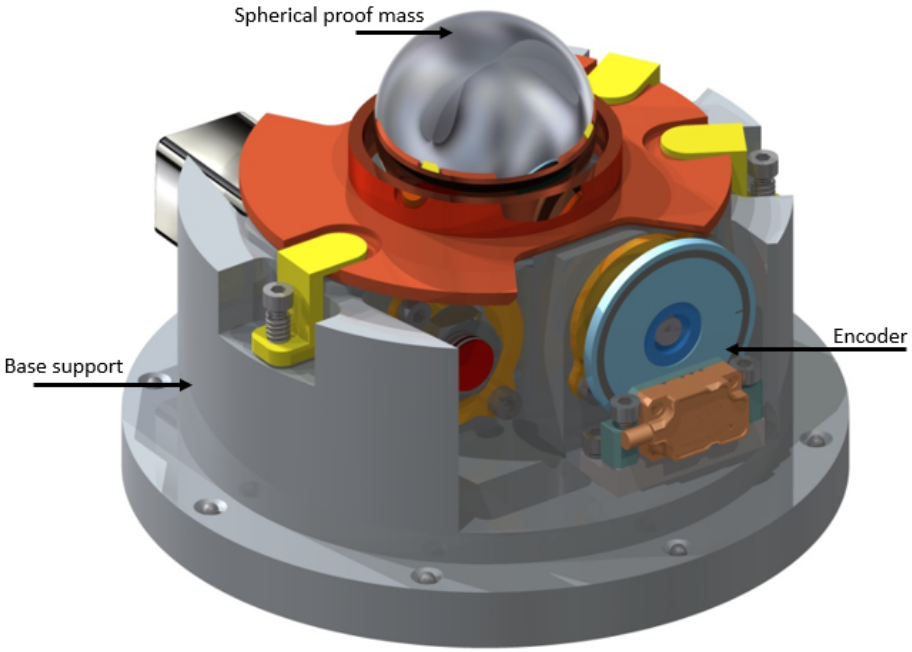

Figure A.1: CAD rendering of the complete assembly design. ADAPTED [19]

Table A.1: Pin assignment of the D-SUB interfaces in designed PCB

Pin	Assignment for first rotational encoder	Assignment for second rotational encoder
1	+B	-MKP
2	+A	GND
3	-A	-B
4	GND	+B
5	-MKP	+A
6	-B	+MKP
7	GND	GND
8	GND	+5V
9	+MKP	-A

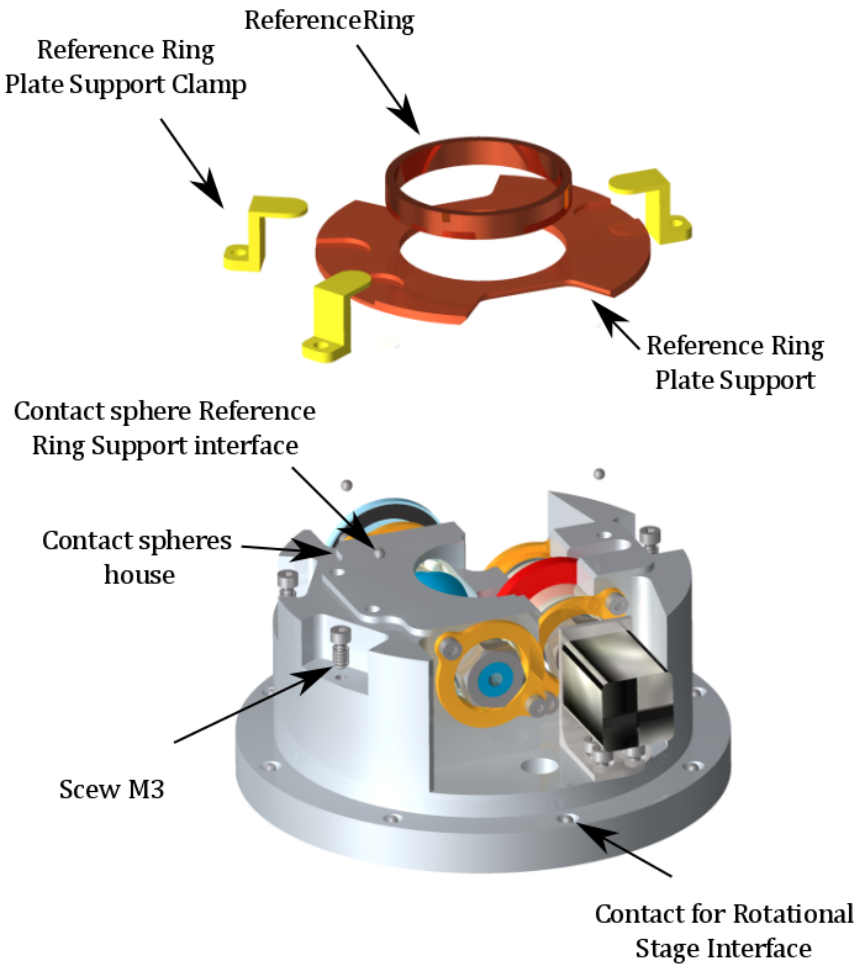

Figure A.2: Exploded view of the reference mirror mount.[19]

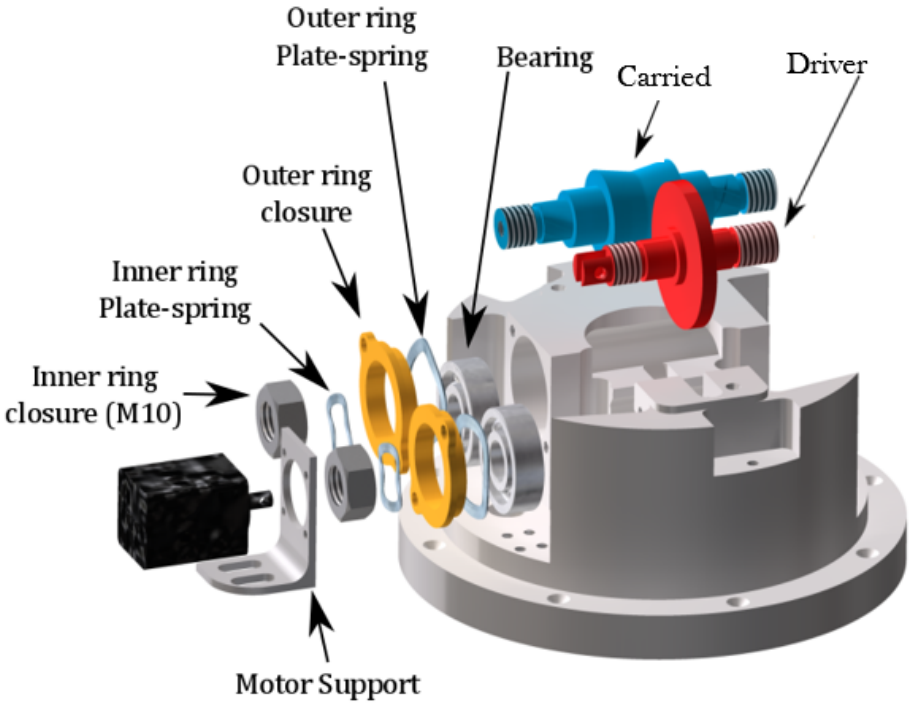

Figure A.3: Exploded view of the motor mount. ADAPTED[19]

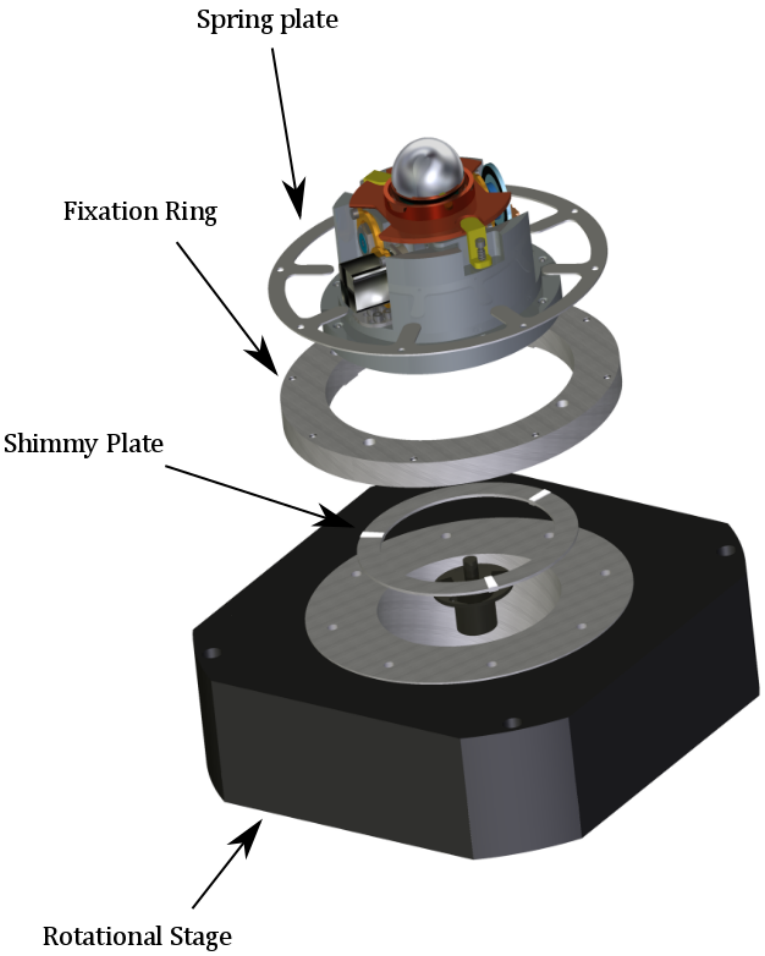

Figure A.4: Exploded view of the second rotational stage mounting on the first rotational stage. The shimmy plate serves as a three point support for the second rotational stage on top of the first.[19]

3.7. Auxiliary Encoder Channel/PSO Output (J201)

The auxiliary encoder interface accepts an RS-422 differential quadrature line driver signal. Invalid or missing signals will cause a feedback fault when the axis is enabled.

This encoder channel can be used as an input for master/slave operation (handwheel) or for dual feedback systems. The auxiliary encoder interface does not support analog encoders and cannot be used as an input for the -MXH or -MXU option.

The auxiliary encoder channel can also be used to echo the standard encoder signals or as the PSO output. Configuring the PSO hardware will automatically configure this encoder channel as an output (refer to Section 3.7.1.) and will remove the 180 ohm terminator resistors.

Table 3-18: Auxiliary Encoder Specifications

Specification	Value
Encoder Frequency	10 MHz maximum (25 nsec minimum edge separation)
x4 Quadrature Decoding	40 million counts/sec
MXH Interpolation Latency	~ 3.25 µsec (analog input to quadrature output)

NOTE: Use the EncoderDivider parameter to configure the bi-directional encoder interface on the auxiliary I/O connector. The EncoderDivider parameter converts the auxiliary encoder interface to an output and defines a divisor for the encoder echo. Refer to the Ensemble Help file for more information.

NOTE: You cannot echo the standard encoder signals on the ML with the -MXU option.

Table 3-19: Auxiliary Encoder Channel Pin Assignment (J201)

Pin#	Description	In/Out/Bi	Connector
1	Auxiliary RS-422 Marker Pulse - / PSO Output (1)	Bidirectional	
2	Auxiliary RS-422 Encoder Cosine +	Bidirectional	
3	Auxiliary RS-422 Encoder Cosine -	Bidirectional	
4	Auxiliary RS-422 Encoder Sine +	Bidirectional	
5	Encoder Cable Shield	N/A	
6	Auxiliary RS-422 Marker Pulse +/ PSO Output (1)	Bidirectional	
7	Encoder +5 Volt Power	Output	
8	Encoder Power Common	N/A	
9	Auxiliary RS-422 Encoder Sine -	Bidirectional	

(1) For PSO, see Section 3.7.1.

J201 Adapter Cable Assembly	Aerotech P.N. (1)	Third Party P.N.
9 Pin Standard D-style	C20931	N/A
25 Pin Standard D-style	C20932	N/A
Flying Leads	ECZ01343	Molex 83421-9042

(1) See the cable drawings on your software CD ROM

Figure A.5: First rotational stage auxiliary encoder channel pin assignment.

Interface signals

Ri and Ti interfaces

	Digital			Analogue		
Function	**Signal**		**Pin**	**Signal**		**Pin**
Power*	5 V		7, 8	5 V		4, 5
	0 V		2, 9	0 V		12, 13
Incremental signals	A	+	14	V_1	+	9
		-	6		-	1
	B	+	13	V_2	+	10
		-	5		-	2
Reference mark	Z	+	12	V_0	+	3
		-	4		-	11
Alarm†	E	+	11	–		–
		-	3			
Set-up	X		1	V_x		6
Remote CAL	–		–	CAL		14
Shield	–		Case	–		Case
Do not connect	–		10, 15	–		7, 8, 15

*All power connections can be used either to minimise voltage drop down the cable or incorporate voltage sensing.
†The alarm signal can be output as a line driver signal or 3-state.
Please select the preferred option at time of ordering.

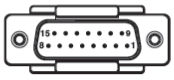
RI connector

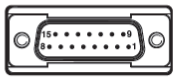
TI connector

Figure A.6: Atom miniature encoder system Ri connector pin assignment

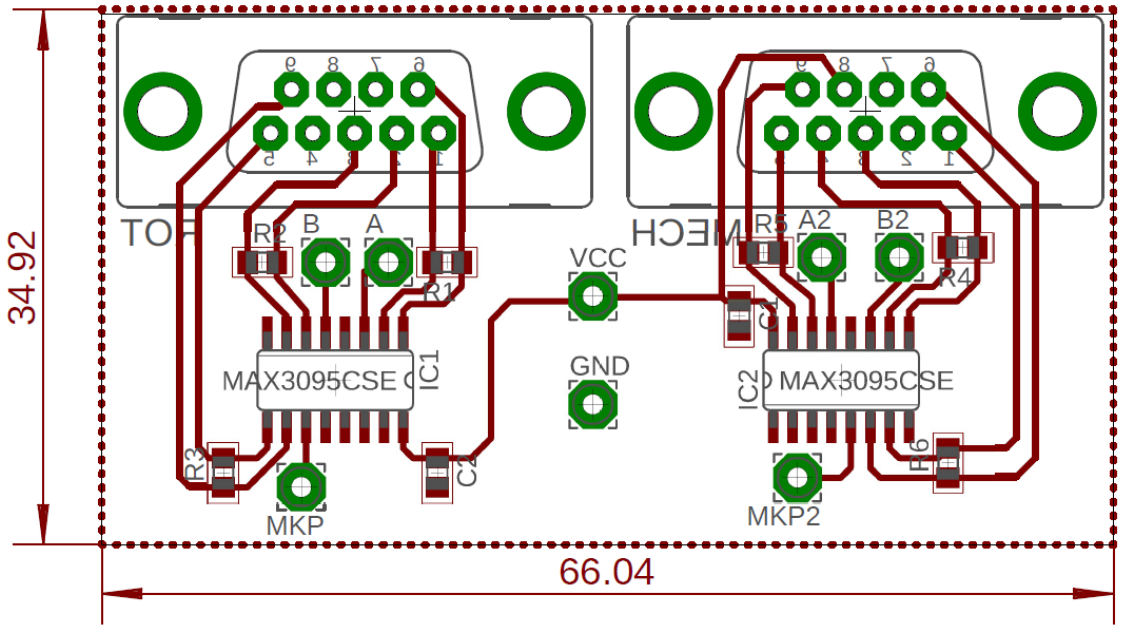

Figure A.7: PCB electronic schematic for the encoders integration in FPGA, where ROT stands for first rotational encoder and MECH for second rotational encoder

19-0498; Rev 3; 1/10

MAXIM

±15kV ESD-Protected, 10Mbps, 3V/5V, Quad RS-422/RS-485 Receivers

MAX3095/MAX3096

General Description

The MAX3095/MAX3096 are rugged, low-power, quad, RS-422/RS-485 receivers with electrostatic discharge (ESD) protection for use in harsh environments. All receiver inputs are protected to ±15kV using IEC 1000-4-2 Air-Gap Discharge, ±8kV using IEC 1000-4-2 Contact Discharge, and ±15kV using the Human Body Model. The MAX3095 operates from a +5V supply, while the MAX3096 operates from a +3.3V supply. Receiver propagation delays are guaranteed to within ±8ns of a predetermined value, thereby ensuring device-to-device matching across production lots.

Complementary enable inputs can be used to place the devices in a 1nA low-power shutdown mode in which the receiver outputs are high impedance. When active, these receivers have a fail-safe feature that guarantees a logic-high output if the input is open circuit. They also feature a quarter-unit-load input impedance that allows 128 receivers on a bus.

The MAX3095/MAX3096 are pin-compatible, low-power upgrades to the industry-standard '26LS32. They are available in a space-saving QSOP package.

Applications

Telecommunications Equipment

Rugged RS-422/RS-485/RS-423 Bus Receiver

Receivers for ESD-Sensitive Applications

Level Translators

Functional Diagram

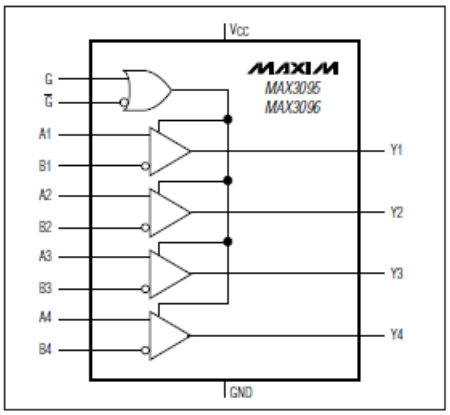

Features

- ESD Protection:
  ±15kV—IEC 1000-4-2, Air-Gap Discharge
  ±8kV—IEC 1000-4-2, Contact Discharge
  ±15kV—Human Body Model
- Guaranteed Propagation-Delay Tolerance Between All ICs:
  ±8ns (MAX3095)
  ±10ns (MAX3096)
- Single +3V Operation (MAX3096)
  Single +5V Operation (MAX3095)
- 16-Pin QSOP (8-pin SO footprint)
- 10Mbps Data Rate
- Allow up to 128 Receivers on the Bus
- 1nA Low-Power Shutdown Mode
- 2.4mA Operating Supply Current
- Pin-Compatible Upgrades to '26LS32

Ordering Information

PART	TEMP. RANGE	PIN-PACKAGE
MAX3095CPE+	0°C to +70°C	16 Plastic DIP
MAX3095CSE+	0°C to +70°C	16 Narrow SO
MAX3095CEE+	0°C to +70°C	16 QSOP
MAX3095EPE+	-40°C to +85°C	16 Plastic DIP
MAX3095ESE+	-40°C to +85°C	16 Narrow SO
MAX3095EEE+	-40°C to +85°C	16 QSOP
MAX3096CPE+	0°C to +70°C	16 Plastic DIP
MAX3096CSE+	0°C to +70°C	16 Narrow SO
MAX3096CEE+	0°C to +70°C	16 QSOP
MAX3096EPE+	-40°C to +85°C	16 Plastic DIP
MAX3096ESE+	-40°C to +85°C	16 Narrow SO
MAX3096EEE+	-40°C to +85°C	16 QSOP

+Denotes a lead(Pb)-free/RoHS-compliant package.

Pin Configuration

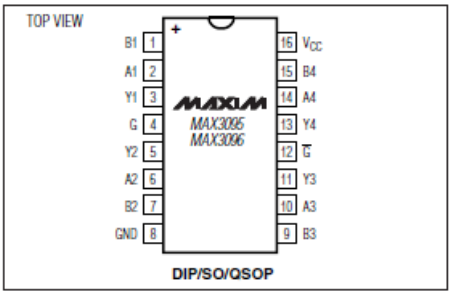

DIP/SO/QSOP

Figure A.8: Differential Line Receiver Quad MAX3095CSE+.

Hardware Manual

STR2
Step Motor Drive

920-0059B
1/30/2014

Applied Motion Products

Figure A.9: STR2 micro step controller driver.

Appendix B

Appendix B - LabVIEW, MATLAB, Python and VHDL scripts

- Block diagram code of the mixer
- Block diagram code of 500Hz sixth order Butterworth low pass filter
- VHDL code for low pass filter design
- Host program sampling speed increase with Asynchronous VI
- MATLAB script for thermal and mechanical noise displacement performance
- MATLAB script for QPDs displacement measurement analysis
- MATLAB script for SPM surface plotting with encoder data
- Python script for refractive index calculation

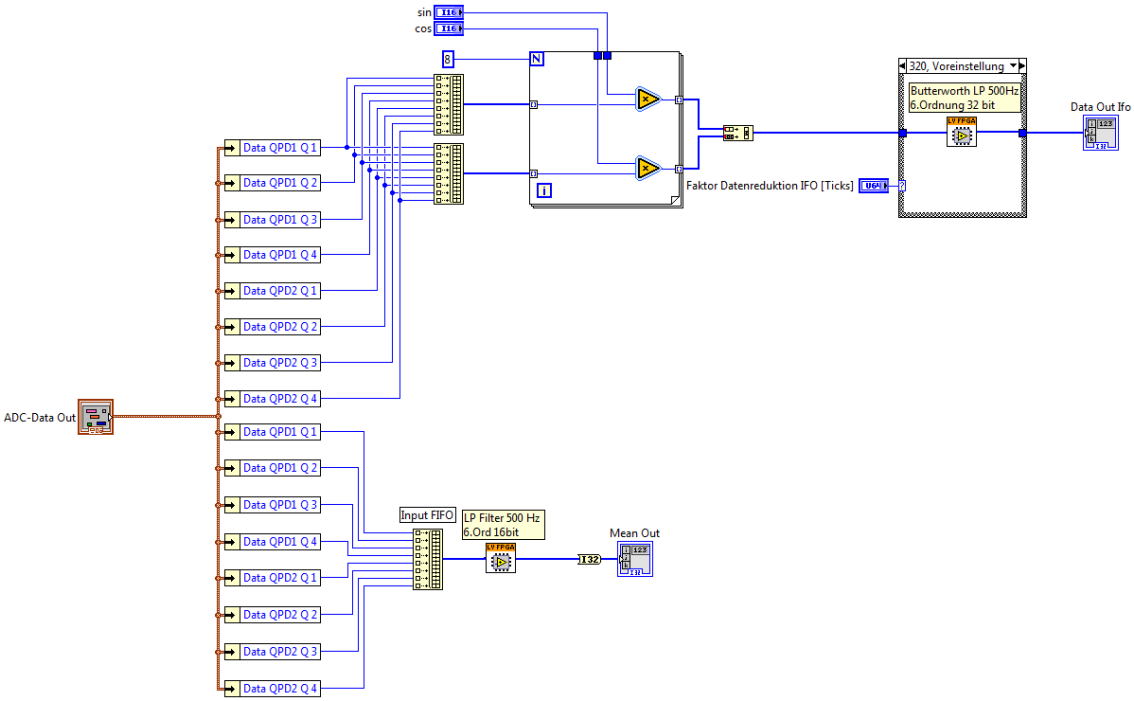

Figure B.1: LabVIEW blockdiagram code of developed frequency mixer with in-quadrature measurement by multiplying two identical signals with two other signals internally generated by the FPGA with a 90° phase shift.

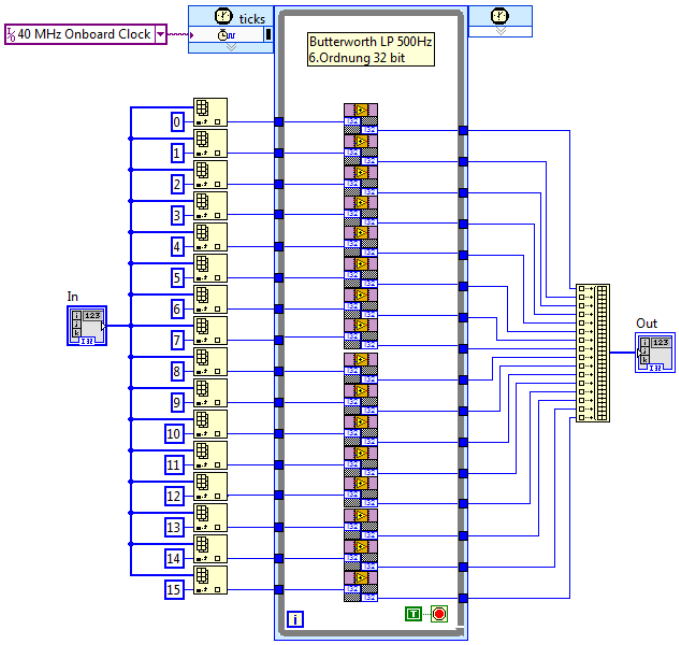

Figure B.2: LabVIEW blockdiagram code of developed low pass filter for frequency mixer, working at 40 MHz or at FPGA single cycle loop.

```vhdl
constant a: natural := 4;

process(clk)
    variable reg1: signed(x'length + a - 1 downto 0) := (others=>'0');
    variable reg2: signed(x'length + a - 1 downto 0) := (others=>'0');
    variable reg3: signed(x'length + a - 1 downto 0) := (others=>'0');
    variable reg4: signed(x'length + a - 1 downto 0) := (others=>'0');
    variable reg5: signed(x'length + a - 1 downto 0) := (others=>'0');
    variable reg6: signed(x'length + a - 1 downto 0) := (others=>'0');
begin
    if rising_edge(clk) then
        if enable_in = '1' then
            reg1 := reg1 - reg1(reg1'length-1 downto a) - signed("0"&std_logic_vector(reg1(a-1 downto a-1)))
                + signed(x);
            reg2 := reg2 - reg2(reg2'length-1 downto a) - signed("0"&std_logic_vector(reg2(a-1 downto a-1)))
                + reg1 - reg1(reg1'length-1 downto a) - signed("0"&std_logic_vector(reg1(a-1 downto a-1)));

            reg3 := reg3 - reg3(reg3'length-1 downto a) - signed("0"&std_logic_vector(reg3(a-1 downto a-1)))
                + reg2 - reg2(reg2'length-1 downto a) - signed("0"&std_logic_vector(reg2(a-1 downto a-1)));

            reg4 := reg4 - reg4(reg4'length-1 downto a) - signed("0"&std_logic_vector(reg4(a-1 downto a-1)))
                + reg3 - reg3(reg3'length-1 downto a) - signed("0"&std_logic_vector(reg3(a-1 downto a-1)));

            reg5 := reg5 - reg5(reg5'length-1 downto a) - signed("0"&std_logic_vector(reg5(a-1 downto a-1)))
                + reg4 - reg4(reg4'length-1 downto a) - signed("0"&std_logic_vector(reg4(a-1 downto a-1)));

            reg6 := reg6 - reg6(reg6'length-1 downto a) - signed("0"&std_logic_vector(reg6(a-1 downto a-1)))
                + reg5 - reg5(reg5'length-1 downto a) - signed("0"&std_logic_vector(reg5(a-1 downto a-1)));

            y <= sted_logic_vector(reg6(reg6'length-1 downto a)
                + signed("0"&std_logic_vector(reg6(a-1 downto a-1)));
        end if;
    end if;
end process;
enable_out <= enable_in
```

Figure B.3: VHDL code for Low pass filter design, using six first order butterworth low pass filters in cascade with parameter $a = 4$, having thus a cut-off frequency of 575.23 Hz.

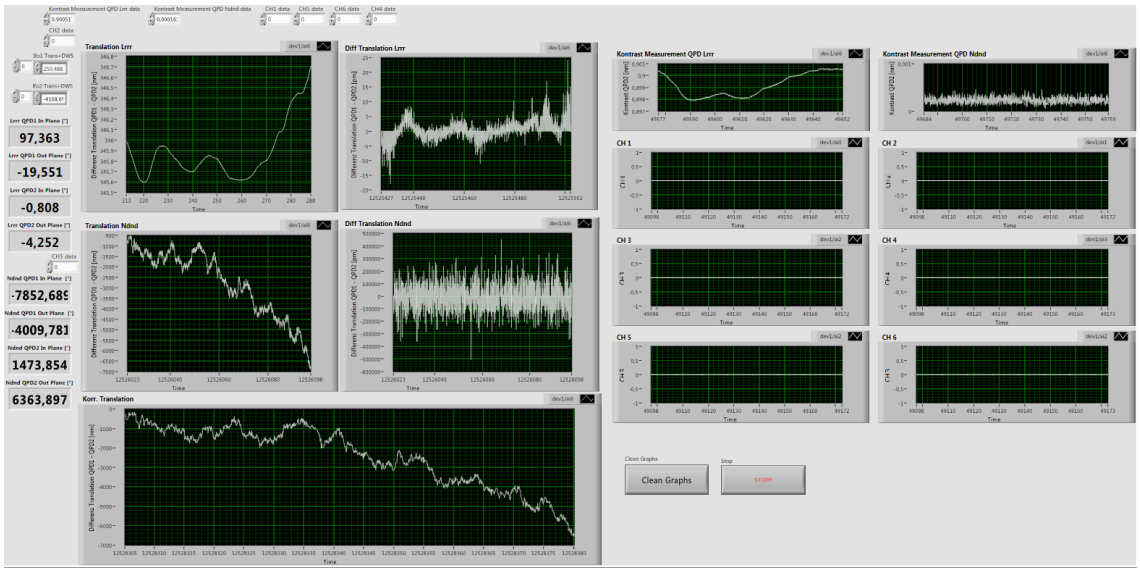

Figure B.4: LabVIEW front panel of 5.7 with Lrrr as IFO_1, Ndnd as IFO_2 and channels 1-6 as voltage detectors. The "Diff"plots shows the difference between two consecutive translation measurements. The "Kontrast"plots shows the information from QPD_{MES} for each interferometer. The "Korr"or correlation plot shows the sum of both interferometers translations.

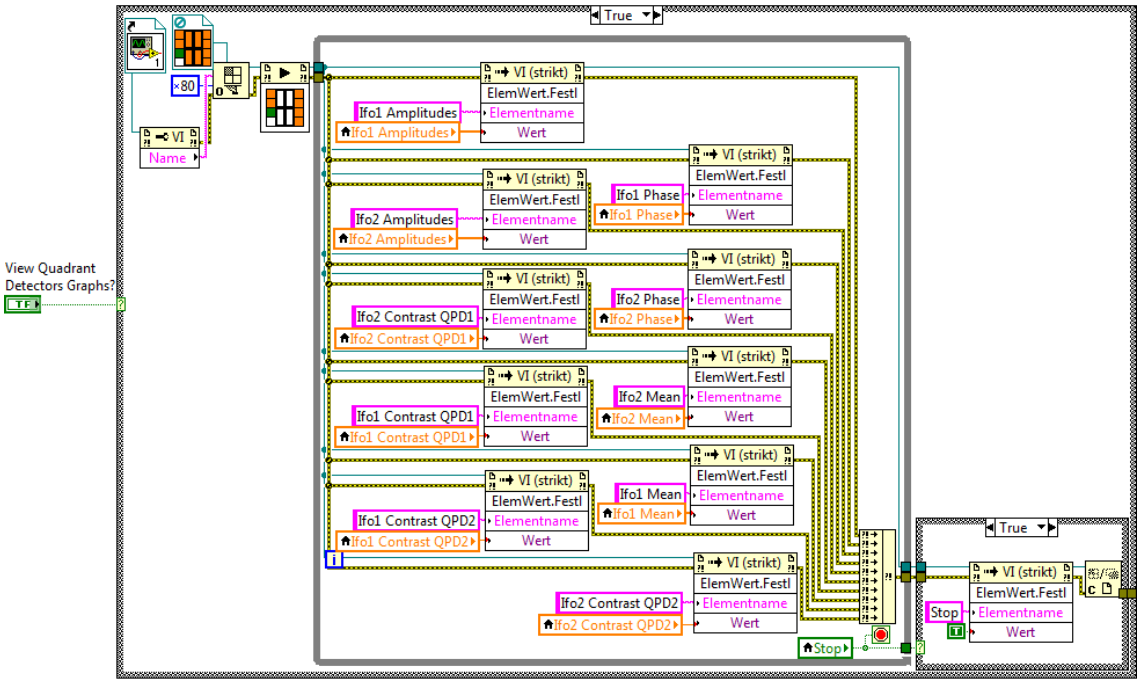

Figure B.5: LabVIEW blockdiagram code developed for increasing host program sampling rate by using Asynchronous VI for parallel processing with multi-threading.

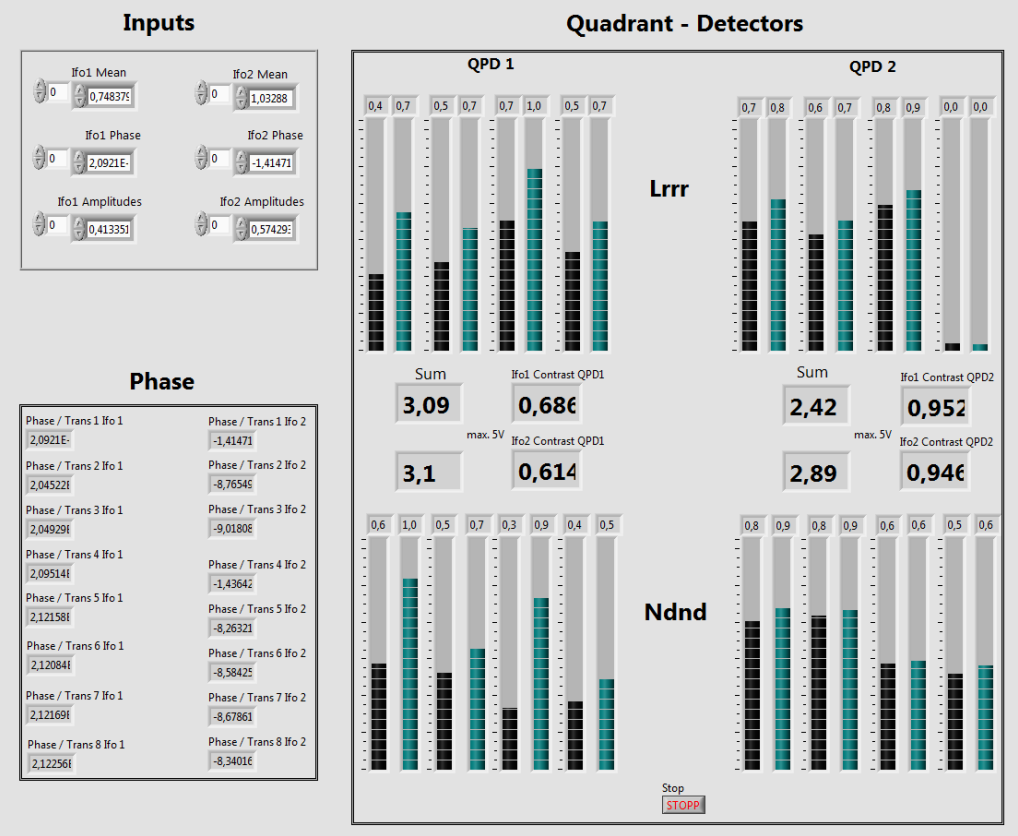

Figure B.6: LabVIEW front panel of B.5 with Lrrr as IFO_1, Ndnd as IFO_2 and the QPD_S channels where each of the four photodetectors of the QPD_s measures the laser beam intensity, right bar blue, and the super imposed laser beam, left bar black. It is possible to see that one of the quadrants of the QPD2 or QPD_{meas} from IFO1 or Lrrr is no longer working and that alignment adjustments have to be done.

```
ltpda_startup;                                          %LISA toolbox
filename = 'Measurement_file.mat';                      %Specify filename
A = load('-mat', filename);                             %Load data
B = cell2mat(struct2cell(A));                           %Convert struct to matrix
samplingFreq = 500;                                     %Sampling frequency in [Hz]

IFO = array2table(B(:,1:5),'VariableNames',{...
    't','IFO1_MES','IFO1_REF','IFO2_MES','IFO2_REF'});  %Data from IFOs in micro rad
measureTime = size(IFO.t,1)/samplingFreq;               %Measurement time in [sec]
pl = plist('NAVS',[2], 'ORDER',[1],'WIN','BH92');       %Input parameter list for PSD

%IFO 1
cons = 1064*10^-6*/(4*pi);                              %Translate micro rad to nanometer
DIFF_IFO1 = IFO.IFO1_MES - IFO.IFO1_REF;
a_DIFF_IFO1 = ao(cons*DIFF_IFO1, samplingFreq);         %Create analysis object for LISA toolbox
setYunits(a_DIFF_IFO1, '[nm]');                         %Set units as [pm]
b_DIFF_IFO1 = psd(a_DIFF_IFO1,pl);                      %Create PSD
c_DIFF_IFO1 = sqrt(b_DIFF_IFO1);                        %Take sqrt to get [pm/sqrt(Hz)]
c_DIFF_IFO1.setName('IFO1');

% %IFO 2
DIFF_IFO2 = IFO.IFO2_MES - IFO.IFO2_REF;
a_DIFF_IFO2 = ao(cons*DIFF_IFO2, samplingFreq);         %Create analysis object for LISA toolbox
setYunits(a_DIFF_IFO2, '[nm]');                         %Set units as [pm]
b_DIFF_IFO2 = psd(a_DIFF_IFO2, pl);                     %Create PSD
c_DIFF_IFO2 = sqrt(b_DIFF_IFO2);                        %Take sqrt to get [pm/sqrt(Hz)]
c_DIFF_IFO2.setName('IFO2')


% Final Plot
 pl_1 = plist('Linecolors', {'b', 'r'}, 'LineStyles', {'-', '-'}, 'LineWidths', {1, 1});
 figure(2)
     iplot(c_DIFF_IFO1, c_DIFF_IFO2, pl_1)
     title('Performance measurement')
```

Figure B.7: MATLAB script for the noise displacement performance measurement analysis, using the LTPDA toolbox. The parameters used for the PSD analyzes are: "NAVS"which stands for number of averages, therefor the data e average 2 times; "ORDER"stands for the order of segment detrending, with the value 1 was subtract linear fit; "WIN"stands for the window to be applied to the data to remove the discontinuities at edges of segments with "BH92"as Blackman Harris 92dB filtering window.

```
ltpda_startup;                                              %LISA toolbox
filename = 'Measurement_file';                              %Specify filename
A = load('-mat', filename);                                 %Load data
B = cell2mat(struct2cell(A));                               %Convert struct to matrix
samplingFreq = 500;                                         %Sampling frequency in [Hz]
IFO = array2table(B(:,1:5),'VariableNames',{...
    't','IFO1_MES','IFO1_REF','IFO2_MES','IFO2_REF'});      %IFOs data in micro rad
measureTime = size(IFO.t,1)/samplingFreq;                   %Measurement time in [sec]
cons = 1064*10^-6/(4*pi);                                   %Set data from micro rad to
nanometers
%IFO 1
a_IFO1_MES = ao(IFO.IFO1_MES*cons, samplingFreq);           %Create object to be
analyzed by LTPDA
a_IFO1_REF = ao(IFO.IFO1_REF*cons, samplingFreq);
a_IFO1 = ao(abs(IFO.IFO1_MES - IFO.IFO1_REF)*cons, samplingFreq);
a_IFO1.setName('IFO1')

%IFO 2
a_IFO2_MES = ao(IFO.IFO2_MES*cons, samplingFreq);
a_IFO2_REF = ao(IFO.IFO2_REF*cons, samplingFreq);
a_IFO2 = ao(abs(IFO.IFO2_MES - IFO.IFO2_REF)*cons, samplingFreq);
a_IFO2.setName('IFO2')

pl = plist('Linecolors', {'b', 'r'}, 'LineStyles', {'-', '-'}, 'LineWidths', {1, 1});
figure(1)
iplot( a_IFO1_MES, a_IFO1_REF, pl)
title('IFO1 QPD_s displacement')
xlabel('time [s]') % x-axis label
ylabel('displacement [nm]') % y-axis label
legend('QPD_{MES}','QPD_{REF}')

figure(2)
iplot( a_IFO2_MES, a_IFO2_REF, pl)
title('IFO2 QPD_s displacement')
xlabel('time [s]') % x-axis label
ylabel('displacement [nm]') % y-axis label
legend('QPD_{MES}','QPD_{REF}')

figure(3)
iplot(a_IFO1, pl)
title('IFO1 |QPD_{MES} - QPD_{REF}| displacement test')
xlabel('time [s]') % x-axis label
ylabel('displacement [nm]') % y-axis label

figure(4)
iplot(a_IFO2, pl)
title('IFO2 |QPD_{MES} - QPD_{REF}| displacement test')
xlabel('time [s]') % x-axis label
ylabel('displacement [nm]') % y-axis label
```

Figure B.8: MATLAB script for QPD displacement measurement analysis.

```
filename = sprintf('phase/surface_total.mat');
a = load('-mat', filename);
prime=a.IFO(:,1);
prime_rad=(2*pi)/260000*prime; %Integer value to angle, for first encoder
second=a.IFO(:,2);
second_rad=(2*pi)/(20000*0.9)*second; %Translate second encoder resolution to SPM

 x=[-2.5 2.5
     0    0
     0    0];
  y=[  0    0
       0    0
      -2.5 2.5];

figure
    plot3(x(1,:),x(2,:),x(3,:),'k','Linewidth',2.5) %plot x axis
    hold on
    plot3(y(1,:),y(2,:),y(3,:),'k','Linewidth',2.5) %plot y axis
    hold on
    B=[];
    for i=1:floor(length(prime_rad))
        rot=[2 0 0                                  %Rotational matrix for second encoder
        0 2*cos(second_rad(i)) -2*sin(second_rad(i))
        0 2*sin(second_rad(i))  2*cos(second_rad(i))];
        [xunit,yunit,zunit] = circle_V2(prime_rad(i)); %Polar coordinates to Cartesian coordinates
        BB=rot*[xunit;yunit;zunit]; %Rotate Cartesian coordinates with second encoder angle
        B=[B,BB];
    end
    plot3(B(1,1:end),B(2,1:end),B(3,1:end)) %Plot surface
    axis equal
```

Figure B.9: MATLAB script for simulation of SPM surface topography mapping with only encoder data.

```python
# ADAPTED FROM:
# Author: Mikhail Polyanskiy
# Original data: Ciddor 1996, https://doi.org/10.1364/AO.35.001566
import numpy as np
def Z(T,p,xw): #compressibility
    t=T-273.15
    a0 = 1.58123e-6   #K·Pa^-1
    a1 = -2.9331e-8   #Pa^-1
    a2 = 1.1043e-10   #K^-1·Pa^-1
    b0 = 5.707e-6     #K·Pa^-1
    b1 = -2.051e-8    #Pa^-1
    c0 = 1.9898e-4    #K·Pa^-1
    c1 = -2.376e-6    #Pa^-1
    d  = 1.83e-11     #K^2·Pa^-2
    e  = -0.765e-8    #K^2·Pa^-2
    return 1-(p/T)*(a0+a1*t+a2*t**2+(b0+b1*t)*xw+(c0+c1*t)*xw**2) +
    (p/T)**2*(d+e*xw**2)
def n(o,t,p,h,xc):
    # o: wavelength, 0.3 to 1.69 µm
    # t: temperature, -40 to +100 °C
    # p: pressure, 1000 to 120000 Pa
    # h: fractional humidity, 0 to 1
    # xc: CO2 concentration, 0 to 2000 ppm
    omega = 1/o       #µm^-1
    T= t + 273.15     #Temperature °C -> K
    R = 8.314510      #gas constant, J/(mol·K)
    k0 = 238.0185     #µm^-2
    k1 = 5792105      #µm^-2
    k2 = 57.362       #µm^-2
    k3 = 167917       #µm^-2
    w0 = 295.235      #µm^-2
    w1 = 2.6422       #µm^-2
    w2 = -0.032380    #µm^-4
    w3 = 0.004028     #µm^-6
    A = 1.2378847e-5  #K^-2
    B = -1.9121316e-2 #K^-1
    C = 33.93711047
    D = -6.3431645e3  #K
    alpha = 1.00062
    beta = 3.14e-8    #Pa^-1,
    gamma = 5.6e-7    #°C^-2
    #saturation vapor pressure of water vapor in air at temperature T
    if(t>=0):
        svp = np.exp(A*T**2 + B*T + C + D/T) #Pa
    else:
        svp = 10**(-2663.5/T+12.537)
    #enhancement factor of water vapor in air
    f = alpha + beta*p + gamma*t**2
    #molar fraction of water vapor in moist air
    xw = f*h*svp/p
    #refractive index of standard air at 15 °C, 101325 Pa, 0% humidity, 450 ppm CO2
    nas = 1 + (k1/(k0-omega**2)+k3/(k2-omega**2))*1e-8
    #refractive index of standard air at 15 °C, 101325 Pa, 0% humidity, xc ppm CO2
    naxs = 1 + (nas-1) * (1+0.534e-6*(xc-450))
    #refractive index of water vapor at standard conditions (20 °C, 1333 Pa)
    nws = 1 + 1.022*(w0+w1*omega**2+w2*omega**4+w3*omega**6)*1e-8
    Ma = 1e-3*(28.9635 + 12.011e-6*(xc-400)) #molar mass of dry air, kg/mol
    Mw = 0.018015                            #molar mass of water vapor, kg/mol
    Za = Z(288.15, 101325, 0)                #compressibility of dry air
    Zw = Z(293.15, 1333, 1)                  #compressibility of pure water vapor
    #Eq.4 with (T,P,xw) = (288.15, 101325, 0)
    densityaxs = 101325*Ma/(Za*R*288.15)           #density of standard air
    #Eq 4 with (T,P,xw) = (293.15, 1333, 1)
    densityws  = 1333*Mw/(Zw*R*293.15)             #density of standard water vapor
    # two parts of Eq.4: density=densitya+densityw
    densitya   = p*Ma/(Z(T,p,xw)*R*T)*(1-xw)       #density of the dry component of
    the moist air
    densityw   = p*Mw/(Z(T,p,xw)*R*T)*xw           #density of the water vapor
    component
    nprop = 1 + (densitya/densityaxs)*(naxs-1) + (densityw/densityws)*(nws-1)
    return nprop
```

Figure B.10: Python script, adapted from RefractiveIndex.INFO website: © 2008-2018 Mikhail Polyanskiy, for the calculation of the refractive index using data from [21] .

Appendix

C

Appendix C - Other results

C.1 Results obtain from full measurement time

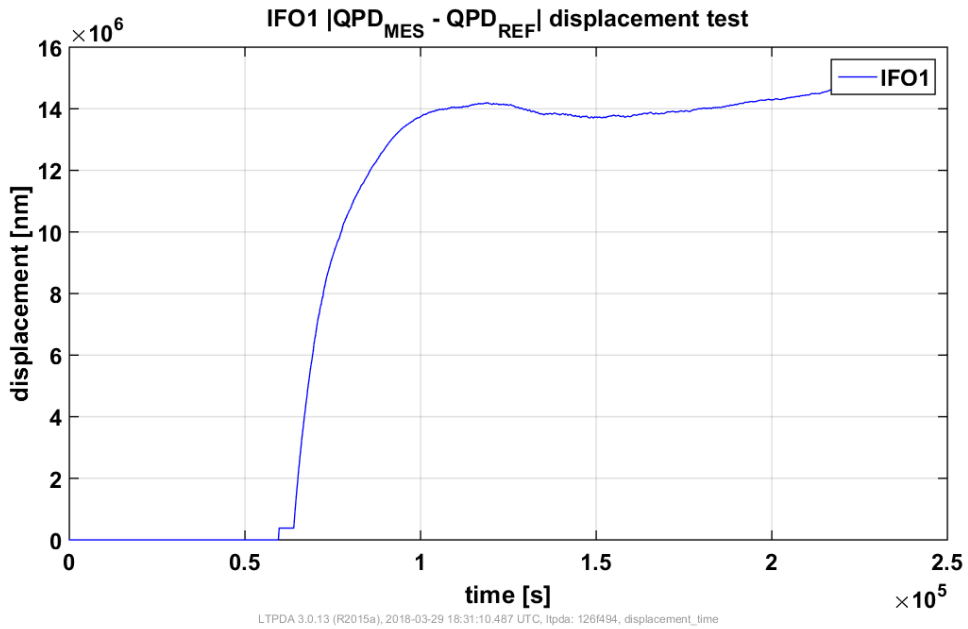

Figure C.1: Measurement data from entire measurement time for IFO1.

During the measurement, the laser beam got out of phase at $\approx 0.52 * 10^5$ seconds of measurement, thus the displacement measurement starting increasing in such a way that not longer represents reality. Therefore in the results section, only the measurements done while the lasers were not out of phase, are analyzed.

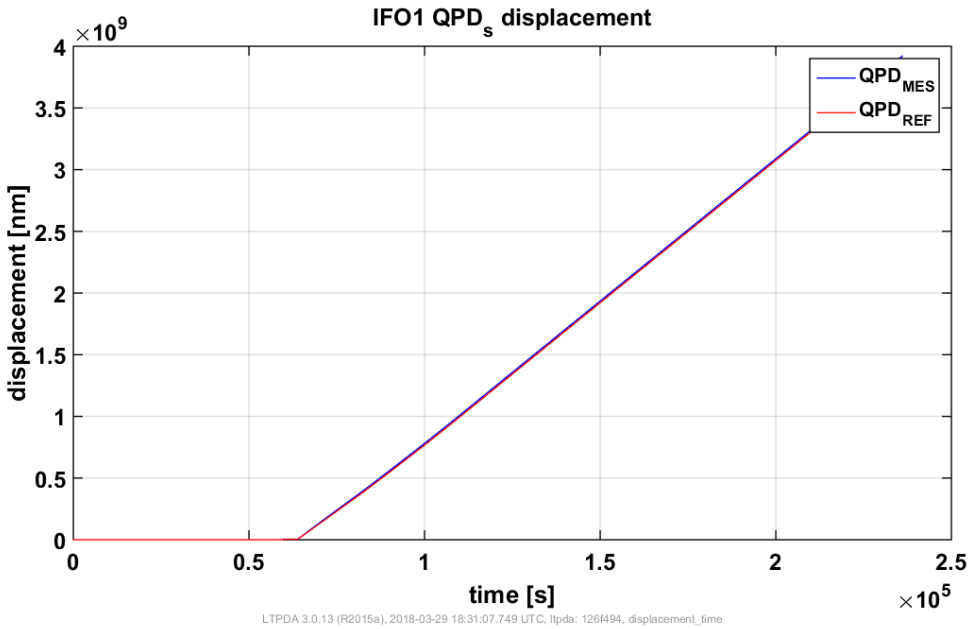

Figure C.2: Measurement data from entire measurement time for IFO1 QPD_s.

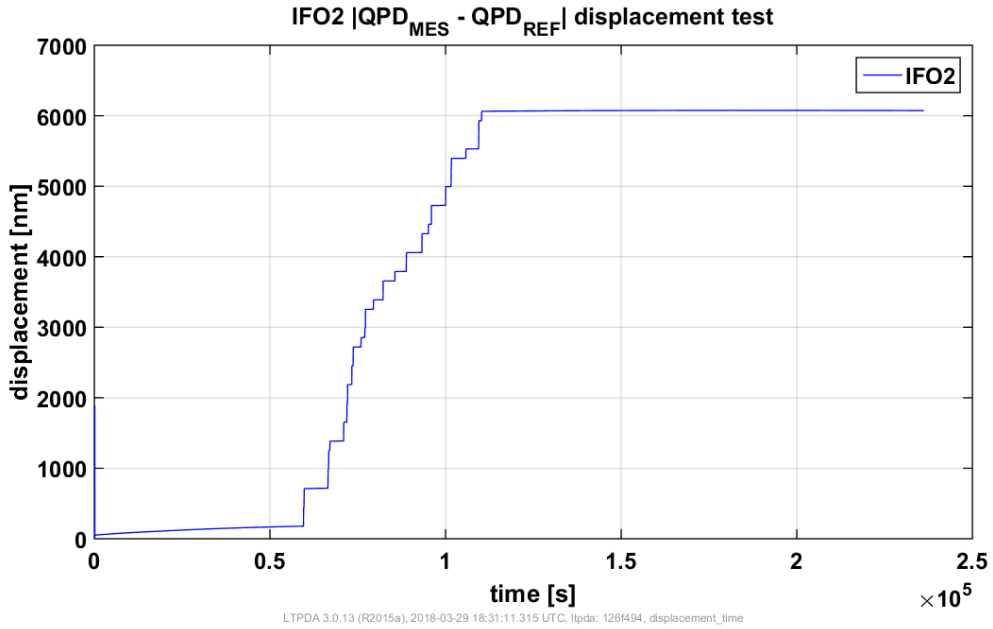

Figure C.3: Measurement data from entire measurement time for IFO2.

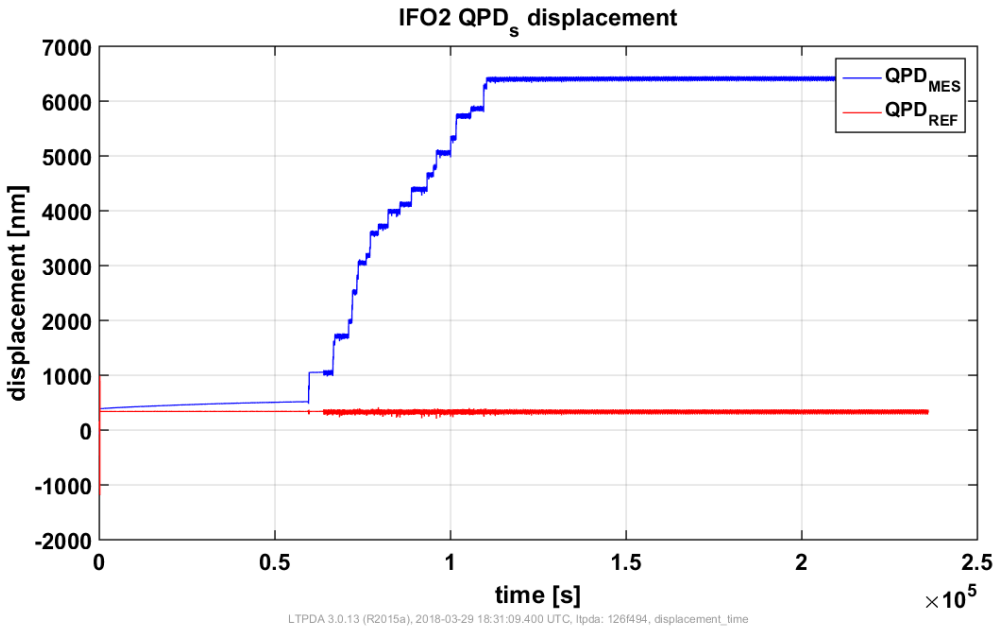

Figure C.4: Measurement data from entire measurement time for IFO2 QPD_s.

João Pedro Bento Vilas

Master of Science

Interferometric mapping of test mass surfaces for precise position determination in inertial sensors

Dissertation submitted in partial fulfillment
of the requirements for the degree of

Master of Science in
Physics Engineering

April, 2018

FACULDADE DE
CIÊNCIAS E TECNOLOGIA
UNIVERSIDADE NOVA DE LISBOA

João Pedro Bento Vilas

Master of Science

Interferometric mapping of test mass surfaces for precise position determination in inertial sensors

Dissertation submitted in partial fulfillment
of the requirements for the degree of

Master of Science in
Physics Engineering

April, 2018

FACULDADE DE
CIÊNCIAS E TECNOLOGIA
UNIVERSIDADE NOVA DE LISBOA

João Vilas 2018
Interferometric mapping of test mass surfaces for precise position determination in inertial s 2018